STUDIA UNIVERSITATIS
BABEŞ-BOLYAI

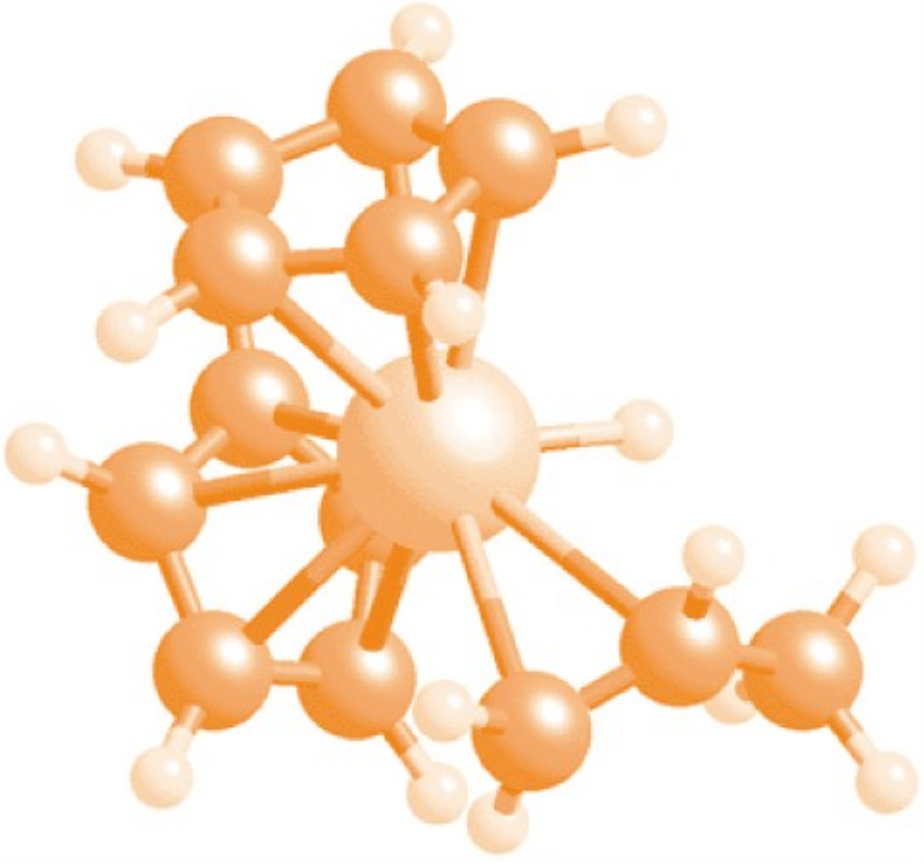

CHEMIA

2/2007

PROFESSOR PAUL ŞERBAN AGACHI

Born in Bucharest on October 21st, 1947, the personality of Professor Paul Şerban Agachi has become outlined already from the High School period spent at the National College "Sf. Sava" and then it gained value by attending the courses of the Faculty of Control Engineering and Computer Science of the Polytechnical Institute of Bucharest, graduated in 1970 on a highly ranked position obtained as an outstanding student.

From the early beginning of the career, his professional interests have been placed under the view and vision on the future role and great potential that the computers will have during the next decades, a prediction that has been fully confirmed by most features of the contemporary life.

The PhD degree obtained in 1985 in the field of Control has emerged from both wide and thorough theoretical and practical experience gained at the Design Institute for Organic Chemistry and the Computer Centre of the Ministry for Chemical Industry in Bucharest.

In 1978 Professor Agachi received the *Teclu Award* of the Romanian Academy as an early recognition for the value of scientific and technical work performed during the first years of his career. His future research interests have roots in this period and they will be constantly developed during the next years in the very attractive fields of modelling, simulation, control and optimisation of chemical processes.

The scientific contributions of Professor Paul Şerban Agachi are the result of his multidisciplinary education covering different engineering fields, such as: electrical, chemical and control fields. Integrating process control in successful applications is a task that involves both profound theoretical knowledge and comprehensive practical skills and both of them have been extensively proved by the theoretical developments of the Model Predictive Control algorithm and by the industrial applications achieved by Professor Agachi. Data acquisition and processing, modelling, control and optimisation have been investigated and implemented in a large number of processes, such as: polyvinylchloride production, volatile oils distillation, polyvinylacetate production, brine electrolysis, hydrazine production, fluid catalytic cracking or soda ash production.

The scientific research work performed during the 37 years of devoted efforts has emerged in 13 books and textbooks, over 200 articles in scientific journals, national or international scientific events and 6 patents. The most recently published book "Model Based Control - Case Studies in Process Engineering" at Wiley-VCH Verlag is a reference work in the control field, worldwide addressed to researchers, engineers and students.

A different but perfectly harmonizing facet of the scientist Paul Şerban Agachi is revealed by his gifted vocation for teaching, which finds its fulfilment starting with 1982 when he becomes member of the teaching staff of the Babeş-Bolyai University in Cluj-Napoca, at the Faculty of Chemistry and Chemical Engineering. The steps of the academic degrees are completed in short time and starting 1994 he becomes Professor of Control, Modelling and Optimisation.

The always enthusiastic and determined force and energy he generously invested in national or international research and education projects have shown important results. Invited Professor at Universities all around Europe, Professor Paul Şerban Agachi was awarded in 1992 with a Fulbright Scholarship at California Institute of Technology, Department of Chemical Engineering, as Visiting Associate in the Control group of Professor Manfred Morari, where he brought an important contribution to the Project of Modelling and Control of a Fluid Catalytic Cracking Unit for Chevron Research & Development.

Professor Paul Şerban Agachi has constantly been a pioneering messenger for the ideas of implementing information technology in education and research activities. His computer application projects have been proved to be successful first in the Faculty of Chemistry and Chemical

Engineering and then extended throughout the Babeş-Bolyai University, becoming a reference model for the Romanian higher education network.

The development of a new school of Computer Aided Process Engineering is a recognized contribution of Professor Agachi of which generations of professional highly trained students are grateful.

As a natural consequence of experience accumulation, the polyvalent personality of Professor Paul Şerban Agachi has also shown its quality at the level of leadership, first as Head of Chemical Engineering Department, then as Chancellor and eventually as Vice-rector of Babeş-Bolyay University. Recognized as a reformer and developer of the education and research systems, the results of his work in this field have achievements both in Romania and abroad; his participation in 2000 and 2001 as an UNESCO Higher Education consultant in the UN program "Oil for Food" in Iraq is a significant example. The critical analyses followed by the proposal of reforming solutions are results of his vigorous activity performed in the academic and management of the research, both at the Babeş-Bolyai University and at national level.

His scientific and management merits are worldwide recognized and he became member of prestigious international professional organizations, such as the American Institute of Chemical Engineers or DECHEMA, but also member of the Romanian Academy of Technical Sciences. Being an ambassador of the Romanian school of Computer Aided Process Engineering, he organized for the first time in Romania Cape Forum 2005 and ESCAPE 17, scientific events of high international standards.

In recognition of his research and institutional management contributions Professor Agachi was awarded by the President of Romania with the award *Ordinul National "Pentru Merit" în grad de Comandor*.

At his 60th anniversary, the teaching staff community of Babeş-Bolyai University and Editorial Board of Studia Chemia addresses to Professor Paul Şerban Agachi the appreciation for his entire activity along with the best wishes for a long life of successful future achievements.

The Editorial Board

LIST OF PUBLICATIONS

BOOKS

1. **P. Ş. Agachi**
   Models and application programs of operational methods in identifying control systems
   Editura M. I. Ch. , 1972
2. **P. Ş. Agachi**
   Determining mathematical models of technological processes in the chemical industry
   Editura M. I. Ch. ,1973
3. L. Oniciu, E. Schmidt, A. Soo, **P. Ş. Agachi**, V. Topan
   Conversia electrochimică a energiei
   Editura Şt. şi Enciclopedica, Bucureşti,1976
4. **P. Ş. Agachi**
   Automatizarea proceselor din industria chimică şi a materialelor de construcție
   Litografia UBB Cluj, 1976, 176 pag.
5. E. Gavrila, I. Bâldea, V. Topan, **P. Ş. Agachi**
   Chemical reaction engineering
   Litografia UBB Cluj-Napoca, 1988
6. **P. Ş. Agachi**
   Automatizarea proceselor chimice
   Editura Casa Cărții de Ştiință, Cluj-Napoca, 1994, 420 pag.
7. **P. Ş. Agachi**, M. Cristea,
   Automatizarea proceselor chimice. Caiet de lucrări practice
   Litografia UBB Cluj-Napoca, 1996, 97 pag.
8. A. Imre-Lucaci, **P. Ş. Agachi**
   Optimizarea proceselor din industria chimică
   Editura Tehnică Bucureşti, ISBN 973-31-2113-4, 2002, 292 pag.
9. M. V. Cristea, **P. Ş. Agachi**
   Elemente de Teoria Sistemelor
   Editura Risoprint Cluj-Napoca, ISBN:973-656-266-2, 2002, 337 pag.

10. V. M. Cristea, V. Marinoiu, **P. Ş. Agachi**,
Reglarea predictivă după model a instalației de cracare catalitică
Editura Casa Cărții de Ştiință, Cluj-Napoca, ISBN: 973-686-412-X, 2003, 183 pag.
11. **P. Ş. Agachi**, Z. K. Nagy, M. V. Cristea, A. Imre-Lucaci,
Model Based Control - Case Studies in Process Engineering,
WILEY-VCH Verlag GmbH & Co. KGaA, Weinheim,
ISBN-10: 3-527-31545-4, 2006, 278 pag.
12. V. Pleşu, **P. Ş. Agachi**, Editors
Computer Aided Chemical Engineering, vol. 24, 17-th European Symposium on Computer Aided Process Engineering, Elsevier, ISBN 978-0-444-53157-5, Amsterdam-Oxford, 2007, 1362 pag.
13. P. Nica, **P. Ş. Agachi**, Doina Banciu, A. Curaj, R. Gheorghiu, Geomina Turlea, D. M. Grosu, C. Baltei
Metodologii si proceduri pentru definirea obiectivelor si prioritatilor strategice ale cercetarii stiintifice si dezvoltarii tehnologice nationale pe perioada 2005-2010,
Editura Economica,2005, 100 pag.

ARTICLES AND LECTURES

1. **P. Ş. Agachi**
Numerical PI controller,
Student scientific proceedings, I. P. Bucuresti, 20-21 nov. 1969
2. **P. Ş. Agachi**
Methods of operational research of the processes in the chemical industry,
IPROSIN (MICh) Proceedings, 14-15 febr. 1972
3. **P. Ş. Agachi**
Optimization of the process of choline chloride, using Box. Wilson algorithm,
C. D. C. Symposium, MICh 13-14 apr. 1973
4. L. Oniciu, **P. Ş. Agachi**
Determining optimal parameters of a laboratory fuel cell working,
Proceedings of the Scientific meeting, Chemistry Faculty of Cluj,
7-8 iun. 1974
5. L. Oniciu, **P. Ş. Agachi**
Mathematical modeling of a methanol-oxygen fuel cell working,
The 4-th National Physical Chemistry Conference, Bucharest,
2-5 sept. 1974

6. L. Oniciu, **P. Ş. Agachi**
   Mathematical modeling of steady state working of a methanol air fuel cell,
   Studia U. B. B. ,2,1974, p. 76
7. L. Oniciu, **P. Ş. Agachi**
   Mathematical modeling of the optimum region in a fuel cell working,
   Studia U. B. B. ,1,1975 p. 72
8. **P. Ş. Agachi**
   Modeling control and optimization of the chemical processes,
   Conference at the Faculty of Chemistry, may 1975
9. L. Oniciu, **P. Ş. Agachi**, V. Topan
   Method of optimizing hydrazine hydrate process,
   Proceedings of the Chem. Faculty meeting, June 6-7th, 1975
10. L. Oniciu, **P. Ş. Agachi**, V. Topan
    Heterogenons ion-exchange membranes,
    Proceedings of the Chemistry Faculty meeting, June 6-7th, 1975
11. L. Oniciu, **P. Ş. Agachi**,
    Control solutions for methanol-air fuel cells(I),
    Rev. Chim. ,27, 5, 1976, p. 76
12. L. Oniciu, **P. Ş. Agachi**, V. Topan
    Mathematical model of CSTR. Dynamical working regime,
    Proceedings of the Chem. Fac. meeting, 28-29 may 1976
13. **P. Ş. Agachi**, V. Topan
    Modeling and optimization of the synthesis stage in the hydrazine hydrate process,
    The IV-th National Informatics Symposium, Cluj-Napoca, 10-13 may 1978
14. **P. Ş. Agachi**, V. Topan
    Mathematical modeling in dynamic and steady state working of a distillation column,
    The IV-th Conference of Informatics Cluj, 10-13 may 1978
15. L. Oniciu, E. Schmidt, E. Suciu, A. Soo, V. Topan, **P. Ş. Agachi**
    Hydrazine fuel cells,
    Rev. Roum. Chim. , 1, 1979, p. 38
16. **P. Ş. Agachi**, L. Oniciu, V. Topan
    Modeling of the dynamic working of a binary, packed distillation column,
    Rev. Chim. , 30, 12, 1979, p. 1230

17. V. Topan, **P. Ş. Agachi**, L. Oniciu
Chemical reaction control in a CSTR with nonlinear behavior, based on the mathematical model of the process,
Rev. Chim. , 31, 1, 1980, p 53

18. E. Grozeanu, V. Topan, **P. Ş. Agachi**, L. Oniciu
Aspects concerning the hydrazine/hydrogen peroxide fuel cells,
Energetica, 1, 1981, p. 32

19. L. Oniciu, **P. Ş. Agachi**
Control of a hydrazine/H2O2 fuel cell,
The II-nd National Congress of Chemistry, Buc. , 7-10 sept. 1981

20. L. Oniciu, **P. Ş. Agachi**
Mathematical model of a continuons working cell,
The 2-nd National Congress for Chemistry, Buc. , 7-10 sept. 1981

21. **P. Ş. Agachi**
Interaction of controller parameters in an electrochemical reactor.
Proceedings of the Faculty of Automation meeting, Buc. , sept. 1982

22. L. Oniciu, **P. Ş. Agachi**
Parametric approach of a fuel cell as an electrochemical reactor. Designing the minimum electrode surface,
Proceedings of the Faculty Chemical Technology meeting, 29-30 oct. 1982

23. L. Literat, **P. Ş. Agachi**, I. Batiu
Automatic control of a PVA process,
Proceedings of the Faculty of Chemical Technology, meeting, 16-17 dec. 1983

24. L. Oniciu, **P. Ş. Agachi**
Study of dynamic state of a fuel cell battery,
Proceedings of the Faculty of Chemical Technology, 16-17 dec. 1983

25. **P. Ş. Agachi**,
The study of dynamic behaviour of a 10 kW fuel cell battery,
Proceedings of the 2-nd National simposium on Methods, Models and Techniques in physics and related fields, oct. 14-15 University Babes-Bolyai, Cluj, 1983, p. 114

26. N. Palaghita, M. Bâtiu, **P. Ş. Agachi**, I. Bâtiu
Device for controlling the asincroneous motors rotation speed,
Proceedings of Electrotechnical Society, Buc. , febr 1984

27. **P. Ş. Agachi**, A. Dinga
Mathematical model of the PVC process,
Proceedings of the Faculty of Chemical Technology, 2-3 nov. 1984

28. **P. Ş. Agachi**, L. Morariu
Modal control of an ethanol distillation column,
Proceedings of the Faculty of Chemical Technology, 2-3 nov. 1984

29. **P. Ş. Agachi**, A. Imre, S. Laszlo
Programs for process computer control in chemical industry,
Proceedings of the Faculty of Chemical Technology, 2-3 nov. 1984

30. **P. Ş. Agachi**
Using the process computer in chemical industry,
Conference at the days of Cluj Academy, 26 nov. -1 dec. 1984

31. **P. Ş. Agachi**
Optimization of the electrochemical process taking place in a methanol/ air fuel cell,
The 36th ISE Meeting, Salamanca, Spain, September 23-28, 1985, Extended abstracts, p. 71-90

32. **P. Ş. Agachi**, D. Constantinescu, D. Macedon, L. Oniciu, V. Topan, I. Neacsu
Contributions at the diminishing energetic consumption of the brine electrolysis process.
Paper in the volume of the 11-th Meeting the Scientific Research Center Rm. Vilcea 10-12 oct. 1985, p. 1

33. **P. Ş. Agachi**, D. Constantinescu, V. Topan, L. Oniciu
Contributions at the reducing the energy consumption at the brine electrolysis process,
Proceedings of the 11-th Rm. Vilcea Research Center meeting, Rm. Vilcea, Calimanesti, 10-12 oct. 1985

34. **P. Ş. Agachi**, D. Constantinescu, V. Topan, L. Oniciu
Study concerning the influence of the electrolysis process parameters upon the cell voltage,
Proceedings of the 11-th Rm. Vilcea Research meeting, Rm. Vilcea, Calimanesti, 10-12 oct. 1985

35. **P. Ş. Agachi**, D. Constantinescu, V. Topan, L. Oniciu
Comparing study concerning the models of the brine electrolysis in cells with amalgame cathode,
Proceedings of the 11-th Rm. Vilcea Research Centre, Calimanesti, 10-12 oct. 1985

36. **P. Ş. Agachi**, I. Bâtiu
Automation and Computer Control of the PVA process,
Paper in the volume of the 4-th Conference of Chemical Engineering, Bucuresti, October 17-18 1985, p. 147

37. L. Oniciu, **P. Ş. Agachi**, V. Topan, D. Macedon, I. Neacsu
Mathematical model of a brine electrolysis cell,
The 37-th ISE Meeting, Vilnius, 1986, Ext. Abstr. vol. IX, p. 1256

38. S. Dumitrescu, L. Oniciu, **P. Ş. Agachi**
Simulation of the dynamic working and control of a fuel cell,
Revista de Chimie,7, 1986, p. 712

39. S. Dumitrescu, L. Oniciu, **P. Ş. Agachi**
Technological design of a 10 kW fuel cell battery,
Revista de Chimie, 37 (10), 1986, p. 1123

40. S. Dumitrescu, **P. Ş. Agachi**
Interaction of the control loops of a fuel cell 10 kW aggregate,
Revista de Chimie, 37(12), 1986, p. 1076-1079

41. **P. Ş. Agachi**, A. Faur
Mathematical model of the NaCl electrolysis,
Proceedings of the Faculty of Chemical Technology, march. 1986

42. **P. Ş. Agachi**
Optimization of the chemical processes and the using in the optimal control,
Conference at the days of the Cluj Academy, 18-21 nov. 1987

43. **P. Ş. Agachi**, P. Dobra
Mathematical model and optimal control of the brine electrolysis process,
Informatics symposium during the Days of the Cluj Academy, 18-21 nov. 1987

44. **P. Ş. Agachi**, V. Otoiu, S. Nemes
Mathematical models of the CaC_2 process,
Lecture at the 4-th Conference for Chemistry and Chemical engineering, Buc. 22-24 oct. 1987

45. **P. Ş. Agachi**, P. Dobra, L. Oniciu
Optimal control of an amalgam cathode brine electrolysis cell,
The Conference of Chemistry and Chemical Engineering, Buc. 22-24 oct. 1987

46. L. Oniciu, **P. Ş. Agachi**, P. Dobra
Saving energy through control at brine electrolysis amalgame cells,
The 39-th ISE Congress, Glasgow, 5-9 sept. 1988

47. **P. Ş. Agachi**
Mathematical modeling and optimal control of the chemical process
Conference at the "Lecturer's conference series", Faculty of Chemical Technology, 21 febr. 1988

48. **P. Ş. Agachi**
Expert system for the brine electrolysis process,
Paper in the Volume of the 20 -th Aniversary Meeting, IPG Ploiesti, 21-22 oct. 1988, p. 23-32

49. L. Oniciu, I. Bugan, **P. Ş. Agachi**
Optimization of the brine electrolysis process in amalgame cathode cells,
The 40-th ISE Congress, Kyoto, Japan, 1989

50. **P. Ş. Agachi**, I. Bâldea, F. Lajko, I. Kolcsar
Mathematical model of the PVC reactors,
The days of the Timisoara Academy, 27-28 May, 1989

51. L. Oniciu, I. Bugan, **P. Ş. Agachi**, A. Imre
Expert system for brine electrolysis process,
The 41-st ISE Congress, Prague, 25-26 Aug. 1990

52. **P. Ş. Agachi**, I. Diczig
Modelarea matematică a procesului de fabricare a carburii de calciu (I),
Revista de Chimie, 41(4), 1990, p. 333-336

53. **P. Ş. Agachi**, I. Diczig
Modelarea matematică a procesului de fabricare a carburii de calciu (II),
Revista de Chimie, 41(5-6), 1990, p. 455-460

54. **P. Ş. Agachi**
Concepts concerning computer control of brine electrolysis process, in cells with amalgam cathode,
Conference, Technical University Timisoara Symposium, 16 oct. 1990

55. **P. Ş. Agachi**
Trying to improve the PVC technology, using the computer modeling, optimization and control,
Conference, Veszprem University, Dept. of Chemical engineering, 27 June, 1990

56. **P. Ş. Agachi**
Computer control of brine electrolysis process,
Conference, Veszprem, Hungary, 26 Sept. , 1990

57. L. Oniciu, **P. Ş. Agachi**, A. Imre-Lucaci, Julia Socol
Computer control of brine electrolysis amalgam DeNora process,
The 42-nd ISE Meeting, Montreux, aug. , 25th-30th 1991, p. 538-542

58. **P. Ş. Agachi**
About the artificial intelligence. Expert systems in chemical engineering,
Conference at the Seminar of Physical chemistry Department, Fac. of chemistry and chemical engineering, Cluj, May,1991

59. **P. Ş. Agachi**
Possible use of the Pontryagin's maximum principle on the optimization of a methanol synthesis reactor,
Proceedings of the annual Conference of Chemical Engineering, 1991,oct. ,17, p. 3, Technical University Timisoara

60. **P. Ş. Agachi**
Mathematical model of Fluid Catalytic Cracking Unit,
Conference at the Petroleum and Gas Institute Ploiesti, November 22, 1992

61. **P. Ş. Agachi**
Design and Model Predictive Control of a FCCU,
National Meeting of Chemistry and Chemical Enginering, Bucuresti, 29-31 November, 1993

62. **P. Ş. Agachi**, A. Imre- Lucaci, I. Bunea
Using Neural Networks for modeling an Ion Exchange Membrane Electrolyser. Part I Analytical model,
Studia Universitatis "Babes-Bolyai", 1-2, 1994, p. 28-35

63. **P. Ş. Agachi**, I. Bunea
Using Neural Networks for modeling an Ion Exchange Membrane Electrolyser. Part II. Neural Network Models,
Studia Universitatis "Babes-Bolyai", 1-2, 1994, p. 36-44

64. **P. Ş. Agachi**
Computer Control of Chemical Processes,
Syposium of the 75th anniversary of the founation of the Cluj University, April 27-28, 1994

65. **P. Ş. Agachi**
Computer Control of pH of acidic waters, using dual base injection principle,
Conference at Eotvos Lorand University, Budapest, March 22, 1994

66. **P. Ş. Agachi**
Principles of the Industrial Electrochemistry,
Seminar at the Physical Chemistry Department of University of Budapest, March 23, 1994

67. **P. Ş. Agachi**
Model Predictive Control for Batch Processes,
Conference, Veszprem University, April 5, 1994

68. **P. Ş. Agachi**, E. Vass
Optimizarea reactorului de fabricare a metanolului, utilizand Principiul Maximului lui Pontriaghin,
Revista de Chimie, 6, 1995, p. 513-521

69. Z. Nagy, **P. Ş. Agachi**
Model Predictive Control of a PVC batch reactor,
Zilele Academice Timisorene, 22-25 Mai, 1995

70. M. Cristea, **P. Ş. Agachi**
Study of controllability of a FCCU plant, using Relative Gain Array method,
Volume of the Academic Days of Timisoara, Romania, May 25-27, 1995, vol II, p. 1-4

71. Z. Nagy, **P. Ş. Agachi**
Nonlinear Model Predictive Control of a PVC batch reactor,
Volume of the Academic Days of Timisoara, Romania, May 25-27, 1995, vol II, p. 64-67

72. **P. Ş. Agachi**
Modeling, Simulation and Control of Electrochemical Processes, a way to better efficiency (keynote lecture),
The 42-nd ISE Congress, Balaton fured, Sept. 1-5, 1996

73. **P. Ş. Agachi**, A. Imre-Lucaci, M. Cristea, Z. Nagy, L. Silaghi
Industrial System of Energy Management,
12th International Conference of Chemical and Process Engineering, CHISA '96, Prague, August 25-30, 1996

74. M. Cristea, **P. Ş. Agachi**
Mathematical Model of a UOP Type Cracking Unit,
12th International Conference of Chemical and Process Engineering, CHISA '96, Prague, August 25-30,1996

75. **P. Ş. Agachi**, M. Cristea
Controllability Study of a Fluid Catalytic Cracking Process,
12th International Conference of Chemical and Process Engineering, CHISA '96, Prague, August 25-30, 1996

76. **P. Ş. Agachi**, Z. Nagy
Model Predictive Control of a Model IV Fluid Catalytic Cracking Unit,
12th International Congress of Chemical and Process Engineering, CHISA'96, full paper, p. 1721, 25-30 August 1996, Prague

77. **P. Ş. Agachi**
Methods for Measuring sensitivity and Controllability for the Fluid Catalytic Cracking Process,
Automatic Control and Testing Conference, Cluj 23-24 May, 1996

78. Z. Nagy, **P. Ş. Agachi**
Nonlinear Model Predictive Control of a Continuous Fermentation Reactor using Artificial Neural Networks,
Automatic Control and Testing Conference, Cluj 23-24 May, 1996

79. **P. Ş. Agachi**, M. Cristea
Dynamic Simulator of a UOP Model Fluid Catalytic Cracking Unit,
National Seminar of Chemical Engineering, Timisoara, October 10-11, 1996

80. **P. Ş. Agachi**
Modeling, Simulation and Control of Electrochemical Processes, a way to Better Efficiency and a Cleaner Environment (invited plenary lecture),
Symposium of Chemistry and Chemical Technology, Rm. Valcea, 23-24 Oct. 1996

81. L. Oniciu, **P. Ş. Agachi**, J. Bugan, A. Imre
Steady State Model of the Electrochemical Process of Brine Electrolysis,
Hungarian Journal of Chemical Engineering, 25, 1997, p. 81-89

82. Z. Nagy, **P. Ş. Agachi**
Model Predictive Control of a PVC Batch Reactor,
Computers & Chemical Engineering, 6, 1997, p. 571-591

83. M. Cristea, **P. Ş. Agachi**
Dynamic Simulator for a UOP Model Fluid Catalytic Cracking Unit,
Studia Universitatis "Babes-Bolyai", Chemia, 42(1-2),1997, p. 97-102

84. M. Cristea, **P. Ş. Agachi**
Advanced Control of the Carbonation Reactor in the Ammonia Soda Product,
Revista Românã de Informaticã si Automaticã, Vol. 7 (4), 1997, p. 43-49

85. M. Cristea, V. Marinoiu, **P. Ş. Agachi**
Simulation and Model Predictive Control of a UOP Fluid Catalytic Cracking Unit,
11-th International Conference on Control and Computer Science, Bucharest, May1997, p. 166-170

86. M. Cristea, A. Imre, **P. Ş. Agachi**
New methods concerning the improvement of the flow measurement using computers,
Revista de Chimie, 49 (1), 1998, p. 50-55

87. M. Cristea, **P. Ş. Agachi**, C. Gobel
Sensitivity Analysis of an Industrial Dryer,
13th International Congress of Chemical and Process Engineering CHISA, CD-ROM of full text, 23-28 August, Praha, 1998

88. **P. Ş. Agachi**, Z. Nagy, A. Imre, M. Cristea, G. Szasz
Data acquisition and monitoring system of an industrial power station,
13th International Congress of Chemical and Process Engineering CHISA, CD-ROM of full text, 23-28 August, Praha, 1998

89. Anton A. Kiss, **P. Ş. Agachi**
Model Predictive Control of a PVC emulsion process,
13th International Congress of Chemical and Process Engineering CHISA, CD-ROM of full text, 23-28 August, Praha, 1998

90. Beatrix Budy, **P. Ş. Agachi**
Nonlinear models - inline neutralization of acid solutions with variable composition - new approaches,
13th International Congress of Chemical and Process Engineering CHISA, CD-ROM of full text, 23-28 August, Praha, 1998

91. Z. Nagy, **P. Ş. Agachi**
Nonlinear Model Predictive Control of a Continuons Fermentation Reactor using Artificial Neural Networks,
Artificial Intelligence in Industry, Conference, April 22-24, 1998, High Tatras, Slovakia, p. 207-215

92. M. Cristea, V. Marinoiu, **P. Ş. Agachi**
Rezultate privind simularea şi conducerea predictivă după model a instalaţiei de cracare catalitică de tip UOP,
Sesiunea Jubiliarã 50 de ani de la înfiintarea Universitãtii "Petrol-Gaze", Ploiesti, 1998

93. Z. Nagy, **P. Ş. Agachi**
Dynamic Modelling And Model Predictive Control of a Fermentation Bioreactor,
SiChem'98, Bucuresti, 1998, p. 450-460

94. M. Cristea, **P. Ş. Agachi**, A. Imre
Flow rate measurement using orifice plates in industrial implementation,
Simpozionul SIChem'98, 10-23 Oct. 1998, Bucuresti, p. 412-419

95. Anton A. Kiss, **P. Ş. Agachi**
Model Predictive Control of temperature of a PVC emulsion process,
Hungarian Journal of Industrial Chemistry, 27, 1999, p. ,117-124

96. M. V. Cristea, V. Marinoiu, **P. Ş. Agachi**
Multivariable Model Based Predictive Control of a UOP Fluid Catalytic Cracking Unit,
2nd Conference on Process Integration, Modeling and Optimization for Energy Saving and Pollution Reduction, PRES'99, May 31 - June 2, Budapest, Hungary, 1999, p. ,223-228

97. Z. Nagy, **P. Ş. Agachi**
Productivity Optimization of the PVC Batch Suspension Reactor Using Genetic Algorithm.
2nd Conference on Process Integration, Modeling and Optimization for Energy Saving and Pollution Reduction, PRES'99, May 31 - June 2, Budapest, Hungary, 1999, p. 487-492

98. Z. Nagy, **P. Ş. Agachi**
Distance Learning applied in an Introductory Data Acquisition Course,
The 5th International Conference on Computer Aided Engineering Education, CAEE'99, Sept. 22-24, 1999, Sofia, Bulgaria, p. 250-254

99. Z. Nagy, **P. Ş. Agachi**
DAQ System for Remote Monitoring and Control of a Laboratory Chemical Plant,
International Conference of "Molecular and Isotopic Processes", 23-25 September, 1999, Cluj-Napoca, p. 129

100. Z. Nagy, **P. Ş. Agachi**
Using Optimal Brain Surgeon for the Determination of the Topology of Artificial Neural Networks Used in the Dynamic Modeling of Chemical Processes,
The XI th Romanian International Conference on Chemistry and Chemical Engineering, RICCE-11, September 30 - 2 October, 1999, Bucharest, full paper on CD

101. M. V. Cristea, V. Marinoiu, **P. Ş. Agachi**
UOP FCCU Advanced Control,
The 11-th International Conference on Chemistry and Chemical Engineering, 30 Sept. -2 Oct, 1999, Bucuresti

102. Z. Nagy, **P. Ş. Agachi**,
Software pentru Curs Electronic de Achizitie de Date, cu Achizitie de Date la Distanta si Videoconferinta,
Revista Romana de Informatica si Automatica, 9 (3), 1999

103. Z. Nagy, **P. Ş. Agachi**, L. Bodizs
Adaptive Neural Network Model Based Nonlinear Predictive Control of Fluid Catalytic Cracking Unit,
European Symposium on Computer Aided Process Engineering-10, Elsevier Science, 7-11 May 2000, Florence, Italy, p. 235-240

104. M. Cristea, M. Baldea, **P. Ş. Agachi**
Model Predictive Control of an Industrial Dryer,
European Symposium on Computer Aided Process Engineering-10, Elsevier Science, 7-11 May 2000, Florence, Italy

105. **P. Ş. Agachi**, A. Imre-Lucaci
Control Strategies for brine Electrolysis by Ion Exchange Membrane Cell Process,
ESCAPE-10, 7-11 May 2000, Florence, Italy, in S. Pierucci editor, European Symposium on Computer Aided Process Engineering-10, Elsevier Science, 7-11 May 2000, Florence, Italy

106. Z. Nagy, L. Bodizs, R. Findeisen, M. Diehl, F. Allgower, **P. Ş. Agachi**, H. G. Bock, J. P. Schloder
A Comparison of First Principles and Neural Network Model Based Nonlinear Predictive Control of a Distillation Column,
AIChE Annual Meeting, Los Angeles, CA, USA, November 12-17, Paper No. 257h, 2000

107. V. M. Cristea, **P. Ş. Agachi**
Model Predictive Control of Hexamethylenetetramine Reactor Using Sensitivity Analysis for MPC Tuning,
2-nd International Conference of the Chemical Societies of the South-Eastern European Countries on Chemical Sciences for Sustainable Development, Halkidiki, Greece, 2000, Vol. II Abs. , p. 249

108. E. Rosca-Bocancea, **P. Ş. Agachi**
River Water Pollution Simulation Program,
14-th International Congress of Chemical and Process Engineering CHISA 2000, 27-31 August, Praha, 2000, on CD-ROM

109. Z. Nagy, **P. Ş. Agachi**. F. Allgower, R. Findeisen
Nonlinear model predictive control of a high purity distillation column,
14-th International Congress of Chemical and Process Engineering CHISA 2000, 27-31 August, Praha, 2000, on CD-ROM

110. A. M. Cormos, M. Cristea, **P. Ş. Agachi**, G. Zaha
Dynamic Simulation of the Calcium Carbonate Thermal Decomposition in Vertical Lime Kiln,
14-th International Congress of Chemical and Process Engineering CHISA 2000, 27-31 August, Praha, 2000, on CD-ROM

111. Al. Ozunu, **P. Ş. Agachi**,
Some Aspects concerning the Chemical Engineering Education at "Babes-Bolyai" University from Cluj-Napoca,
Proceedindings of 27th International Conference of Slovak Society of Chemical Engineering, 2000

112. C. Cormos, **P. Ş. Agachi**
Modeling and Simulation the Process of Synthesis of d,l Calcium pantothenate,
Q &A-R 2000, Cluj Napoca 19 - 20 th May, 2000 , Technical University of Cluj

113. M. Cristea, **P. Ş. Agachi**
Issues on Model Predictive Control Tuning ,
Q &A-R 2000, Cluj Napoca 19 - 20 th May, 2000, Technical University of Cluj

114. **P. Ş. Agachi**, G. Szasz
Adaptive PI Control of A Fermentation Bioreactor,
Q &A-R 2000, Cluj Napoca 19 - 20 th May, 2000, Technical University of Cluj

115. V. M. Cristea, **P. Ş. Agachi**
Model Predictive Control of Inferred Variables and Dynamic Sensitivity Analysis Applied to MPC Tuning,
SPC-2000 Symposium, Buletinul Universitatii "Petrol-Gaze" Ploiesti, Vol. LII, ST, No. 1/2000, p. 52-57

116. C. Cormos, **P. Ş. Agachi**
Modeling and simulation the synthesis process sodium pantothenate,
SICHEM 2000, october 3-6, 2000, Bucuresti, Papers of Chemical Engineering Symposium, p. 305

117. Ana-Maria Cormos, M. Cristea, **P. Ş. Agachi**
Simulation of the limestone thermal decomposition based on the granule dynamic model,
SICHEM 2000,3-6 octombrie 2000, Bucuresti, Papers of Chemical Engineering Symposium, p. 256

118. A. Imre, G. Szasz, Z. Nagy, A. Kiss, **P. Ş. Agachi**

Dynamic Modeling of Continuous Distillation. Comparison between Comercial Software,
In Proceedings of the 4th Conference on Process Integration, Modelling and Optimization for Energy Saving and Pollution Reduction-PRES'01,Florence, May 20-23, 2001, p. 345-348

119. Z. Nagy, **P. Ş. Agachi**, F. Allgower, R. Findeisen, M. Diehl, H. G. Bock, J. P. Schloder
Using Genetic Algorithm in Robust Nonlinear Model Predictive Control,
European Symposium on Computer Aided Process Engineering-11, ESCAPE-11, Denmark, May 27-30, 2001, p. 711-716

120. **P. Ş. Agachi**, Z. Nagy, A. M. Cormos
Artificial Neural Network (ANN) based dynamic simulator for thermal decomposition of the limestone, on the coke consuming),
Revista de Chimie, 52 (6), 2001, p. 330-334

121. M. V. Cristea, M. Baldea, **P. Ş. Agachi**
Multivariable Fuzzy logic Control of the Hexamethylene Tetramine Reactor,
Studia Universitatis "Babeş-Bolyai", Chemia, XLVI (1-2), 2001, p. 317-322.

122. A. M. Cormoş, M. Cristea, G. Zaha, **P. Ş. Agachi**, Al. Pop
Simulation of the Dolomite Thermal Decomposition based on the Granule Model,
Studia Universitatis "Babeş-Bolyai", Chemia,XLVI (1-2),2001,p. 323-327

123. M. V. Cristea, **P. Ş. Agachi**
Simulation and Model Predictive Control of the Soda Ash Rotary Calciner,
Control Engineering and Applied Informatics, Vol. 3, Nr. 4, 2001, p. 19-26

124. V. M. Cristea, **P. S. Agachi**, S. Zafiu
Simulation of an industrial rotary calcinator for soda ash production,
ICheaP-5 Congress, Florence 20-23 May 2001, p. 245-250

125. A. Bătinaş, Al. Pop, **P. S. Agachi**, F. Ciauşi
Kinetic studies for the SO_2 absorption in primary and secondary sodium phosphate,
28th International Conference of Slovak Society of Chemical Engineering, May 21 - 25, ISBN 80-227-1533-6, 2001, CD-ROM

126. A. Bătinaş, Al. Pop, C. Gherman, **P. S. Agachi**, C. Botar-Jid
Kinetic studies for the SO_2 chemosorption in ammonia spirit,
28th International Conference of Slovak Society of Chemical Engineering, May 21 - 25, ISBN 80-227-1533-6, 2001, CD-ROM

127. V. M. Cristea, **P. S. Agachi**, S. Zafiu

Control of an Industrial Rotary Calciner for Soda Ash Production,
Conferinta Internationala de Chimie si Inginerie Chimica RICCCE-12, Bucuresti, 2001

128. C. Cormos, **P. Ş. Agachi**
Modeling and simulation of 3-aminopropyonitrile sythesis using dedicated software packages,
Lucrarile Simpozoniului "30 ani de î învăţământ de Inginerie Chimica la Cluj-Napoca", 5-7 septembrie 2001

129. G. Szasz Z. Nagy, **P. Ş. Agachi**
Vapour-liquid in aqueos solutions of ammonia and carbon dioxide using neural networks,
Lucrarile Simpozoniului "30 ani de învăţământ de Inginerie Chimica la Cluj-Napoca", 5-7 septembrie 2001

130. M. V. Cristea, M. Bâldea, **P. S. Agachi**
Multivariable Fuzzy Logic Control of the Hexamethylene Tetramine Reactor,
Lucrarile Simpozoniului "30 ani de învăţământ de Inginerie Chimica la Cluj-Napoca", 5-7 septembrie 2001

131. G. Szasz, A. Imre-Lucaci , **P. Ş. Agachi**
Software for process simulation. Dynamic modeling of continuous distillation,
Lucrarile Simpozoniului "30 ani de învăţământ de Inginerie Chimica la Cluj-Napoca", 5-7 septembrie 2001

132. A. M. Cormos, M. Cristea, G. Zaha, **P. Ş. Agachi**, Al. Pop
Simulation of the dolomite thermal decomposition based on the granule model,
Lucrarile Simpozoniului "30 ani de învăţământ de Inginerie Chimica la Cluj-Napoca", 5-7 septembrie 2001

133. Z. K. Nagy, **P. Ş. Agachi**, R. Findeisen, F. Allgöwer, M. Diehl, J. P. Schlöder, H. G. Bock
The tradeoff between modeling complexity and real-time feasibility in nonlinear model predictive control,
Proceedings of The 6th World Multiconference on Systemics, Cybernetics and Informatics, Orlando, USA, volume VI, 2002, p. 329-334. (Best paper award on section Process ControI)

134. Z. K. Nagy, **P. Ş. Agachi**
A novel nonlinear model predictive approach for hybrid systems,
Proceedings of The 6th World Multiconference on Systemics, Cybernetics and Informatics, Orlando, USA, vol. VI, 2002, p. 335-340

135. V. M. Cristea, **P. Ş. Agachi**
Control of an Industrial Rotary Calciner for Soda Ash Production,
European Symposium on Computer Aided Process Engineering-12, May, The Hague, 2002, p. 463-468

136. M. V. Cristea, **P. Ş. Agachi**, M. V. Marinoiu
Simulation and Model Predictive Control of a UOP Fluid Catalytic Cracking Unit,
Chemical Engineering and Processing, Elsevier Science, vol. 42/2, 2002, p. 67-91

137. M. Bâldea, V. M. Cristea, **P. Ş. Agachi**
A Fuzzy Logic Approach to the Control of the Drying Process,
Hungarian Journal of Industrial Chemistry, vol. 30, 2002

138. C. Cormoş , **P. Ş. Agachi**
Modeling and Simulation of Sodium Beta-Alaninate Synthesis using dedicated software packages,
CHISA 2002 Congress, Praga, Cehia, 2002

139. C. Cormoş, **P. Ş. Agachi**
Modelling and simulation of beta-alaninate synthesis,
29-th International Conference of the Slovak Society of Chemical Engineering, Slovakia, 2002, CD-ROM

140. C. Cormoş, **P. Ş. Agachi**
Modeling and simulation of sodium beta-alaninate synthesis,
Proceedings of Q&A-R 2002 International Conference, Cluj-Napoca, 2002

141. V. M. Cristea, Raluca Roman, **P. Ş. Agachi**
Neural Networks Based Model Predictive Control of the Drying Process,
European Symposium on Computer Aided Process Engineering-13, Elsevier Science, Lappeenranta, Finland, 1-4 June, 2003, p. 389-394

142. M. V. Cristea, D. M. Libotean, **P. Ş. Agachi**,
Education in Chemical Process Control Using the Supervisory Laboratory Application,
Hungarian Journal of Industrial Chemistry, Vol. 31, p. 31-35, 2003

143. A. Ozunu, E. Cordoş, **P. Ş. Agachi**, M. Chitoanu, C. Roman, R. B. H. Mişca, A. Imre, C. Anghel, G. Şimon,
Realizarea unui centru regional pentru prevenirea accidentelor industriale majore (CRAIM),
Environment&Progress, 2003, p. 371-373

144. Z. K. Nagy, L. L. Simon, M. V. Cristea, **P. Ş. Agachi**, L. Jimenez, W. Schaufelberger,
A Distillation Telelaboratory for Distance CAPE Education,
Proceedings of the 2003 WFEO/ASEE e-Conference, 2003 American Society for Engineeering Education

145. V. M. Cristea, C. Maniut, A. M. Cormos, **P. Ş. Agachi**
Simulation of Calcium Carbonate Decomposition in the Rotary Calciner,
30th Conference SSCHE, Proceedings on CD-ROM, Tatranske Matliare, Slovacia, 26-30 May, 2003

146. C. Cormos, **P. Ş. Agachi**,
Modeling and simulation of pantolactone synthesis,
Studia Universitatis "Babeş – Bolyai", Chem. , XLIX (2), Cluj – Napoca, Romania, 2004, p. 13 – 22

147. C. Cormos, **P. Ş. Agachi**,
Modeling and simulation of residual pantolactone extraction from calcium pantothenate solution,
Studia Universitatis "Babeş – Bolyai", Chem. , XLIX (2), Cluj – Napoca, Romania, 2004, p. 23 – 32

148. Mircea V. Cristea, Dan M. Libotean, **P. Ş. Agachi**
Computer Aided Process Control Laboratory,
Computer Aided Process Engineering Education Forum, Veszprem Ungaria, Feb. 2004

149. C. Cormos, **P. Ş. Agachi**
Modeling and simulation of sodium beta-alaninate synthesis: comparison between comercial softwares,
16-th International Congress of Chemical and Process Engineering, Prague, Czech Republic, 22 – 26 August 2004

150. C. Cormos, **P. Ş. Agachi**
Modeling and simulation of pantolactone extraction process,
16-th International Congress of Chemical and Process Engineering, Prague, Czech Republic, 22 – 26 August 2004

151. Z. K. Nagy, **P. Ş. Agachi**
Internet-based interactive remote laboratory for educational experiments,
Proc. of the AIChE Annual Meeting, Austin, TX, in Session New Technologies for Experimentation over the Internet, Paper 528e, full paper on CD, November 7-12, 2004

152. V. M Cristea, D. Libotean, **P. Ş. Agachi**
Tehnici Moderne de Experimentare şi Învățământ în Informatica de Proces,
A XXVIII Conferință Națională de Chimie, oct. 2004, p. 320

153. **P. Ş. Agachi**, Z. Nagy, M. V. Cristea, A. Imre
New e-Learning Development at UBB Cluj-Napoca,
Workshop on e-Learning in Engineering Education, Bucureşti, 2004

154. C. Cormos, **P. Ş. Agachi**
Modeling and simulation of sodium pantothenate synthesis using ChemCAD,
International Conference on Automation, Quality and Testing, Robotics A&QT-R 2004 (THETA 14), Cluj – Napoca, Romania, 13 – 15 May 2004

155. Z. K. Nagy, **P. Ş. Agachi**, F. Allgower
Nonlinear model predictive control of a pilot distillation column. An artificial intelligence approach,
Proc. of the IEEE-TTTC International Conference on Automation, Quality and Testing, Robotics (A&QT-R 2004, THETA 14), Cluj-Napoca, Romania, Vol. 1, 141-146, May 13-15, 2004

156. Z. K. Nagy, R. Roman, **P. Ş. Agachi**, F. Allgöwer
A real-time approach for moving horizon estimation based nonlinear model predictive control of a fluid catalytic cracking unit,
Proc. 7th World Congress of Chemical Engineering, Glasgow, Scotland, July, 2005

157. M. V. Cristea, L. Toma, **P. Ş. Agachi**
Neural Networks Used for Model Predictive Control of the Fluid Catalytic Cracking Unit,
7-th World Congress of Chemical Engineering, Glasgow, June 2005, on CD-ROM

158. R. Roman, Z. K. Nagy, **P. Ş. Agachi**, F. Allgöwer
Dynamic modeling and nonlinear model predictive control of a fluid catalytic cracking unit,
European Symposium on Computer Aided Process Engineering-15, Elsevier Science, Barcelona, Spain, May, 2005

159. C. Cormos, **P. Ş. Agachi**
Advanced process control of pantolactone synthesis using nonlinear model predictive control (NMPC),
European Symposium on Computer Aided Process Engineering-15, Elsevier Science, Barcelona, Spain, May 2005, p. 1435-1440

160. D. Brătfălean, **P. Ş. Agachi**, D. F. Irimie
Utilization of Runge Kutta method for solving differential equations in Enzyme Catalysis on sunflower oil,
Tutorial course Marie Curie Understanding molecular simulations Oct. 24 - Nov. 04 2005 University of Amsterdam

161. A. M. Cormos, C. Cormos, A. Friedl, **P. Ş. Agachi**
Simulation of the scrubbing unit waste incineration plant using ChemCAD, 8-th Conference on Process Integration, Modeling and Optimisation for Energy Saving and Polution Reduction – PRES'05, Girardini Naxos, Italy, 15 – 18 May 2005

162. C. Cormos, A. M. Cormos, **P. Ş. Agachi**
Retrofit study of racemic calcium pantothenate synthesis,
32-nd International Conference of Slovak Society of Chemical Engineering, Tatranske Matliare, Slovakia, 23 – 27 May 2005, CD-ROM

163. C. Cormos, **P. Ş. Agachi**,
Modelarea si simularea extractiei pantolactonei folosind programul ChemCAD,
Revista de Chimie, 56 (7), 2005

164. C. Cormos, A. M. Cormoş, **P. Ş. Agachi**
Modeling and simulation of ammonia recovery process in soda-ash plant,
Revista de Chimie, 56 (11), 2005

165. **P. Ş. Agachi**
Computer Aided Process Engineering,
Proceedings of the Romanian Academy, Series A, Volume 6, No. 1, p. 85-90, 2005

166. Z. K Nagy, R. Roman, F. Allgöwer, **P. Ş. Agachi**
First principles modeling and nonlinear optimization based estimation and control of a fluid catalytic cracking unit,
Studia Universitatis Babeş-Bolyai Seria Chemia Journal, Romania, 2005

167. A. M. Cormos, C. Cormos, **P. Ş. Agachi**
Modeling and simulation of thermal decomposition of limestone in a vertical lime kiln,
Studia Universitatis "Babeş – Bolyai", Chem. , L (1), Cluj – Napoca, 2005

168. C. Cormos, A. M. Cormos, **P. Ş. Agachi**
Modeling and simulation of the carbonation process of ammoniacal brine using ChemCAD,
Studia Universitatis "Babeş – Bolyai", Chem. , L (1), Cluj – Napoca, Romania, 2005, p. 277-288

169. C. Cormos, A. M. Cormos, A. Friedl, **P. Ş. Agachi**,
Modeling and simulation of the scrubbing unit waste incineration plant,
Studia Universitatis "Babeş – Bolyai", Chem. , L (1), Cluj – Napoca, Romania, 2005, p. 289-296

170. Claudiu. C. Botar-Jid, D. Fissore, **P. Ş. Agachi**, Antonello A. Barresi
Selective Catalytic Reduction of NO_x with NH_3 in unsteady-state reactors,
Studia Universitatis "Babeş – Bolyai", Chem. , L (2), Cluj – Napoca, Romania, 2005

171. Mircea V. Cristea, **P. Ş. Agachi**
Neural Networks Applications in Chemistry and Chemical Engineering,
Computer Aided Chemical Engineering Forum 2005, Cluj-Napoca, 2005

172. **P. Ş. Agachi**, I. Stoian, E. Stâncel, M. Cristea, S. Dragan, O. Ghiran, D. Capatâna, A. Imre, A. Ghirisan, St. Hegedus, C. Posteuca,
Monitoring system for air pollution generated by industrial plants with wireless components,
Computer Aided Chemical Engineering Forum 2005, Cluj-Napoca, 2005

173. R. Roman, Z. K. Nagy, M. V. Cristea, F. Allgöwer, **P. Ş. Agachi**
Complex Dynamic Modeling and Linear Model Predictive Control of Fluid Catalytic Cracking Process,
Romanian International Conference on Chemistry and Chemical Engineering RICCCE-14, Bucuresti, Romania, September, 2005, Vol. 3, p. 116-123

174. **P. Ş. Agachi**
Ingineria de Proces Asistată de calculator,
Conferință la Secția de Tehnologia Informației a Academiei Române, 31 ian. , 2005

175. D. Brătfălean, Maria V. Morar, D. F . Irimie, **P. Ş. Agachi**
Comparative study for sunflower Oils extraction by Soxhlet and Mechanical press methods,
Bulletin of USAMV-CN nr. 63, 2006**,** ISSN 1454-2382

176. D. Brătfălean, D. F. Irimie, **P. Ş. Agachi**, D. Stanciu, I. Sorega
Variability study of fats acids on 13 Romanian genotype of sunflower oil by Gas Chromatography,

Cercetări de Genetică Vegetal şi Animală, vol IX/2006 Academy of Agricultural and Forestry Science, Bucharest, ISSN 1224-0436 p. 31-37

177. Cormos Calin-Cristian , Cormos Ana-Maria, **P. Ş. Agachi**
Modeling and simulation of carbonation process of ammoniacal brine solution in soda ash plant,

Revista de Chimie, 57 (2), 2006, p. 130-137

178. Cormos Ana-Maria, Cormos Calin-Cristian , **P. Ş. Agachi**
Modeling and simulation of the ammonia absorption process in sodium chloride solution using chemcad,

Studia Universitatis Babeş-Bolyai, Chemia, LI (2), 2006, p. 215-222

179. A. M. Cormoş, C. C. Cormoş, **P. Ş. Agachi**
Modeling and simulation of the limestone decomposition process in the vertical lime kiln with coke,
Zilele Academice Clujene, 2006

180. V. M. Cristea, A. Imre-Lucaci, Z. K. Nagy, **P. Ş. Agachi**
E-tools for education and research in chemical engineering,
Zilele Academice Timisene, 2006

181. V. Pleşu, **P. Ş. Agachi**
Emphasize the continuity and diversity of Computer Aided Process Engineering (CAPE)
Revista de chimie, 58 (4), 2007, p. I

182. M. V. Cristea, **P. Ş. Agachi**
Comparison Between Different Control Approaches of the UOP Fluid Catalytic Cracking Unit
Revista de chimie, 58 (4), 2007, p. 406-409

183. . M. V. Cristea, **P. Ş. Agachi**
Artificial Neural Networks Based Model Predictive Control of the Wastewater Treatment Plant,
17th European Symposium on Computer Aided Process Engineering, Elsevier Science, Bucharest, Romania, 27-30 May, 2007, CD-ROM, p. 1-6

184. D. Brătfălean, M. V Cristea, **P. Ş. Agachi**, D. F. Irimie, A. Sarrafi, M. Petitprez
Evaluation of sunflower collection by genetic variability based on germination and plantlet development parameters using Artificial Neural Networks,
17th European Symposium on Computer Aided Process Engineering, Elsevier Science, Bucharest, Romania, 27-30 May, 2007, CD-ROM

185. R. Roman, Z. K. Nagy, **P. Ş. Agachi**
First principle modeling of an industrial Fluid Catalytic Cracking – the adaptation of the model,
17th European Symposium on Computer Aided Process Engineering, Elsevier Science, Bucharest, Romania, 27-30 May, 2007, p. 87-92

186. A. M. Cormoş, C. C. Cormoş, **P. Ş. Agachi**
Making soda ash manufacture more sustainable. A modeling study using ASPEN Plus,
17th European Symposium on Computer Aided Process Engineering, Elsevier Science, Bucharest, Romania, 27-30 May, 2007, p. 551-556

187. M. V. Cristea, **P. Ş. Agachi**
Comparison between Different Control approaches of the UOP Fluid Catalytic Cracking Unit,
17th European Symposium on Computer Aided Process Engineering, Elsevier Science, Bucharest, Romania, 27-30 May, 2007, p. 847-852

188. C. C. Botar-Jid, **P. Ş. Agachi**, D. Fissore
Comparison of reverse flow and counter-current reactors in case of selective catalytic reduction of NOx,
17th European Symposium on Computer Aided Process Engineering, Elsevier Science, Bucharest, Romania, 27-30 May, 2007, p. 1331-1336

189. Ani Elisabeta-Cristina, **P. Ş. Agachi**
Numerical models to simulate pollution scenarios in Somes River,
Paper 2029 in: Gani R. and Dam-Johannsen K. , 6th European Congress of Chemical Engineering (ECCE-6) Proceedings book, volume 1, 2007, p. 985

190. C. C. Botar-Jid, Y. Avramenkob, A. Kraslawski, **P. Ş. Agachi**
Decision support system for unsteady-state reactors design using case-based reasoning approach,
Paper 1977 in: Gani R. and Dam-Johannsen K. , 6th European Congress of Chemical Engineering (ECCE-6) Proceedings book, volume 1, 2007, p. 439-440

191. D. Brătfălean, M. V. Cristea , D. F. Irimie , **P. Ş. Agachi**
Comparative fatty acids content of sunflower seeds of Romanian inbred lines genotypes using Artificial Neural Networks,
European Congress of Chemical Engineering (ECCE-669), Copenhagen, 16-20 September 2007

192. D. Brătfălean, D. F. Irimie, **P. Ş. Agachi**
Investigation of oil extraction from sunflower seeds varieties using different techniques. Modeling of extraction process,
CAPE FORUM, 1. -2 February, Maribor, Slovenia, 2007

PATENTS

1. L. Oniciu, V. Topan, **P. Ş. Agachi**, V. Florea
Heterogeous ion-exchange membrane,
pat. OSIM, nr. 71154/24. 04. 1979

2. Silberg Ioan, Topan Vasile, **P. Ş. Agachi**, Baldea Ioan
Method and reactor for chloramine preparation,
Dosar OSIM 120813/25 nov. 1985, nr. brevet 93338/2. 09. 87

3. I. Baldea, I. A. Silberg, V. A. Topan, P. Eftimie, **P. S. Agachi**, M. Veszeny, M. Brie, L. Oniciu
   Method for 3,3-dialchil-diaziridine and dialchilcetazine preparation,
   Dosar OSIM 120895/25nov. 1985, nr. brevet 93340/2. 09. 87
4. V. A. Topan, I. A. Silberg, **P. S. Agachi**, F. Eftimie, M. Veszeny, M. Brie, I. Baldea, L. Oniciu
   Method for obtaining hydrazine sulphate from the water solution of 3,3-dialchil-diaziridine and dialchilcetazine,
   Dosar OSIM 120896/25 nov. 1985, nr. brevet 93341/25. 11. 85
5. L. Oniciu,I. A. Silberg, V. A. Topan, F. Eftimie, **P. S. Agachi**, M. Veszeny, M. Brie, I. Baldea
   Method for obtaining hydrazine hydrate,
   Dosar OSIM 120849/25nov. 1985, nr. brevet 93339/25. 11. 85
6. L. Oniciu, V. A. Topan, I. Bugan, C. Popescu, **S. Agachi**, M. Schenker
   Electrochemical transducer, for sodium concentration in amalgam, for electrolysis mercury cathode cells,
   Nr. 103118/01. 02. 1989

ACADEMIC MANAGEMENT PAPERS

1. **P. S. Agachi**, L. Ilies, M. Miclea
   Strategic Plan of Babes-Bolyai University 2000-2003, October 1999
2. **P. S. Agachi** and collective
   Charter of Babes-Bolyai University, July 2000
3. Andrei Marga, **P. S. Agachi**, V. Cristea, C. Baba
   Strong points and weak points - a self evaluation made by Rector's office of the Babes-Bolyai University at the request of the Association of European University evaluation team,
   Volume The institutional evaluation of the "Babes-Bolyai" University, p. 203, Presa Universitară Clujeană, 2001
4. **P. S. Agachi**
   Science between State and Market, a university perspective, Experts' meeting "Cooperation between Business and Science", in preparation of 4th Danube Region Conference, Bucharest, 8-10 October, 2003
5. **P. S. Agachi**, Stela Andrei, Romana Cramarenco, Marcel Ciprian Pop, Carmen Pop
   The Babes-Bolyai university and the interaction with its environment, case study - Experts' meeting "Co-operation between Business and Science", 4th Danube Conference, Bucharest, October 8-10, 2003

6. **P. S. Agachi**
   Issues and actions after the evaluation of EUA, May 2001, volume The institutional evaluation of the "Babes-Bolyai" University, p. 251, 2001
7. **P. S. Agachi**
   Status of Higher Education in Northern Iraq, Erbil 2002, UNESCO document
8. **P. S. Agachi**
   Analysis of the status of HE in Northern Iraq, based on international indicators of quality, Erbil 2002, UNESCO document
9. **P. S. Agachi**
   Outcomes of the European University Association at Babes-Bolyai University, 5th EUA meeting, Cluj-Napoca, Romania, October 23-25, 2003
10. **P. S. Agachi** Multicultural Policy of "Babes-Bolyai" Univesity, April 1997, Document presented at the Senate Meeting defining the multicultural policy of BBU
11. **P. S. Agachi** and collective
    Strategic Plan of Babes-Bolyai University 2004-2007, July 2003
12. **P. S. Agachi**
    Report concerning Iraq Higher Education -, Paris, UNESCO Rapid Needs Assessment team document, November 2003
13. **P. S. Agachi,** Carmen Loredana Pop
    Entrepreneurial university-University experiences in the field, Presa Universitară Clujeană, Noiembrie 2004
14. **P. S. Agachi**
    Consequences after European University Association Evaluation at Babes-Bolyai University -EUA Alumni Meeting, EUA Maastricht Conference, 28-30 October 2004
15. **P. S. Agachi**
    Performante si clasificari internationale. Metodologie de aplicare. Masa rotunda organizata de UNESCO CEPES si Fundatia Elias a Academiei Romane pe tema: Noi politici in domeniul invatamantului superior si cercetarii stiintifice din Romania, UNESCO-CEPES, Bucuresti, 22 martie 2005

ANUL LII **2007**

S T U D I A

UNIVERSITATIS BABEŞ – BOLYAI

C H E M I A

2

Desktop Editing Office: 51ST B.P. Hasdeu, no. 24 Cluj-Napoca, Romania, phone +40 264-40.53.52

CUPRINS – CONTENT – SOMMAIRE – INHALT

STUDIA UNIVERSITATIS BABEŞ-BOLYAI, CHEMIA, LII, 2, 2007

FUEL CELLS AND NANOPARTICLES

CRINA SUCIU*, ALEX C. HOFFMANN, ARILD VIK***, FIRUTA GOGA***

ABSTRACT. Many new chemical methods are being developed and existing ones modified in order to improve the particles produced and the cost-effectiveness of the process. In our project, yttria stabilized zirconia (YSZ) nanoparticles with a mean particle diameter between 7 and 10 nm have been obtained using a calcination temperature of only 500°C through a modified sol-gel method using two new organic precursors: sucrose and pectin. These precursors are a good solution to the disadvantages presented for the sol-gel method, being cost-effective, ubiquitous and environmentally friendly. The calcination process was studied by thermal analysis (TA) and the crystal structure is analyzed by XRD The particle size was determined by Transmission Electron Microscopy (TEM), supported by the X-ray Diffraction (XRD) determination of the crystallite size using the Scherrer formula, and the Brunauer, Emmet, and Teller (BET) adsorption analysis used to determine the specific surface area.

INTRODUCTION

As reserves for the common fossil fuels become smaller and their use lead to important pollution, alternative energy sources and processes are increasingly the focus of research and development. Fuel cells are electrochemical cells that generate electricity through the oxidation of hydrogen or another gaseous fuel (rich in hydrogen), mostly using oxygen from the air. [1-3].

The materials that constitute the electrolyte and the electrodes determine the type of the fuel cell [4]. In SOFCs, all three components are made from ceramic materials. SOFCs are distinguished from other fuel cell types by: the solid electrolyte; the highest working temperature; a high efficiency; simplicity and their ability to generate electricity directly from

* Faculty of Chemistry and Chemical Engineering, "Babes-Bolyai" University, Arany Janos Street 11, 400028, Cluj Napoca, Romania, Tel: 40-264-593833, Fax: 40-264-593833, csuciu@chem. ubbcluj. ro

** University of Bergen, Institute of Physics and Technology,Allegaten 55, 5007, Bergen, Norway

*** Prototech AS, Fantoftveien 38, Bergen, Norway

hydrocarbon fuels, meaning that, for instance, all of hydrogen (H2), carbon monoxide (CO) and methane (CH4) can be used as fuels, the second one being a poison when used in most other types of fuel cell [2, 5].

The solid electrolyte is an oxidic material, most often yttrium stabilized zirconia (YSZ) [6]. Adding a small percentage of Y_2O_3 to ZrO_2 has two effects: i) it stabilizes the cubic structure of zirconium oxide at all temperatures and ii) substituting some tetravalent zirconium ions with trivalent yttrium ions gives rise to oxygen ion vacancies in the crystal structure. [7].

The YSZ electrolyte must be dense, i. e. free of porosity, it must possess high oxygen ion conductivity and a minimal electronic conductivity, it must have high mechanical strength, good chemical stability and durability and it must be compatible with the other components (the electrodes) in terms of thermal expansion. [7, 9-11].

The working principle of a fuel cell is depicted in Figure 1. As gaseous oxygen is fed into the porous cathode, the molecules are split on the cathodic catalyst, which consumes electrons, and $O2_i$ ions pass into the electrolyte. The electrolyte conducts these ions through oxygen vacancies toward the anode. Here these ions, together with hydrogen from a fuel, form water, which releases electrons. These electrons are conducted through the anode material and captured by a current collector behind the anode and further through an external circuit and a cathodic current collector to the cathode, where they are again consumed in the cathodic process [1-3, 7, 8].

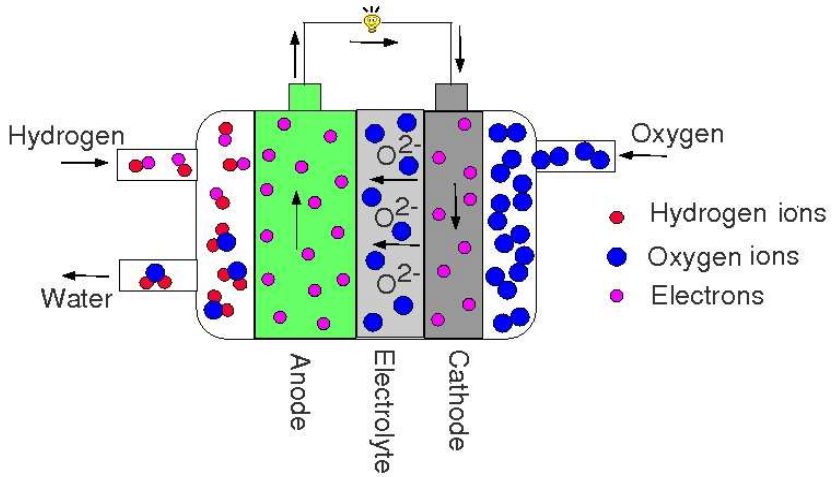

Figure 1. SOFC principle. The electrodes are porous, so that the gaseous molecules actually penetrate right down to the electrolyte

As mentioned, SOFCs use a catalyst (metallic, usually nickel) on one or both electrodes to increase the rate of a reaction without being consumed in the processes [7, 8]. The electrochemical reactions involve gaseous reactants and/or products, ionic reactants and/or products and electrons. The electrochemically active region therefore needs to be accessible to all three of these species, and is thus on the interface between the pores transporting the gaseous reactants/products, the electrolyte conducting the ions, and the catalyst in the electrode conducting electrons. This interface represents the \triple-phase boundary" (TPB) and the efficiency of the electrochemical reactions of the cell depend on its extent (see Figure 2) [12-17].

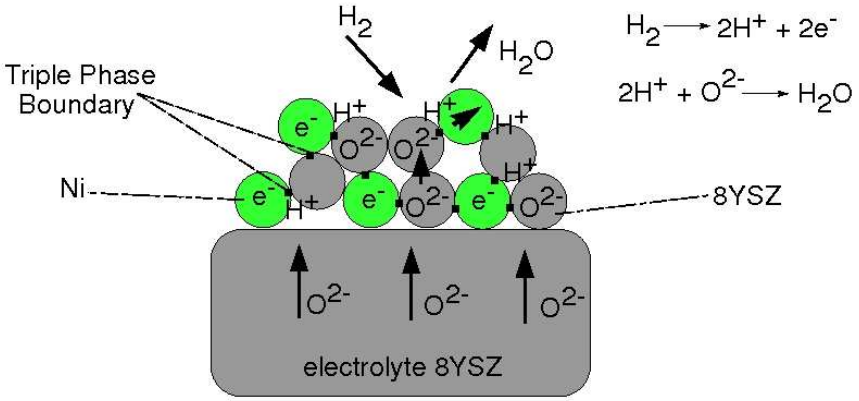

Figure 2. SOFC triple-phase-boundary (TPB). Often, as also depicted in this figure, particles of electrolyte material penetrate into the electrode, increasing the TPB

Our research project is focused on producing nano-sized powders for use as precursors for manufacture of SOFC components. In the manufacture, using nanoparticles gives rise a decrease in the required temperature of sintering, an improvement in the homogeneity of the produced films, a more homogeneous distribution of the doping elements, increased homogeneity of the microstress distribution, enhanced mechanical properties under temperature change and enhanced gas passage through the electrodes [18].

There are a multitude of different processes to produce nanoscaled materials today. These are usually classified into *physical methods* (e. g. plasma spraying [19, 20], flame synthesis [21, 22], electrostatic atomization [23], microwave flash synthesis [24], *chemical methods* (e. g. sol-gel [25-27], precipitation [28-30]) and mixed *chemical-physical methods* (e. g. spray pyrolysis [31, 32], flame-spray synthesis [33]).

Concentrating on chemical methods used for producing zirconia-based nanoparticles, present common advantages such as low costs, good control of stoichiometry, good mixing of the starting materials and good chemical homogeneity of the product. On the other hand, particle agglomeration and costly chemical precursors are a few disadvantages of this type of method.

In this paper, we focused on obtaining ultra fine zirconia powders. Traditional organic precursors for the sol-gel process have been replaced with sucrose and pectin, an alternative which has not been tried out before. The aim was to synthesize the powder and characterize it using thermal analysis, transmission electron microscopy, scanning electron microscopy, X-ray diffraction, and BET analysis.

EXPERIMENTAL

The common salts $ZrCl_4$ (Sigma-Aldrich, technical purity) and $Y(NO_3)_3 \cdot 6H_2O$ (Sigma-Aldrich, 99. 9% purity) were used as zirconia and yttria precursors, respectively. The process followed the floe chart presented in Figure 3. Zirconium chlorate was dissolved in distilled water on a warming plate at 100°C. Next, the yttrium nitrate for a final composition of 8mol% Y_2O_3 to ZrO_2 were calculated, weighed and added to the solution. After the homogenization, a sucrose / pectin mixture with a mass ratio of 4:0. 1 was added to the solution under continuous stirring and the pH of the final solution is between 0. 5–1.

The aim of the stirring under heating treatment is to maintain the degree of dispersion on an advanced scale, to prevent agglomeration of the constituent particles and to avoid their solidification into crystals. The thermal treatment continues and the mixture is dried at 90–100°C and is allowed to stand for 2h. During this, from the clear solution the sol and the gel are gradually formed. The thermal treatment is mainted for another 2-3h until the mixture becomes completely gelatinized and the dried gel (xerogel) is formed. The xerogel is then subjected to a calcinations thermal treatment in order to be transformed into YSZ nanoparticles. The thermal treatment used for the samples at 500°C has a 6h plateau at the maximum temperature at a heating/cooling rate of 100°C/h. The samples obtained at 1000°C the thermal treatment has 1h plateau at the maximum temperature at a heating/cooling rate of 100°C/h.

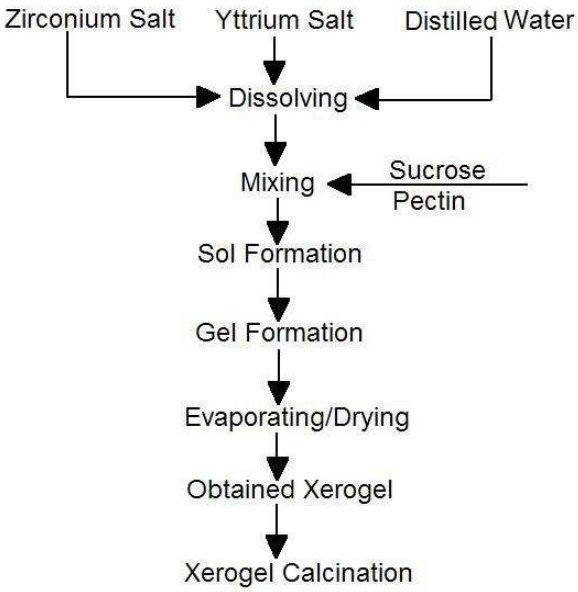

Figure 3. The flowing chart for the YSZ nanoparticles preparation

RESULTS AND DISCUSSIONS

The evolutions of the dried gel was recorded by *Thermal Analysis (TA)* using a Derivatograph Q 1500 (MOM Hungary) based on the F. Pauli, J. Pauli and L. Erdey principle. Small samples of dried gel were taken from the sample was analyzed as a function of temperature at a heating rate of 10^{o}C/min. The TA results are shown in Figure 4.

The DTA curve has shown a strong exothermic process which is starting at 280-300^{o}C and continues up to 850^{o}C. The inflexion points observed at 450^{o}C and between 650^{o}C and 850^{o}C attributed to oxidation of the organic compounds, ZrO_2 formation, and the formation of solid solution between ZrO_2 and Y_2O_3. Because the processes are overlapped it is difficult to limit the intervals attributed to each process.

The TG curve shows a process with little mass losses at the temperature of 100^{o}C due to the water elimination, followed by a higher mass loss at 300^{o}C and a slower mass loss up to 700^{o}C. The total losses were 56%.

After passing the temperature of 850^{o}C no processes can be observed either on the mass variation curves TG or on the DTA curve.

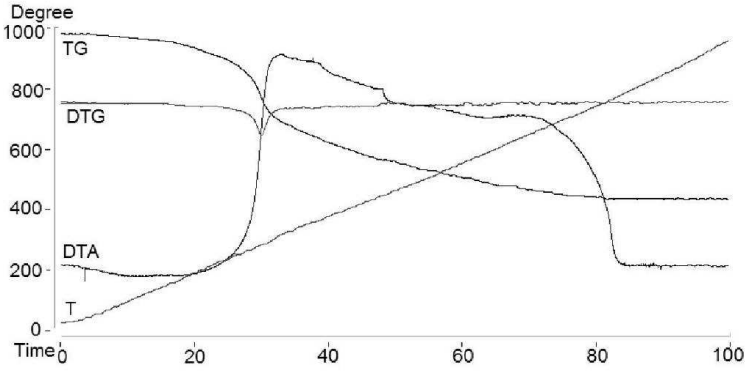

Figure 4. TA analysis of the YSZ gel

The X-ray diffraction spectra were obtained by Brucker D-8 Advance X-ray diffractometer using a Cu K-α radiation. The unit cell parameter accuracy was $\pm 10^{-3}$Å. The intensities were measured from 20 to 100° with a counting rate of 3 s per scanning step. The obtained spectra showed that the obtained nanoparticles at temperatures of 500 and 1000°C are stabilized in cubic crystal form (see Figure 5). The presence of other was not observed.
The Scherrer formula applied on the first four peaks of the obtained XRD spectrum was used in order to determine the crystallite size of the particles. The Cukα1 radiation value used for determination was 0. 15406 nm and the k value equal with 1. The crystallites size increase with increasing the temperature from 7 nm at 500°C to 33 nm at 1000°C.

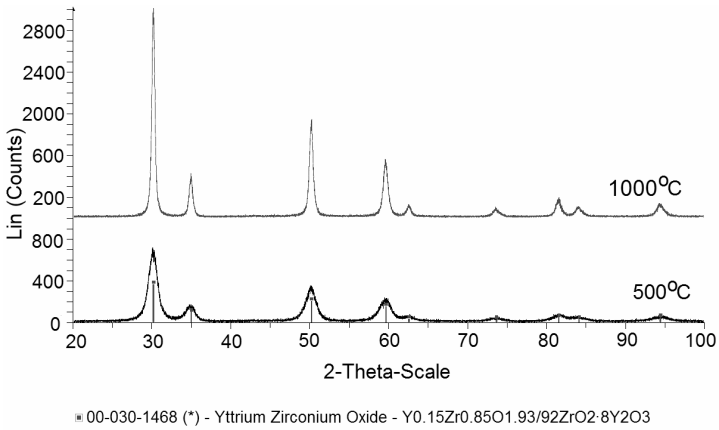

Figure 5. XRD spectra of the YSZ samples at 500 and 1000°C

The specific surface area was determined from *nitrogen adsorption* using a Gemini 2380 from Micromeritics. The samples were degassed at 300°C for 3 hours under vacuum before analysis. At 500°C high singlepoint and multipoint BET values were obtained corresponding to 80 m^2/g and 83m^2/g, respectively. At 1000°C the singlepoint and multipoint values decrease to 8. 2 m^2/g and 8. 6 m^2/g, respectively. The particle size was calculated assuming that the particles are round and that the density of the cubic ZrO_2 is 5900 kg/m^3. In this way, particle of 12 nm are obtained at 500°C and around 120 nm at 1000°C. In agreement with the XRD data, the BET values show that the smallest particle sizes are obtained at low temperatures while increasing the temperature the particle size also increases.

Figure 6 shows the *transmission microscope* images of the obtained YSZ particles. The images were obtained using a JEOL-JEM-1011 transmission microscope. The used copper grids during TEM investigations were subjected to a carbon deposition followed by a glow discharge. In the meantime, the powders were dispersed in distilled water under stirring and one drop taken from the solution was deposited on the prepared copper grid.

The morphology of all samples has shown relatively uniform and round shapes with a narrow size distribution. Particles around 8 nm are obtained at 500°C and around 55 nm at 1000°C. For the particles obtained at 500°C can easily be seen that the individual particles are easy to distinguish, and are not agglomerated to a very large degree in contrast to the particle obtained at 1000°C. At the highest temperature the particle very easily form agglomerates and the particles are difficult to distinguish.

In figure 7 *scanning microscope* picture of the sample obtained at 1000°C is presented. Large agglomerates with the mean particle size around 53 nm are obtained.

CONCLUSIONS

It is possible to produce YSZ nanoparticles in relatively simple conditions and at low costs. The new organic precursors (sucrose and pectin) are cheap, non-toxic, available at industrial scale, easy to store and manipulate at low temperatures. The method is environmentally friendly since it is water based and uses two natural compounds as organic precursors.

The results have shown that the new sol-gel method can be easily use to obtain nanoscaled powders for the sintering of YSZ ceramics with the aim of manufacturing SOFC electrolytes or anodes.

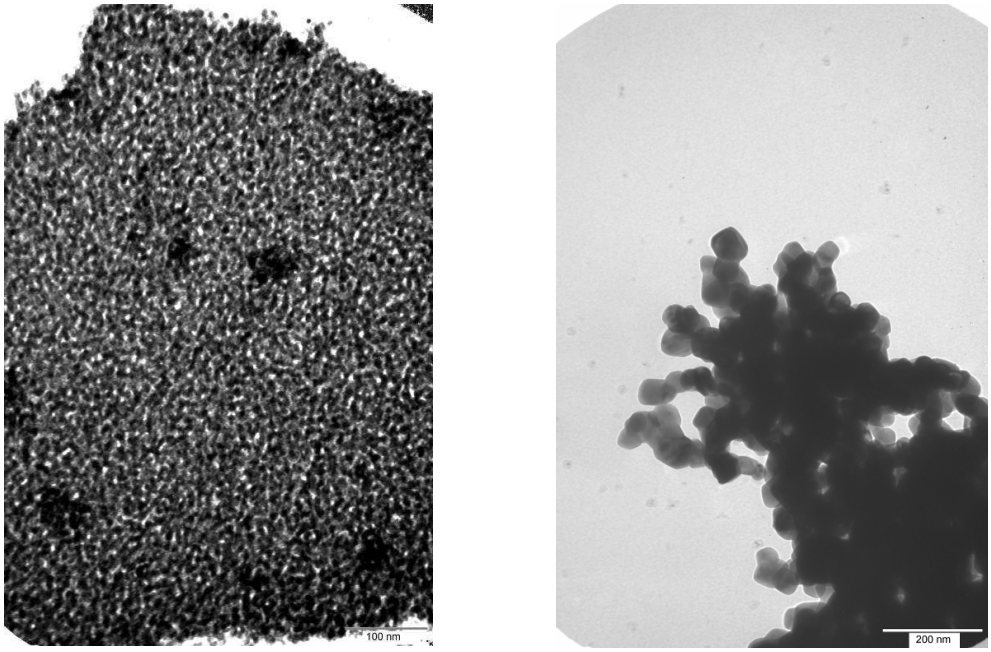

Figure 6. TEM pictures of YSZ obtained at 500 and 1000°C

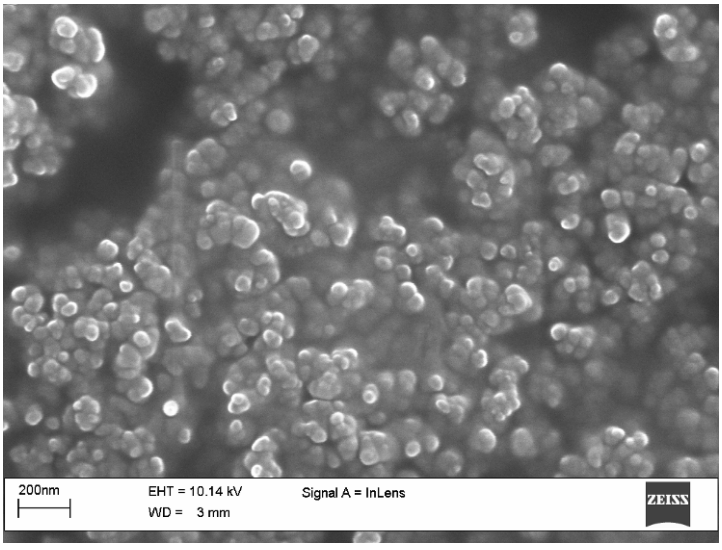

Figure 7. SEM image of the YSZ samples obtained at 1000°C

The XRD analysis gives the measure of the crystallite itself as components of the particle. Thus, the crystallite sizes calculated from the XRD analysis with the Sherrer formula are little less than the particle sizes measured using TEM analysis. The TEM analysis seems to be the most reliable method to determine the particle size because this is directly measured and, in addition, it give information about the shape and the morphology of the powders. The larger particle size determined by the nitrogen adsorption analysis can be affected by errors due to the particle agglomeration especially at high temperatures where the particle adhere to each other.

ACKNOWLEDGMENTS

The authors are grateful to the NFR (Norwegian Research Council), Norway for funding, to the Laboratory for Electron Microscopy, University of Bergen, Norway and to Associate Professor Romulus Tetean and Dr. Eugen Dorolti from Faculty of Physics, Babes–Bolyai University, Cluj–Napoca, Romania for help and useful discussions.

REFERENCES

1. A. A. Ismail, *Applied Catalysis B: Environmental*, **2005**, *58*, 115–12.
2. A. B. Stambouli, E. Traversa, *Renewable and Sustainable Energy Reviews*, **2002**, *6,* 433–455.
3. D. Adityawarman, A. Voigt, P. Veit, K. Sundmacher, *Chemical Engineering Science*, **2005**, *60*, 3373–3381.
4. D. Stover, H. P. Buchkremer, S. Uhlenbruck, *Ceramics International*, **2004**, *30*, 1107–1113.
5. EG&G Services Parsons, Inc., Energy and Environmental Solutions, *Fuel Cell Handbook*, 5th Edition, (Eds: US Dept. of Energy, Office of Fossil Energy) **2000**, 1-1–1-37.
6. F. Tietz, H. P. Buchkremer, D. Stover, *Solid State Ionics*, **2002**, 152-153, 373–381.
7. G. L. Chiarello, I. Rossetti, L. Forni, *Journal of Catalysis*, **2005**, *236*, 251–261.
8. H. Xie, "Nanomaterials for fuel cell applications", **2005**.
9. H. K. Kammler, R. Jossen, P. W. Morrison Jr., S. E. Pratsinis, G. Beaucage, *Powder Technology*, **2003,** *135–136*, 310–320.
10. H. Y. Chang, H. I. Chen, *Journal of Crystal Growth*, **2005**, *283,* 457–468.
11. J. Karthikeyan, C. C. Berndt, J. Tikkanen, S. Reddy, H. Herman, *Materials*
12. L. Combemale, G. Caboche, D. Stuerga, D. Chaumont, *Materials Research Bulletin*, **2005**, *40*, 529–536.

13. M. Gaudon, C. Laberty-Robert, F. Ansart, L. Dessemond, P. Stevens, *Journal of Power Sources*, **2004**, *133*, 214–22.
14. M. Kleitz, F. Petitbon, *Solid State Ionics*, **1996**, *92*, 65–74.
15. M. Lohmann, A. Schmidt-Ott, *Journal of Aerosol Science*, **1995**, *26*, S829–S830.
16. M. C. Williams, "*Fuel Cells*", *7*, **2007**, 78 – 85.
17. R. OHayre, D. M. Barnett, F. B. Prinzc, *Journal of The Electrochemical Society*, **2005**, *152*, A439–A444.
18. R. E. Williford, L. A. Chick, *Surface Science*, **2003**, *547*, 421–437.
19. S. C. Singhal, *MRS Bulletin*, **2000**, *25*, 16–21.
20. S. Lee, T. Son, J. Yun, H. Kwon, G. L. Messing, B. Jun, *Materials Letters*, **2004**
21. S. C. Singhal, "*Solid State Ionics*", **2000**, *135*, 305–313.
22. S. -G. Kim, S. P. Yoon, S. W. Nam, S. -H. Hyun, S. -A. Hong, *Journal of Power Sources*, **2002**, *110*, 222–228.
23. S. P. Jiang, S. H. Chan, *Journal of Materials Science*, *2004*, **39**, 4405–4439.
24. S. P. Yoon, J. Han, S. W. Nam, T. H. Lim, S. A. Hong, *Journal of Power Sources*, **2004**, *136*, 30–36.
25. *Science and Engineering*, **1997**, *A238*, 275–286.
26. T. Chraska, A. H. King, C. C. Berndt, *Materials Science and Engineering*, **2000**, *A286*, 169–178.
26. T. E. Konstantinova, I. A. Danilenko, N. P. Pilipenko, G. K. Volkova, *Electrochemical Society Proceedings*, **2003**, *2003-07*, 153–159.
27. T. Fukui, S. Ohara, M. Naito, K. Nogi, *Journal of Power Sources,* **2002**, *10*, 91–95.
28. V. Esposito, C. DOttavi, S. Ferrari, S. Licoccia, E. Traversa, *Electrochemical Society Proceedings*, **2003**, *2003-07*, 643–652.
29. V. M. Rusu, C. -H. Ng, M. Wilke, B. Tiersch, P. Fratzl, M. G. Peter, *Biomaterials*, **2005**, *26*, 5414–5426.
30. W. Vielstich (Editor), A. Lamm (Editor), H. Gasteiger (Editor), "Handbook of Fuel Cells, Fundamentals, Technology and Applications", *volume 4: Fuel Cell Technology and Applications*, John Wiley & Sons, **2003**.
31. W. J. Stark, M. Maciejewski, L. M¨adler, S. E. Pratsinis, A. Baiker, *Journal of Catalysis*, **2003**, *220*, 35–43.
32. W. N. Wang, I. W. Lenggoro, Y. Terashi, T. O. Kim, K. Okuyama, *Materials Science and Engineering B*, **2005**, *123*, 194–202.
33. W. Z. Zhu, S. C. Deevi, "*Materials Science and Engineering*", **2003**, *A362*, 228–239.

STUDIA UNIVERSITATIS BABEŞ-BOLYAI, CHEMIA, LII, 2, 2007

RHEOLOGICAL BEHAVIOUR OF TITANIA SYSTEMS DURING THE SOL-GEL TRANSITION

ADINA GHIRIŞAN*, VIRGINIA DANCIU*, VERONICA COŞOVEANU* and MIHAELA POPA*

ABSTRACT. Rheological behaviour of titania based systems prepared from the hydrolysis of titanium isopropoxide in ethanol-water mixture with different initial ratios between reagents has been studied. Rheological measurements in this study have established the dependence of gelation time upon the initial composition of raw materials. The achieved results have shown Newtonian behaviour of titania sols before gelation and non-Newtonian (pseudoplastic) behaviour after gelation.

Keywords: rheological behaviour, sol-gel transition, time of gelation, apparent viscosity, Newtonian and non-Newtonian fluids.

INTRODUCTION

Applications of the new low-temperature method for the synthesis of glasses, ceramics, mono-size powders, porous gels, membranes, coatings and thin films known as sol-gel have increased the interest in studying this possible route of preparation [1].

The sol-gel process is based on the hydrolysis of suitable molecular precursors and condensation of oligomers, thus the control of relative reaction rates allow to obtain materials that are more homogeneous than those obtained through conventional high temperature processes. The precursor participates in hydrolysis and condensation reactions forms particles (particulate sol) or polymers (polymeric sol), uniformly distributed in the bulk solvent [1, 2]. The particle-particle and particle-solvent interactions among these units lead to an increase in the viscosity of the solution until a *gel* is formed [3]. The sol-gel evolution has great influence in the porous structure of the final material, usually obtained after the application of a thermal program.

* FACULTY OF CHEMISTRY AND CHEMICAL ENGINEERING, "BABEŞ-BOLYAI" UNIVERSITY CLUJ-NAPOCA, Arany Janos 11, 400028 Cluj-Napoca, Romania

The simplest picture of gelation is that clusters grow by condensation of polymers or aggregations of particles until the clusters collide; then links form between the clusters to produce a giant cluster that is called *gel*. At the moment that the gel forms, many clusters will be present in the sol phase, entangled in but not attached to the spanning cluster. With time, they progressively become connected to the network and the gel will increase. In this process no latent heat is evolved, but the viscosity rises abruptly and elastic response to stress appears [1].

Titanium dioxide (TiO_2) coatings (films) have been studied recently because of a large area of applications: solar cells, photo catalysis, photoelectric properties, antireflective coatings, electronic devices (dielectric mirrors for lasers), ceramic filters, as antibacterial coatings, self-cleaning coatings on car windshields, and protective coatings of marble (for preservation of ancient Greek statues against environmental damage) [4].

Sol-gel method is a relatively wide-spread method of producing TiO_2 coatings. The advantage of this method is the possibility to vary the film properties and low process cost. The sol-gel procedure may have the advantage of obtaining TiO_2 coatings with a smooth or a porous structure, depending on their uses. Controlled synthesis is essential for successful applications, and solution phase methods provide a large degree of control over the synthesis products [5].

The changes in rheological behaviour of materials are usually used to identify the *time of gelation*, t_g, and to establish the type of analysed systems (Newtonian or non-Newtonian fluid) [6, 7].

In this work, the sol-gel evolution of titania based systems using different initial compositions of raw materials has been analysed with a Rheotest 2 (type RV2, produced by Prüfgerate-Werk Medigan, Germany).

From the experimental obtained data, apparent viscosity (η_{app}) was estimated as:

$$\eta_{app} = \frac{\tau}{\gamma} \cdot 100 \text{ (mPa.s)} \quad (1)$$

where: τ is the shear stress (dyn/cm^2), and γ – shear rate (s^{-1}).

$$\tau = z \cdot \alpha \quad (2)$$

z is the constant depending on the type of used cylinder (z = 5.79 dyn/cm^2 for S-S_1 cylinders), and α is the electrical measurement read on Rheotest apparatus.

The analysis of the rheological behaviour of sol-gels TiO_2 performed in this study involves two types of correlations, the first one the modification of apparent viscosity (η_{app}) during sol-gel transition to identify the time of gelation for different initial ratios of the reagents, and the second one the variation of apparent viscosity (η_{app}) with the shear rate (γ) at constant time to establish the type of analysed systems (Newtonian or non-Newtonian material).

To confirme the behaviour of the TiO_2 gels as non-Newtonian material the model of power law (Ostwald de Waele) was used.

EXPERIMENTAL

a. PREPARATION OF MATERIALS

In this work, the synthesis of TiO_2 sol-gels was based on the hydrolysis of titanium isopropoxide ($Ti(O\text{-}iPr)_4$ or IPT). For the synthesis of the TiO_2 sol-gels were used: Ti(V) isopropoxide (>98%, Merck Schuchardt or 97 % Aldrich), anhydrous ethanol (analytical grade, Aldrich), deionised H_2O and HNO_3 (analytical grade, 65%, Primexchim).

The polymerization of formed oligomer in ethanol-water mixture was controlled kinetically with an inhibiting acid (HNO_3) that avoids the precipitation of the oxide or the formation of large heterogeneous zones. In order to obtain a homogenous mixture, it was constantly mixed by means of a magnetic stirrer at room temperature.

The molar ratios of reagents used for the synthesis of TiO_2 sol-gels were: H_2O: IPT = 3.75, EtOH: IPT = 21.4; 26.82 and 33.75, HNO_3: IPT = 0.06; 0.08 and 0.18 [8].

b. EXPERIMENTAL APPARATUS

The rheological behaviour of titania sol-gels have been observed using a Rheotest 2 with 2 cylinders (Type S-S_1), which is based on a simple shearing flow of the sample enclosed in the gap between the 2 coaxial cylinders. From the experimental values obtained at the room temperature 20±1.5 ^{0}C, the apparent viscosity (η_{app}) was estimated on the variation of shear stress (τ) with shear rate ($\gamma = dw_x/dy$). Three replicate runs were carried out for each set of experimental conditions.

RESULTS AND DISCUSSION

The obtained data through rheological measurements, gave us information about the variation of apparent viscosity (η_{app}) during sol-gel transition for different initial rations between reagents (alcohol concentration and acid concentration) and about the variation of apparent viscosity (η_{app}) at different shear rate ($\dot{\gamma}$) and at a fixed time.

Effect of alcohol concentration and acid concentration on the sol-gel evolution of titania based systems has been shown in Figure 1 and 2. Figure 1 plots the evolution of apparent viscosity (η_{app}) of titania sol-gels on the time, corresponding to different EtOH: IPT ratios. Figure 2 plots evolution of apparent viscosity (η_{app}) of titania sol-gels on the time, corresponding to different acid inhibitor concentration.

These kinds of measurements were done at a constant shear rate of 145.8 s^{-1}.

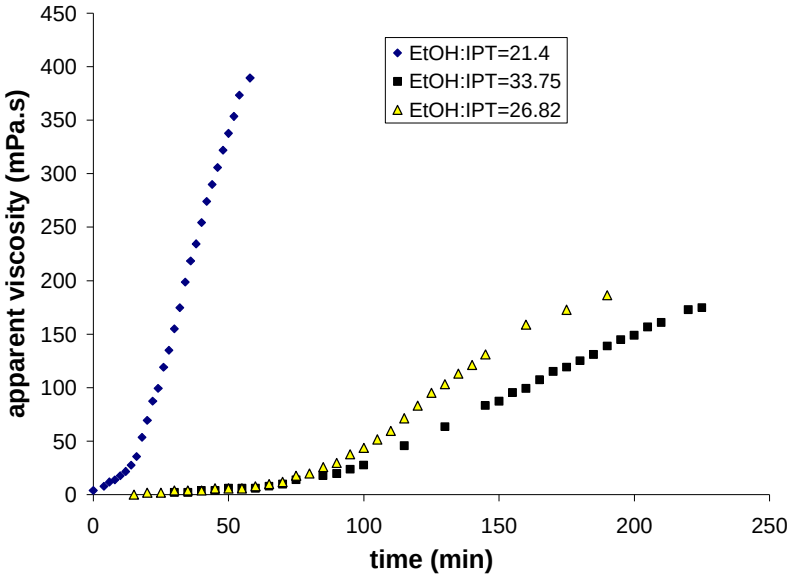

Figure 1. Effect of EtOH: IPT ratio on viscosity change versus time for titania systems during sol-gel transition.

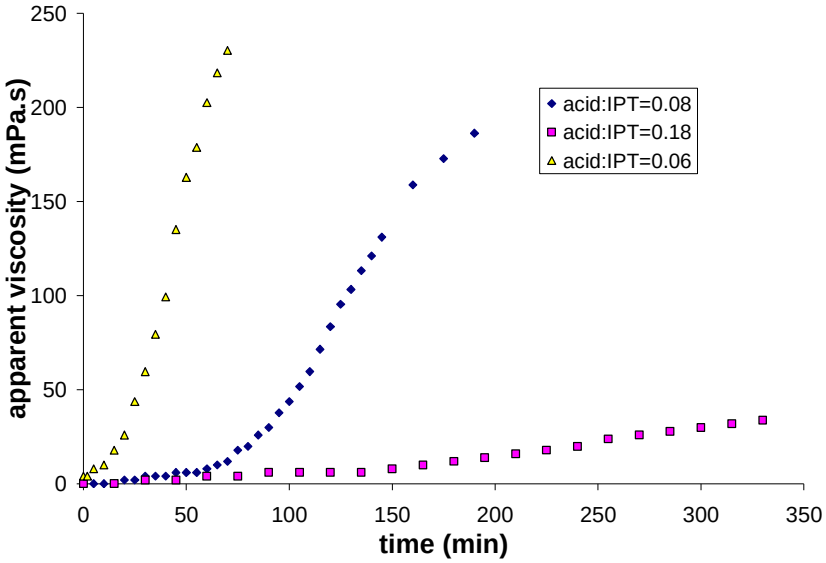

Figure 2. Effect of HNO_3: IPT ratio on viscosity change versus time for titania systems during sol-gel transition.

It is easy to see that the time of gelation for TiO_2 systems is strongly dependent on both ratios EtOH: IPT and HNO_3: IPT employed for preparing the initial solutions. For example, the gelation appears after 20 minutes in the system containing molar ratio EtOH: IPT = 21.4, and after 80 minutes in the system containing EtOH: IPT = 26.82. No substantial difference on gelation time was observed between samples having molar ratios EtOH: IPT = 26.82 and 33.75 (Figure1).

From Figure 2 it can be seen that the apparent viscosity increases quickly at low acid inhibitor concentration and very slowly at a higher concentration of acid inhibitor, a longer time until the gel structure is achieved. For the sample containing a molar ratio HNO_3: IPT = 0.18 no sudden change (increase) was observed during 350 minutes. This means that the increase of the acid inhibitor increase the gelation time, offering longer time for sol-gel transition, and thus a better control on the surface of the films (coatings) when this is necessary (Figure 2).

For the second collection of measurements, necessary to establish the behaviour of titania systems during sol-gel transition the shear rate were varied between 27 s^{-1} and 729 s^{-1}.

The results have shown that the samples used in this kind of experimental measurements (having a molar ratio EtOH: IPT = 26.82, and HNO_3: IPT = 0.08) exhibit a linear and constant, independent on shear rate, shear stress and time, evolution of apparent viscosity (Newtonian behaviour) before gelation (Figure 3), and a non-linear, pseudoplastic, non-Newtonian behaviour after gelation, proper to gel structure, and similar to other synthesised gels [6] (Figure 4).

Figure 4 plots the evolution of the apparent viscosity for two samples collected after 80 minutes that the mixing of reagents was initiated and after 100 minutes.

The analysis of curves plotted in Figure 4 have shown the decrease of apparent viscosity (η_{app}) with increasing of shear rate (γ) in both cases, which confirms non-linear, pseudoplastic or shear-thinning behaviour of titania gels (semisolid materials). This behaviour is characteristic to a specific molecular rearrangement of the system, a de-structuration of the gel, proper to the reduction of the interaction between semisolid particles with the increase of the shear rate. In the same time it is obvious that as the shear rate increases, the slope of graphs decreases.

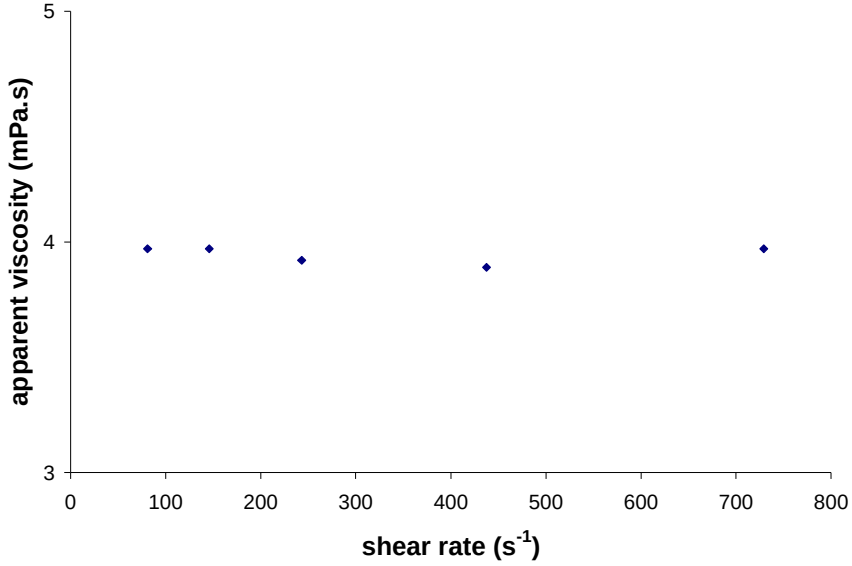

Figure 3. Behaviour of the titania sols before gelation at 30 minutes after the mixing of reagents.

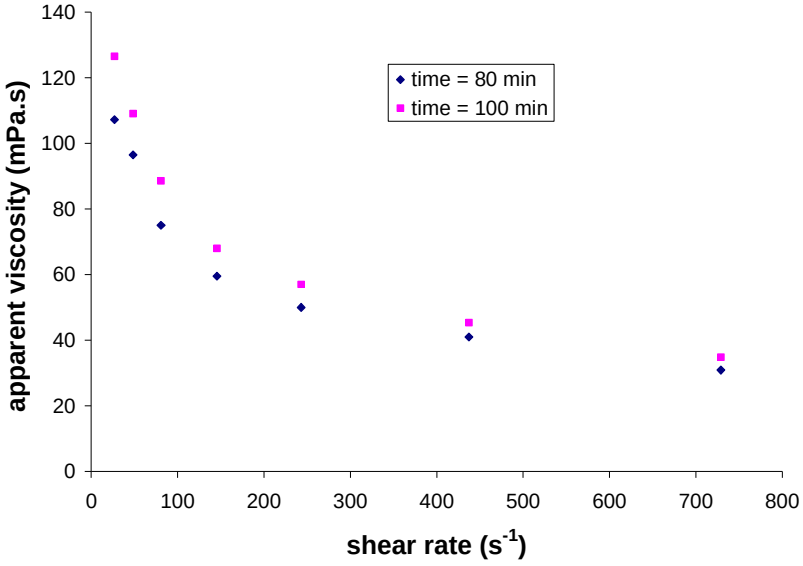

Figure 4. Apparent viscosity change with shear rate registered for the titania gel at 80 and 100 minutes after the mixing of reagents.

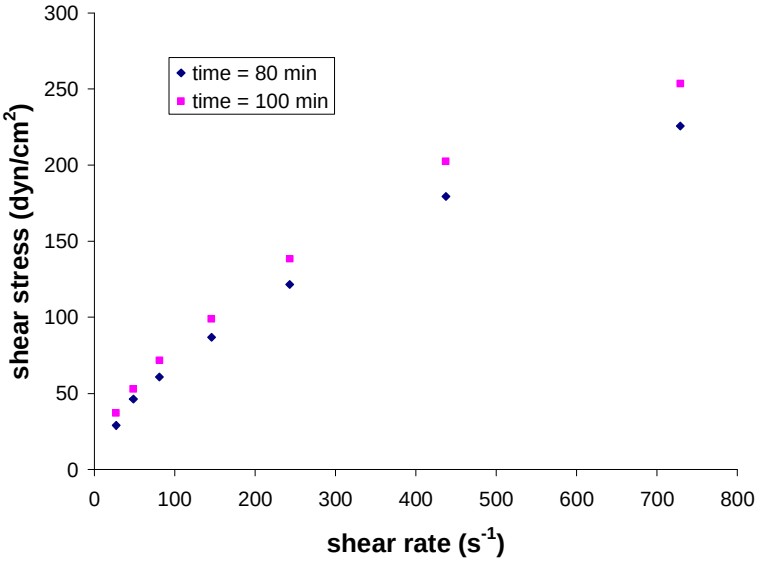

Figure 5. Shear stress (τ) versus shear rate (γ).

The specific plot obtained in Figure 5 confirms the non-Newtonian behaviour of titania systems after gelation, the decrease of the slope of graph with the increase of the shear stress.

Fitting the experimental data obtained for the gel samples to the theoretical power law model Ostwald de Waele, which describes the relationship between shear stress and shear rate (Equation 3), a value of n equal 0.62 was obtained at 80 minutes after mixing of raw solutions and a value of 0.59 at 100 minutes. The values of n index lower than unity confirms the pseudopalstic behaviour of gel samples.

$$\tau = k\gamma^n \tag{3}$$

where k and n are rheological constants of material.

CONCLUSIONS

In this work we have demonstrated that for the titania sol-gels the time of gelation depends on the initial ratio of reagents (EtOH: IPT and HNO_3: IPT). Rheological measurements have shown that the increase of initial concentration of ethanol and acid inhibitor has led to the increase of the time of gelation.

Through rheological measurements, which provide an easy tool for understanding the behaviour of titania based systems during sol-gel transition, the values of apparent viscosity were determined and from special plots the behaviour of the titania sols as Newtonian fluids and gels as non-Newtonian or pseudoplastic fluids was established.

The theoretical power law model Ostwald de Waele, has confirmed the behaviour of TiO_2 system during sol-gel transition.

The influence of other components (e.g., molar ratio H2O: IPT) and of the temperature on the TiO_2 sol-gel transition can be researched in a future work to determine the chemistry and the activation energy involved in this kind of processes.

REFERENCES

1. G. Oskam, *J. Sol-gel Sci. Techn*., **2006**, 37, 161-164

2. J. Brinker and G. Scherrer, "*Sol-Gel Science, the Physics and Chemistry of Sol-Gel Processing*", Academic Press, San Diego, California, **1990**

3. J. Livage, C. Sanchez and F. Babonneau, "*Chemistry of Advanced Materials: An Overview*", Wiley-VCH, Inc., L.V. Interrante and M. J. Hampden-Smith Eds., **1998**

4. J. Livage, F. Beteille and C. Roux , *Acta Mater*, **1998,** 46, 743-752

5. M. Fernandez-Torres, A. Ghirişan and J.M. Ţipan-Lepetich, *Can. J. Ch. Eng*., **2001**, 79, 454-457

6. N. Teodorescu, „*Reologie aplicată*", Ed. Matrix Romania, Bucureşti, **2004**

7. U. Diebold " The Surface Science of Titanium Dioxide", Tulane University Press, New Orleans, **2003**

8. V. Danciu, M. Popa, Z. Pap, L. Baia, M. Baia, V. Coşoveanu, F. Vasiliu, L. Diamandescu and R. Alexandrescu, „Iron Doped and Undoped TiO_2 Catalysts for Advanced Water Treatment", First European Conference on Environmental Applications of Advanced Oxidation, 7-9 September, Greece, **2006**

STUDIA UNIVERSITATIS BABEŞ-BOLYAI, CHEMIA, LII, 2, 2007

MODELING AND SIMULATION OF POLLUTANT DUST WAVE FROM A FOUNDRY

MIHAELA MORAR*, A. IMRE-LUCACI*

ABSTRACT. In this paper a model was developed for pollutant dust wave dispersion from a foundry. The chemical composition of the foundry dust is 88.02 % SiO_2, 4.62 % Fe, 7.36 % others (Al, Cu, Pb, Ca, Cr, Zn etc.). The Gaussian Dispersion Model – local model dispersion for point shape sources with continuous or accidentally emission was used. The dispersion of a pollutant dust wave in the environment is influenced mainly by the wind velocity, atmospheric stability class and sources characteristics. Matlab was used to create this simple model and together with the simulation program that provides information about the dispersion area of the pollutant dust wave. The model can be used and help in promptly acting to prevent or to solve the pollutant accidents.

INTRODUCTION

The pollution is a phenomenon that cannot take in account the countries physical borders (ex. acid rains, polluted rivers) and for this, we all are responsible and we have to try to prevent pollution.

Economical-industry evolution of our country in the last decades made serious environment pollution problems. Therefore, researchers are trying to develop the most efficient methods to catch and purify the residual gases before their evacuation in the atmosphere and also, to redesign the equipments or entire technology.

The basics for mathematical modeling of pollutant dispersion are represented by three important equations that describe mass balance, energy balance and momentum balance. This kind of equations must be written for each pollutant.

Generally, for one receiver, it could be made an estimation of one source substance concentration by using the dispersion equation. For the models accepted by EPA (European Pollution Administration) the necessary

* Babes-Bolyai University, Faculty of Chemistry and Chemical Engineering, Cluj-Napoca, Romania

data about the emission that took place are: source coordinates, internal diameter of the chimney top side, exit velocity of emission and temperature on the top of the chimney. Also, it's necessary to know hourly meteorological parameters (stability class of the atmosphere, wind direction, wind velocity, air temperature, etc.). The results of this kind of models are the hourly concentrations that are evacuated by each pollutant source [4].

The model in this research was made for a pollutant dust wave from a foundry. The chemical composition of the foundry dust is 88.02 % SiO_2, 4.62 % Fe, 7.36 % others (Al, Cu, Pb, Ca, Cr, Zn etc.). Because of the presence of the SiO_2 in dust, the most of the employees have a disease called silicosis.

DISPERSION MODEL'S DESCRIPTION

For this research was used the Gaussian Dispersion Model – local model dispersion for isolated sources with continuous or accidentally emission [3]. The Gaussian dispersion model is used especially to obtain static parameters of concentrations (average values, passing frequencies of sanitary limits, etc.). To estimate the concentration value, the distribution frequencies of meteorological parameters obtained by measurements is used. Dispersion coefficients used in this model were experimentally developed for long distances between 10 km and 30 km and the Gaussian model provides reliable predictions for this distances. For distances between 20 km and 100 km the model can be used only to obtain qualitative information about pollutants concentration [3].

Gaussian model uses the following equations to evaluate pollutant concentration:

a. if the mixing height (h_s) is infinite, there is no thermal inversion or weather is stable, is used Gaussian solution for a point shape source with continuous release:

$$\overline{C}(x,y,z) = \frac{Q}{2\pi\sigma_y\sigma_z\overline{u}}\exp\left(-\frac{y^2}{\sigma_y^2}\right)\cdot g(z,H) \tag{1}$$

$$g(z,H) = \exp\left[-\frac{1}{2}\left(\frac{(z-H)^2}{\sigma_z^2}\right)\right] + \exp\left[-\frac{1}{2}\left(\frac{(z+H)^2}{\sigma_z^2}\right)\right] \tag{2}$$

b. if the value of dispersion parameter is $\sigma_z > 1{,}6h_s$ and the weather is instable or neutral:

$$\overline{C}(x,y,z)=\frac{Q}{\sqrt{2\pi}\sigma_y h_s}\exp\left(-\frac{y^2}{2\sigma_y{}^2}\right) \quad (3)$$

In this situation the pollutant is mixed uniformly in boundary layer and the concentration doesn't depend on hight z.

c. if the weather is instable or neutral and the dispersion parameter value is $\sigma_z < 1{,}6h_s$:

$$\overline{C}(x,y,z)=\frac{Q}{2\pi\sigma_y\sigma_z\overline{u}}\exp\left(-\frac{y^2}{2\sigma_y{}^2}\right)\cdot g(h_s) \quad (4)$$

$$g(h_s)=\sum_{k=-4}^{k=+4}\left\{\exp\left[-\frac{1}{2}\left(\frac{(z-H+2kh_s)^2}{\sigma_z{}^2}\right)\right]+\exp\left[-\frac{1}{2}\left(\frac{(z+H+2kh_s)^2}{\sigma_z{}^2}\right)\right]\right\} \quad (5)$$

In case of thermal inversions, the pollutants can't be dispersed vertically because the inversion surface behaves like a mirror surface.

The values for meteorological parameters for each stability class are presented in [3].

RESULTS AND DISCUSSION

Dispersion of a pollutant dust wave in the environment is influenced mainly by the wind velocity, atmospheric stability class and sources characteristics. The maximal admissible value of the dust in atmosphere is 0.5 □g/m^3.

Pollutant concentration in atmosphere is kept high for a long area if wind velocities are low and the maximal admitted concentration is over passed for a distance of 5000-6000 m (Fig. 1).

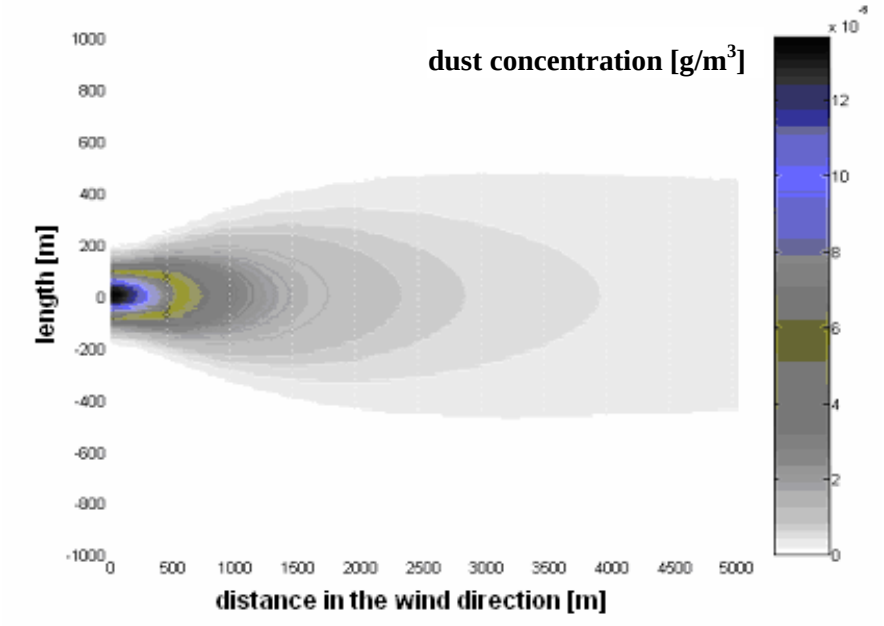

Fig. 1. Pollutant dust wave dispersion area in case of atmospherically calm conditions at z=20 m

If the wind velocity grows, the pollutant spread distance, with concentrations higher than 0.5 μg/m^3, decreases from 5000-6000 m to 1000-1500 m because of the faster spread of the pollutant particles in the atmosphere. If the wind velocity is higher than the evacuation velocity of the air mixed with dust, appears a phenomenon called downwash (flowing of the pollutant downward the chimney out-wall, Fig. 2).

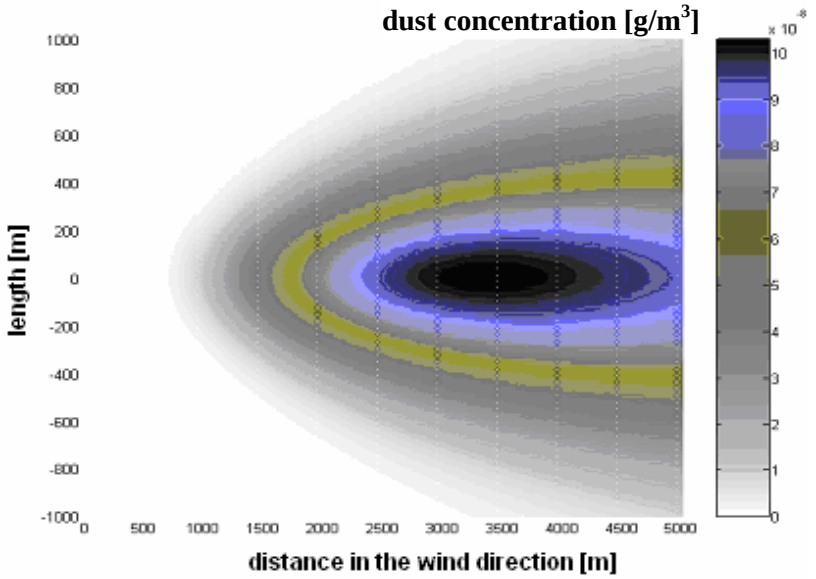

Fig. 2. Downwash effect (footprint of the dust concentration at z=20 m).

In the foundry, there are 5 pollutant sources (5 cyclone dust separators that don't work properly or don't work at all) that are different by the exit flow and the diameter of the evacuation chimney (Table.1).

Table 1.

Sources inventory [6]

Source No.	Chimney diameter [m]	Exit flow [m³/h]	Dust quantity in exit flow [g/h]
1	0.4	30000	2100
2	0.6	24000	1560
3	0.35	16000	768
4	0.9	28000	1820
5	0.25	2000	140

When all 5 sources work simultaneously, the dust concentration evacuated in atmosphere is the highest and the dispersion area becomes larger (Fig. 3). The pollutant dust wave becomes more dangerous for the environment and for the people. In this conditions dust concentration in the atmosphere is about $2 \cdot 10^{-5}$ g/m³.

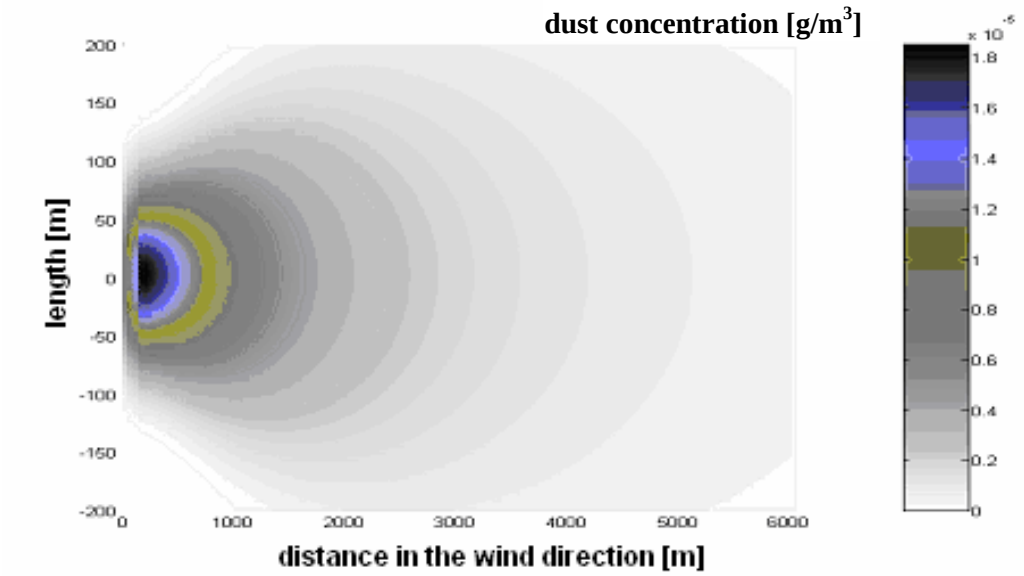

Fig. 3. Pollutant dust wave from all five sources in the wind direction (footprint of the dust concentration at z=20 m)

If the cyclone dust separators are replaced with bag filters (94 % efficiency), pollutant dust concentrations are reduced under the maximal limit of 0.5 μg/m^3 (Fig. 4). For the conditions of source no. 1 (30000 m^3/h evacuated air, 1200 g/h dust) the filter evacuates in atmosphere only 126 g/h dust in 30000 m^3/h air.

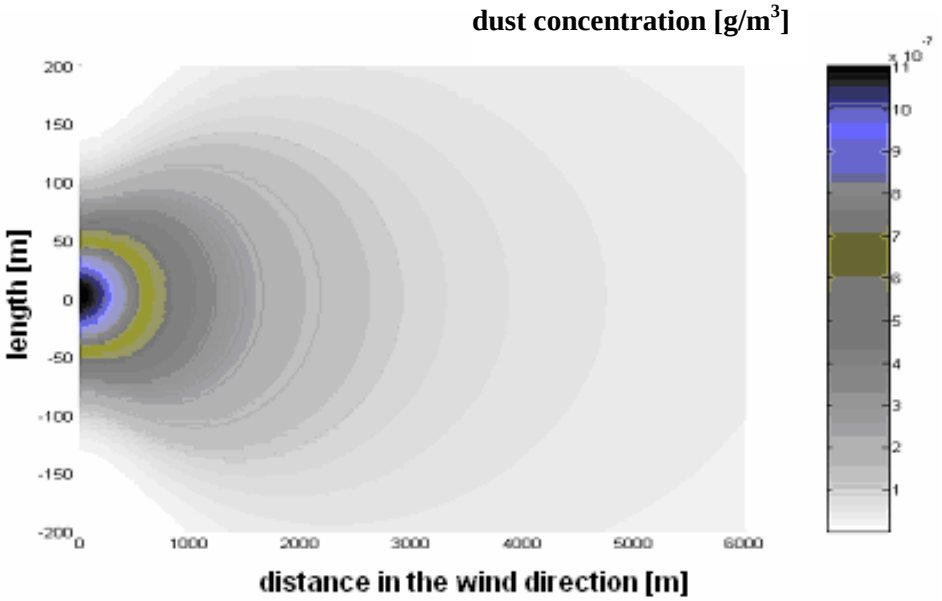

Fig. 4. Pollutant dust area for a filter bag in the condition of source 1 (footprint of the dust concentration at z=20 m)

CONCLUSIONS

Gaussian model used for modeling and simulation of the pollutant dust dispersion in the environment is only a simplified model that helps to estimate the values of dust concentration evacuated in atmosphere (prediction and post evaluation). The simulations can help to estimate accidental emissions and, if the pollution already occurred, provides the opportunity to know how far the dust extends and how large is the area that the environmental agents have to clean or to evacuate.

Matlab was used to create this simple model and to simulate the process that gives information about the dispersion area of the pollutant dust wave. This software can be easily used and help to promptly act to prevent or to solve the pollutant accidents. It can be easily used for other substances because the Gaussian model needs only the released mass of the pollutant in atmosphere and it's not necessary to know the chemical and physical characteristics of the pollutant substances.

The pollution becomes more serious when the pollutant wave contains toxic or lethal substances that affect not only the vegetation and animals but also the people.

List of symbols

x – down-wind horizontal coordinate, m

y – cross-wind horizontal coordinate, m

z – vertical coordinate, m

$\overline{C}(x, y, z)$ *- concentration as a function of the terms between the brackets, g/m*^{3}

Q – released mass, g

σ_y, σ_z *– cross-wind and vertical dispersion parameters of cloud, m*

u – down-wind velocity of dispersing material, m/s

H – height of cloud centre-line, m

h_s *– mixing height, m*

REFFERENCES

1. C. Savii, G. Savii, Modelarea si simularea poluarii atmosferice, Ed. Presa universitara romana, Timisoara, **2000**.

2. E. A. Bakkum, N. J. Duijm, "Vapour cloud dispersion", Methods for the calculation of physical effects – Yellow Book, Chapter 4, Hague, **1997.**

3. I. Sandu, I. V. Pescaru, I. Sandu, Modele de evaluare a dispersiei poluantilor in atmosfera, Ed. SITECH, Craiova, **2004.**

4. M. Morar, Modeling and simulation of pollutant dust wave from a foundry, Diploma Thesis, Babes-Bolyai University, Cluj-Napoca, **2005**.

5. S. C. Ecoproiect, Bilant de mediu de nivel I, Cluj-Napoca, **2005**.

6. S. Coldea, Difuzia si dispersia poluantilor in geofluide, Ed. Presa universitara clujeana, Cluj-Napoca, **2002**.

7. V. Voicu, Combaterea noxelor in industrie, Ed. Tehnica, Bucuresti, **2002.**

STUDIA UNIVERSITATIS BABEŞ-BOLYAI, CHEMIA, LII, 2, 2007

SIMULATION OF AN INDUSTRIAL COMPLEX FCCU PART I: BUILIDING THE MODEL AND VALIDATION

RALUCA ROMAN*, ZOLTAN KALMAN NAGY, VASILE MIRCEA CRISTEA*, ŞERBAN PAUL AGACHI***

ABSTRACT. The Fluid Catalytic Cracking process is a proven state-of-the-art technology for the conversion of gasoils and resids to lighter, higher-value products. A mathematical model for this process has been developed. The model describes not only the most phases of chemical engineering fundamentals, such as fluidization, heat/mass transfer, and distillation, but also incorporates the process kinetics, based on a lumping strategy which lumps molecules and reactions according by their boiling point and treated as pseudo-components. Based on the experimental data it was analyzed the process variables behavior in the presence of disturbances.

1. INTRODUCTION

A petroleum modern refinery is composed of processing units that convert crude oil into usable products such as gasoline, diesel, jet fuel, heating oil, fuel oil, propane, butane, and chemical feedstocks that are very useful in producing other products such as plastics, synthetic rubbers and fabrics and also cosmetics. Fluid Catalytic Cracking Unit (FCCU) is one of the most important conversion processes in a petroleum refinery. The main propose of this unit is to convert high-boiling petroleum fractions (gasoil) to high value, high octane gasoline, high cetane diesel and heating oil [1]. The three dominant reactions are cracking, isomerization, and hydrogen transfer. The catalyst acid sites have a major influence on the reaction chemistry. The introduction of zeolites into the FCC catalyst drastically improved the performance of the catalytic cracker reaction products. The zeolite catalysts are active and selective. The higher activity and selectivity translate to more profitable liquid product yields and additional cracking capacity [2].

* Babeş-Bolyai University, Faculty of Chemistry and Chemical Engineering, 11 Arany Janos. 400028 Cluj-Napoca, Romania, e-mail: romanr@chem.ubbcluj.ro

** Loughborough University, Department of Chemical Engineering, Loughborough, LE11 3TU, United Kingdom

The process consist in the following: raw material is mixed with the regenerated catalyst in reactor riser. Here took place the cracking reactions and coke formation. The products (gasoline, disesel, slurry) are separated in fractionator and the catalyst poisoned with coke is regenerated in regenerator (Figure1).

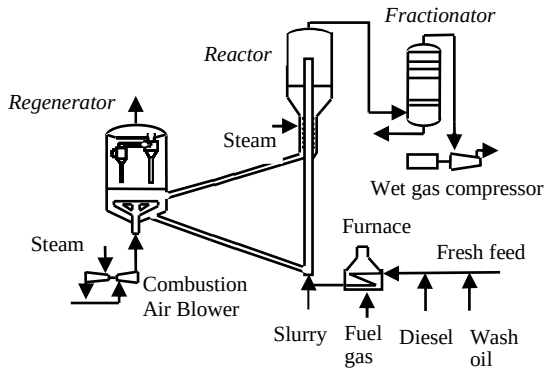

Figure 1. Fluid Catalytic Cracking Unit

2. PROCESS MATHEMATICAL MODELING

Mathematical modeling in the chemical engineering field has multidisciplinary character, dealing with different processes which must be described. A mathematical model is a system of equations that defines the intrinsic interdependencies of a system. Analytical mathematical models are based on conservation equations (mass, energy, momentum), laws of the physical and chemical processes that are taking place in the system and are able to describe proper the process [3].

Numerous studies are concerned with the modeling of this unit, which are very useful in elucidating of the main characteristics of this unit The FCCU dynamic model has been developed on the basis of reference construction and operation data from an industrial unit and consists of detailed models of: the feed and preheat system, reactor stripper, riser, regenerator, air blower, wet gas compressor, catalyst circulation lines and main fractionator. The FCCU model has been developed on the basis of reference construction and operation data from an industrial unit: ROMPETROL Refinery, Romania. The

resulted global model of the FCCU is described by a complex system of partial-differential-equations, which was solved by discretizing the kinetic models in the riser and regenerator on a fixed grid along the height of the units, using finite differences. The resulted model is a very high order DAE, with 933 ODEs (133 from material and energy balances and 800 resulted from the discretization of the kinetic models). The model captures the major dynamic effects that can occur in an actual FCCU system. It is multivariable, strongly interacting and highly nonlinear.

A model to predict the yields of valuable products is included: the five lump kinetic model for the riser reactor, which can describe the composition of the major product:gasoline and the raw material conversion [4,5]. The following assumptions have been made: approximately 10% of the HCO was uncrackable; effectively no gasoline overcracking takes place; diesel only cracks to gas and is not converted into gasoline. The kinetic model is schematically presented in Figure 2.

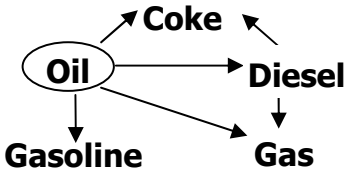

Figure 2. Five lump model for the catalytic cracking

This model is described by the following set of differential equations:

$$\frac{\partial y_{slurry}}{\partial t} = ((-(k_1 + k_2 + k_3)(y_{slurry} - x_{slurry}))\psi_{conv} - (k_5(y_{slurry} - x_{slurry})CTO \quad (1)$$

$$\frac{\partial y_{diesel}}{\partial t} = ((k_1(y_{slurry} - x_{slurry}) - k_4 y_{diesel})\psi_{conv} - (k_6 y_{diesel})\psi_{coke})CTO \quad (2)$$

$$\frac{\partial y_{gasoline}}{\partial t} = ((k_2(y_{slurry} - x_{slurry}))\psi_{conv} CTO \quad (3)$$

$$\frac{\partial y_{gas}}{\partial t} = ((k_3(y_{slurry} - x_{slurry}) + k_4 y_{diesel})\psi_{conv} CTO \quad (4)$$

$$\frac{\partial y_{coke}}{\partial t} = ((k_5(y_{slurry} - x_{slurry}) + k_6 y_{diesel})\psi_{coke} CTO \quad (5)$$

The activity function of coke formation is described by the following equation:

$$\frac{\partial \psi_{coke}}{\partial t} = -\alpha \psi_{coke} \quad (6)$$

The activity function of conversion is assumed to be the same for all the reactions:

$$\frac{\partial \psi_{conv}}{\partial c_c} = -k_d \psi_{conv} \tag{7}$$

3. MODELING RESULTS

The five lump kinetic model for the riser section leads to a set of partial differential equation who can give a good prediction of the cracabiliy of the aromatic gas oil. For the riser section, described by the five-lump kinetic model, a sensitivity analysis at different catalyst-raw material-ratio (which is an important disturbance in a real process) for the raw material conversion has been made and it was observed that the CTO has a small influence on the raw-material conversion; the increase of the CTO leads to an approximate the same value of conversion (~ 80%), as Figure 3 shows:

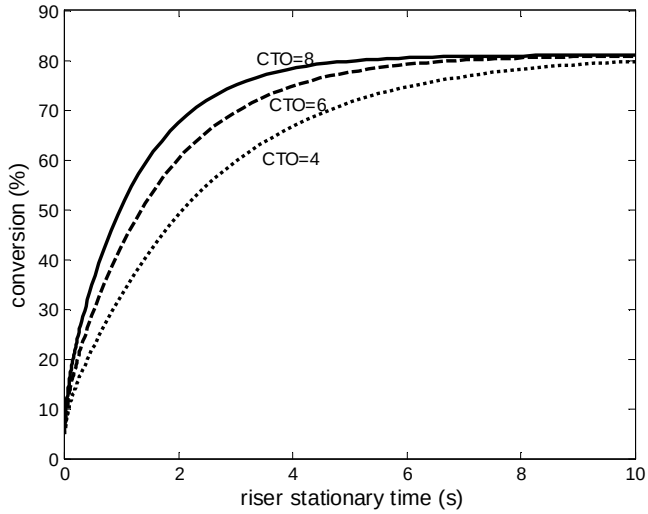

Figure 3. Raw-material conversion at different catalyst-raw material-ratio (CTO)

Comparison between modeling results and industrial operating data form ROMPETROL Refinery has been performed for sets of data, confirming the main trends of the dynamic process behavior. Simulated variables are situated in a range corresponding to industrial unit behavior as can be shown in Table 1, Figure 4 and Figure 5.

Table 1

Typical operating conditions and values obtained with the simulator

Process variable	Measure unit	Data Plant		Value in simulator
		Minimum value	Maximum value	
Catalyst-to-Oil Ratio	-	6.5	8.5	7.4
Reactor pressure	bar	1.5	2.2	1.51
Regenerator pressure	bar	1.7	2.4	1.7
Main fractionator pressure	bar	0.9	1.5	1.3
Regenerator temperature	^{0}C	682	735	709.6
Reactor temperature	^{0}C	505	535	524.5
Raw material temperature	^{0}C	190	320	303.5
CO_2 concentration in flue gas	%	16	19	16.07
O_2 concentration in flue gas	%	0.8	2.5	1.02
Reactor Catalyst Inventory	tons	35	50	39.7
Total Catalyst Inventory	tons	175	195	191

Next figures present the open-loop dynamic simulation results together with the industrial data form ROMPETROL Refinery. It is presented the the reactor and regenerator pressure behavior when the raw material flow disturbance appears. For the first set of experiments the fresh feed flow decreases with 5.5 m^3/h at t=80 min. The simulation results are presented comparatively with the experimental data from the plant in Figure 4. In the second set of experiments, fresh feed flow decrease with 1.2 m^3/h at t=10 min then it decrease with another 13.8 m^3/h at t=70 min. The simulation results are presented comparatively with the experimental data from the industrial plant in Figure 5.

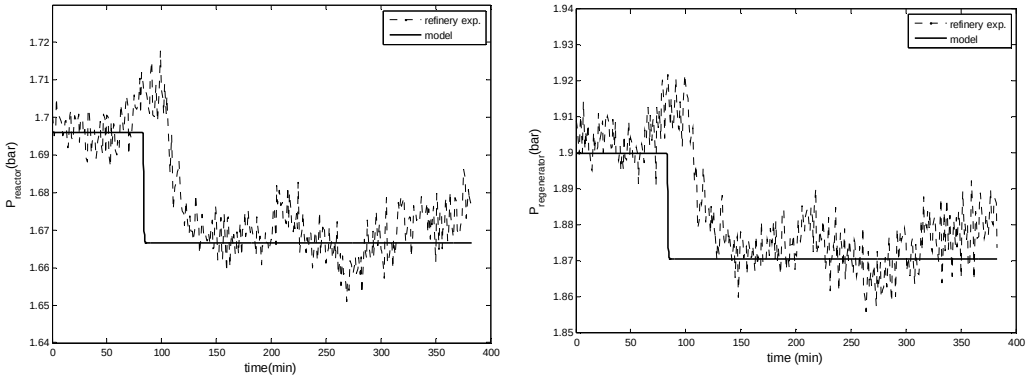

Figure 4. Open-loop simulation of FCCU dynamic behavior- comparison with industrial data (first set of experiments)

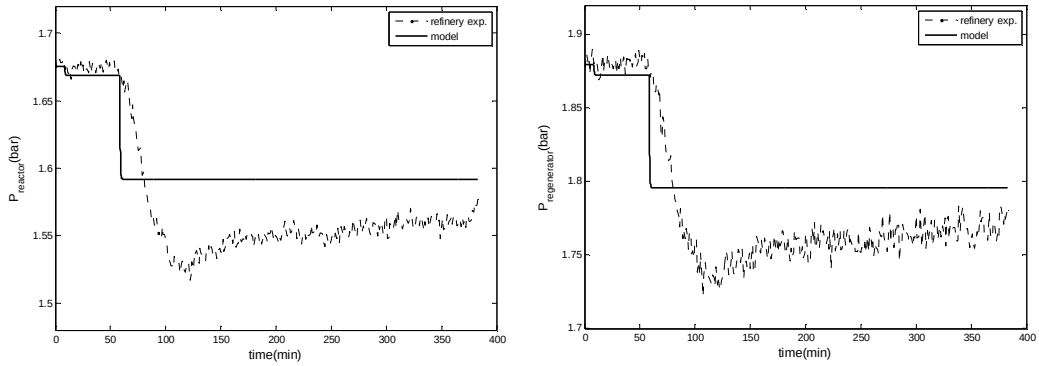

Figure 5. Open-loop simulation of FCCU dynamic behavior- comparison with industrial data (second set of experiments)

4. CONCLUSIONS

A five lump kinetic model (namely: gas-oil, gasoline, diesel, gases and coke) capable to predict raw material conversion was introduced in the FCC process global model. Based on the experimental data, comparisons between the output values in simulator and industrial data, in the presence of disturbances where made. Results obtained by the simulations present a good fit with industrial operating data. With this new model, the FCCU complex behavior in the presence of disturbances can be studied in order to improve the productivity and profitability of the modern process.

ANNEX

k_I = reaction rate constant (gfeed · gcat · s^{-1})
kd = deactivation constant for conversion (wt%)
α = deactivation constant for coke formation (s^{-1})
α = deactivation constant for coke formation (s^{-1})
c_c = coke content on catalyst (wt %)
CTO = catalyst-to-oil ratio (gcat/gfeed)
ϕ_{coke} = activity function for coke formation
ϕ_{conv} = activity function for conversion
ϕ_{coke} = activity function for coke formation
ϕ_{conv} =activity function for conversion

ACKNOWLEDGEMENTS

The authors are also gratefully to the ROMPETROL Company for their support.

REFERENCES

1. J. Ancheyta-Juarez, R. Sotelo-Boyas, *Energy and Fuels*, **2000**, *14*, 1226-1231.
2. M. V. Cristea, S.P. Agachi, V. Marinoiu, *Chemical Engineering and Processing*, **2003**, *42*, 67-91.
3. R. Sadeghbeigi, "Fluid Catalytic Cracking Handbook", Buterworth-Heinemann, New York, **2000**
4. V. Tasoti, 'Enhancement of environmental security by mathematical modelling and simulations of processes', *NATO Security through Science Series*, **2007**, 47-56
5. X. Dupain, E. D. Gamas, R. Madon, C.P. Kelkar, M. Makkee, J.A. Moulijin, *Fuel*, **2003**,*82*, 1559-1668.

STUDIA UNIVERSITATIS BABEŞ-BOLYAI, CHEMIA, LII, 2, 2007

SIMULATION OF AN INDUSTRIAL COMPLEX FCCU PART II: STUDY OF THE PROCESS DYNAMIC BEHAVIOR

RALUCA ROMAN*, ZOLTAN KALMAN NAGY, VASILE MIRCEA CRISTEA*, ŞERBAN PAUL AGACHI***

ABSTRACT. The fluid catalytic cracking unit (FCCU) is an important processing unit in an oil refinery. A mathematical model for this process has been developed. The novelty of the model consists on the complex global dynamics of the reactor-regenerator-fractionator system as well as complex catalytic cracking kinetics for the reactor. The mathematical model consist of the main subsystems of an industrial unit: feed and preheat system, reactor (riser and stripper), regenerator, air blower, wet gas compressor, catalyst circulation lines and the main fractionator. Based on the mathematical model it was analyzed the dynamic behavior of this complex process that includes also the economical aspects of the process.

1. INTRODUCTION

The Fluid Catalytic Cracking Unit (FCCU) is one of the most important process units in oil refineries for the largest yield of products reached and the importance of them. A small benefit in this process is economically attractive. The (FCC) unit converts gas oils into a range of hydrocarbon products of which gasoline and diesel are the most valuable. The amount of low market-value feedstocks available for catalytic cracking is considerable in any refinery. The ability of a typical FCC unit to produce gasoline and diesel from low market value feedstocks gives the FCC unit a major role in the overall economic performance of the refinery. An overview of the FCC process is given in Figure 1.

* Babeş-Bolyai University, Faculty of Chemistry and Chemical Engineering, 11 Arany Janos, 400028 Cluj-Napoca, Romania, e-mail: romanr@chem.ubbcluj.ro

** Loughborough University, Department of Chemical Engineering, Loughborough, LE11 3TU, United Kingdom

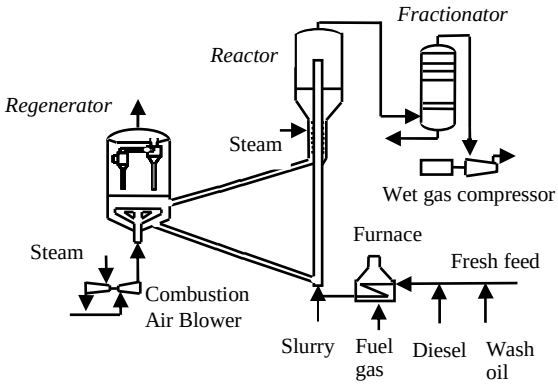

Figure 1. Fluid Catalytic Cracking Unit

The unit consists of a reactor-regenerator section, main fractionator and gas processing facilities. The feed is heated in a fired heater (furnace) and combined with regenerated catalyst in the bottom of the reactor (riser). The catalyst and the reacted hydrocarbon vapors flow up the riser and are separated in the reactor cyclone. The catalyst circulation is achieved by burning off the coke deposit in a fluidized bed inside the regenerator. A steam turbine driven air blower supplies the oxygen needed to burn the coke deposit. The spent catalyst is held up in a small fluidized bed in the upper part of the reactor (stripping section) before being returned to the regenerator. The air flow for combustion was is provided by the combustion air blower. Catalyst in the regenerator is fluidized; carbon and hydrogen on the catalyst react with oxygen to produce CO, CO_2, H_2O. Gas travels up in the regenerator into the cyclones where the entrained catalyst is removed and returned into bed. The flue gas from the regenerator is sent to a waste heat boiler before being discharged to the atmosphere. The FCC unit is operated in full burn mode. Vapor products from the reactor (gases, gasoline, diesel, slurry) are sent to the main fractionator where various boiling point fractions are withdrawn [1].

Numerous studies are concerned with the modeling of this unit, which are very useful in elucidating of the main characteristics of this unit dealing with strong interactions and many constraints from the operating, security and environmental point of view. For the reactor riser, many kinetic models have been proposed. They can be divided in two categories:

heavy lumped models and molecular based models. The later is more generic, but is only applicable with analysis at the molecular scale. Because of this complex analysis, the different groups of molecules are lumped by their boiling point and treated as pseudo-components for a global description of the phenomena taking place in reactor [2].

The potential of yielding more market-oriented oil products, increasing production rate and stabilizing the operation become the major incentives to search for more accurate and practical models and high performance, cost effective and flexible control strategies.

2. MATHEMATICAL MODEL OF THE FCCU

The FCCU complex behavior in the presence of disturbances has been done using the mathematical model of the process. To obtain a mathematical model of the FCC process it was necessary to write mass, energy, moment and conservation equations; equation to describe physical and chemical processes that are taking place in the system and it was obtained, by this way, an analytic mathematical model [3]. It was also studied and identified the equations that correlate the input and output variables by using statistical techniques and it was obtained a new dynamic mathematical model for the FCCU that incorporates process hydrodynamics, heat transfer, mass transfer and catalytic cracking kinetics [4].

The model has been developed on the basis of reference construction and operation data from an industrial unit: ROMPETROL Refinery, Romania. The new FCCU mathematical model includes the main systems: feed and preheat system, reactor (riser and stripper), regenerator, air blower, wet gas compressor catalyst circulation lines and the main fractionator. The novelty of the model consists in that besides the complex dynamics of the reactor-regenerator system it also includes the dynamic model of the fractionator and in this way it can be possible to study the to study its dynamic effects on the overall system. The global model also includes a five lump kinetic model (namely: gas-oil, gasoline, diesel, gases and coke) capable to predict the yields of valuable products and gasoline octane value [5].

The resulted global model of the FCCU is described by a complex system of partial-differential-equations, which was solved by discretizing the kinetic models in the riser and regenerator on a fixed grid along the height of the units, using finite differences. The resulted model is a very high order differential-algebraic equations system (DAE), consists of 933 differential algebraic equatios (ODEs): 133 equations derived from material

and energy balances and 800 resulted from the discretization of the kinetic model and with more than 100 algebraic equations. The plant simulator was implemented in C++ programming language for efficient solution and it was compiled in Matlab/Simulink programming language because it has a friendly user graphic interface. The model captures the major dynamic effects that can occur in an actual FCCU system. It is multivariable, strongly interacting and highly nonlinear.

3. SIMULATION RESULTS

The new developed simulator gives useful information regarding the dynamic behavior of the global reactor-regenerator-fractionator system and predicts the composition of the main products (gasoline and diesel) in the case of different disturbances that can appear during the process. Different sets of disturbances have been studied and the evolutions of the most representative process variables in the presence of the slurry recycle flow rate changes in the Figure 2.

The **slurry recycle flow rate** disturbance could appear due to the raw-material fresh feed rate change or due to the changes in the valve position on the slurry circulation line. A decrease by 30% in the slurry recycle rate determine the increase of the regenerated catalyst flow which increase the catalyst-to-oil ratio and this leads to a fast increase of coke in the riser *($coke_{riser}$)*. This coke amount in regenerator decreases the regenerator temperature *(T_{reg})* by 1.5 ^{0}C, and also the reactor temperature *(T_r)* by 0.8 ^{0}C. The increase of the reactor temperature leads to an intensification of the cracking reactions, with the effect of the reactor pressure *(P_r)*. The small increase of the reactor pressure influences the spent catalyst flowrate *(F_{sc})* (0.6% increase). The flowrate of regenerated catalyst (F_{rgc}) increases by 0.3% and for this reasons, reactor catalyst inventory *(Wr)* increases by 2 tons and in the regenerator catalyst inventory *(W_{reg})* increases by 0.07 tons. Because the spent and regenerated catalyst increase and the coke production in riser also increases, the carbon production in regenerator increases and the combustion in the regenerator is performed in an excess of oxygen; the O_2 amount *(X_{O2})* increase with 20% and the CO_2 amount (X_{CO2}) increases with 9.8%. This disturbance influence catalyst-to-oil ratio and also the products profile in main fractionator, gasoline composition on the top of the column decrease by 1.2 % and on top it increases by 0.05% which could have an a significant economical impact on the plant profit.

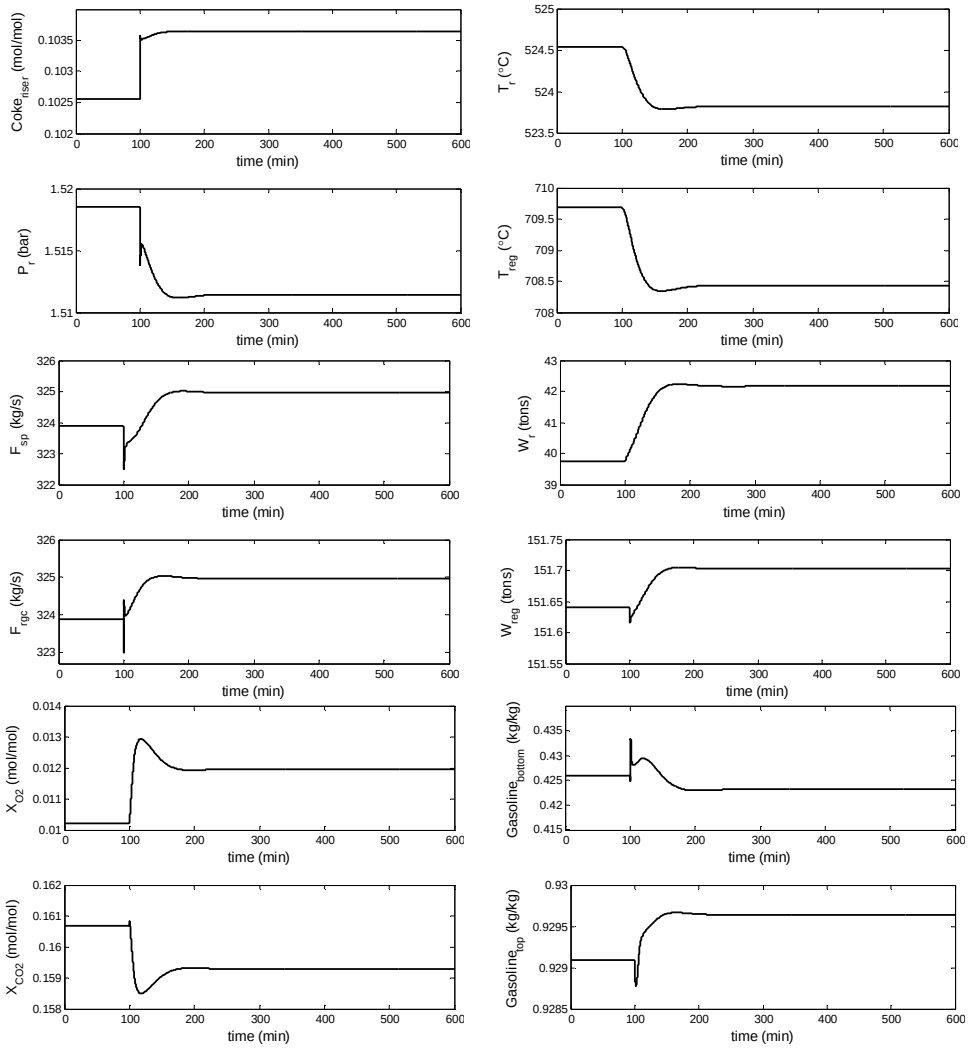

Figure 2. Simulation of FCCU dynamic behavior in the presence of slurry recycle flow rate disturbance (30% decrease at t=100 min)

4. ECONOMICAL ASPECTS

With this simulator it was possible not only to study the process behaviour but it is also possible to investigate the plant gross profit and gasoline octane number, in order to take logical decision concerning the increase in the plant profitability.

Gross Profit of the FCCU can be expressed as follows [6]:

$$\begin{aligned} Profit = & \text{column flow x gasoline composition x cost gasoline} + \\ & + \text{column flow x diesel composition x cost diesel} - \\ & \text{raw material flow x gasoil cost} \end{aligned} \quad (1)$$

Gasoline octane number

The motor octane number (*MON*) and the research octane number (*RON*) have the following expressions [6]:

$$MON = 72.5 + 0.05(T_r - 900^0 K) + 0.17(conversion - 0.55) \quad (2)$$

$$RON = 1.29MON + 12.06 \quad (3)$$

The gasoline octane number (CO) can be calculates with the following formula:

$$CO = \frac{MON + RON}{2} \quad (4)$$

The Plant Gross Profit and Gasoline Octane Number are sensitive in the presence of the slurry recycle flow rate changes as follows:

- 30% decrease in the slurry recycle rate can decrease the plant profit with 7.8% and
- 30% decrease in the slurry recycle rate determine the increase of the *CO* from 93.44 to 93.48

5. CONCLUSIONS

The dynamic behavior of this complex petrochemical process in a wide range of operating conditions and in the presence of disturbances was analyzed by using dynamic mathematical modeling. The new FCCU developed model is sufficiently complex to capture the dynamic effects that occur in an actual FCCU system and is able to depict the main dynamic characteristics of a typical commercial FCC process. Simulations demonstrate the process is multivariable, strongly interacting and highly nonlinear. With the new simulator, economical aspects can be studied (Gross Profit and Gasoline Octane Number). The developed complex model is a very efficient tool to study and to improve the design, safe operation and performance of a modern catalytic cracking unit.

ACKNOWLEDGEMENTS

The authors are also gratefully to the ROMPETROL Company for their support.

REFERENCES

1. M. V. Cristea, S. P. Agachi, V. Marinoiu, *Chemical Engineering and Processing*, **2003**, *42*, 67-91.

2. R. Ellis, X.Li, J. Riggs, AIChE *Journal*, **1998**, *44*, 2068-2079.

3. R. C. McFarlane, R. C. Rieneman, J. F. Bartee and C. Georgakis, *Computers Chemical Engineering*, **1993**,*17*, 275-300.

4. V. Tasoti, *NATO Security through Science Series*, **2007**, 47-56.

5. X. Dupain, E. D. Gamas, R. Madon, C. P. Kelkar, M. Makkee, J. A. Moulijin, *Fuel*, **2003**,*82*, 1559-1668.

6. X. Dupain, M. Makkee, J. A. Moulijn, *Applied Catalysis*, **2006**, *297*, 198-219.

STUDIA UNIVERSITATIS BABEŞ-BOLYAI, CHEMIA, LII, 2, 2007

DETERMINATION OF FATTY ACIDS AND TOTAL LIPID CONTENT IN OILSEED OF SUNFLOWER GENOTYPES GROWN IN ROMANIA

DORINA BRATFALEAN*, D. F .IRIMIE*, P. S. AGACHI*

ABSTRACT. The fatty acids composition of the seed oils from the 10 sunflower inbred lines and 4 hybrids obtained to the National Agricultural Research and Development Institute Fundulea, was qualitatively and quantitatively determined using analytical methodology.

Procedure of research for detection lipids content in sunflower seeds was the conventional extraction, using International Organization for Standardization (ISO). Soxhlet method (SO-extraction) involves the gravimetric determination of sunflower oil using the petroleum extract from oilseeds. The result of Soxhlet method has been detecting a large variability point of view of lipid percent content in hybrids and inbred lines of sunflower. The fatty acids profiles were obtained using laboratory analytical techniques, the methyl ester analysis were made through gas-chromatography. The groups of the fatty acids: C14:00, C15:00, C16:00, C16:01, C17:00, C18:00, C18:01, C18:02, C18:03, C20:00, C20:1 and C22:0 was determined by experiments. Great variation has been observed in fatty acid content of sunflower seeds from 14 Romania genotypes.

1. INTRODUCTION

The sunflower (*Helianthus annuus L.*) is an annual plant in the family *Asteraceae*, with a large flower head [1]. Sunflower is considered the most important oilseed in the world. Lipids play diverse and important roles in nutrition and health. Sunflower seed is considered an important oilseed source crop due its high nutrition oil composition. Sunflower oil, extracted from the seeds, is used for cooking (but is less cardio healthy than olive oil), as a carrier oil and to produce biodiessel, for which it is less expensive than the olive product.

* *"Babes Bolyai" University, Faculty of Chemistry and Chemical Engineering, 11 Arany Janos Street, RO-400028, Cluj-Napoca, Romania,*
Tel: +40264593833, Fax: +40264590818, E-mail: dorinet63@yahoo.com

Fats are an essential nutrient in the human diet, but an unbalanced diet is not healthful. For most individuals, it is appropriate to get 30% of one's daily food energy from fats and oils, evenly divided between monounsaturated, polyunsaturated, and saturated fats [2]. Sunflower is a widely found oilseed species of oleaginous grown in Romania [3]. A large quantity sunflower seeds are source of raw materials required for industrial purposes in human and animal food.

Vegetable oils nowadays are a great source of maintaining oil consummation in families and because of consumers concern with the saturated/unsaturated fatty acid ratio in the diet, the lipid composition of fruit and vegetable has lately received particular attention. Consumers are especially interested in essential fatty acids, with emphasis on the health potential of polyunsaturated fatty acids. These fatty acids play a natural preventive role in cardiovascular disease and in alleviation of some other health problem, because they promote the reduction of both total and HDL cholesterol [4].

2. METHODOLOGY

Samples

Mature sunflower seeds of four hybrids and ten inbred lines (14 genotyeps) were provided by the National Agricultural Research and Development Institute Fundulea. Sunflower seeds were stored at 5°C and low humidity until these were analyzed. Each sample was taken to the laboratory for dry weight determination. Approximately 10 g of sunflower seed at harvesting maturity was sampled for each variety, from which genotype composites were prepared. The genotypes variability is presented in Table 1.

Table 1

Inbreeds lines and hybrids under study

Genotype	LC-A1	LC-A2	LC-A3	LC-A4	LC-A5	EHPA	LC-A6
Type of variety	Semi-precocious	Semi-precocious	Precocious	Tardive	Semi-precocious	Semi-tardive	Semi-tardive
Genotype	LC-A7	LC-A8	LC-A9	H1	H2	H3	H4
Type of variety	Semi-precocious	Precocious	Tardive				

Extraction of total lipid (TL)

The method used for lipids extraction is Soxhlet extraction. The conventional extraction procedure followed in this research was realized according the International Organization for Standardization. Soxhlet method (SO-extraction) involves the gravimetric determination of the oil using the light the petroleum extract from oilseeds [5]. The petroleum extract is called "oil content". Thus, 10 grams of sample (seed material) were weighed and placed in a cellulose extraction cartridge. The cartridge was plugged with cotton wool and then placed in the Soxhlet extractor containing 250 mL of petroleum ether. The oils were recovered by distilling the solvent in a rotary evaporator at 40°C.

Fatty acid methyl ester (FAMEs) preparation

FAMEs were produced to measure content of total fatty acids [6]. First step for FAMEs consist in saponification procedure. Two samples of 0.1g lipid extract from each sunflower variety were esterified with 1 mL methanolic NaOH solution by refluxing for 1h at 100°C. After removal of free fatty acid, the samples were esterified putting 50µL sample with methanolic H_2SO_4 solution was warmed 2h at 80°C. The FAMEs were extracted from a salt saturated mixture with petroleum ether (3.mL). From drying FAMEs, anhydride Na_2SO_4 was added, and then upper part was poured in specific cell.

Gas chromatography system

The fatty acid have been analyses by gas chromatography (GC) following the published methods [5]. The esters were separated by GC (FRATOVAP, Carlo Elba) fitted with a column ((L=2m; d=3mm). Argon was used as carrier gas with the flow of 24mL/min. The temperature of injection port and detector were maintained at 190°C and respectively 225°C. The peaks were identified based on their retention times using authentic standard fatty acids methyl esters and all samples were run in duplicate.

3. RESULTS AND DISCUSSIONS

The results shows values of the oil extraction by extraction with solvents (also raw fat content of the sunflower seeds) (SO) the oil rated capacity was from 41.93% at the LC6 genotype to 49.12% from H1 genotype. In all case, the extract was dependent of genotypes (to see table 2) summarizes

lipophilic extract weight as a percentage of total seed weight. The percentage of lipids in Romanian hybrids is under 45%. (from H3 47.13% to H2 49.12%). A large majority of the total lipids extract weight was corresponding to the twelve detected fatty acids, in all these cases. The groups of the fatty acids detected (C14:00, C15:00, C16:00, C16:01, C17:00, C18:00, C18:01, C18:02, C18:03, C20:00, C20:01, C22:00) were determinate by experiments. Great variation has been observed in fatty acid content of sunflower seeds from 14 Romania genotypes (10 inbred line, and four hybrids).

Table 2

Total lipids and fatty acid composition [a] of Romania sunflower seeds

Geno-types	Lipids (%)	Fatty acid %											
		C14:0	C15:0	C16:0	C16:1	C17:0	C18:0	C18:1	C18:2	C18:3	C20:0	C20:1	C22:0
LC1	46.79	0.017	0.008	6.742	0.067	0.113	3.892	31.592	56.468	0.372	0.100	0.060	0.569
LC2	47.80	0.023	0.014	7.353	0.074	0.178	4.508	48.599	37.501	0.484	0.098	0.051	1.117
LC3	42.98	0.016	0.009	6.699	0.117	0.019	3.021	41.931	46.814	0.39	0.056	0.096	0.832
LC4	46.06	0.020	0.017	6.769	0.166	0.093	4.808	40.271	46.271	0.436	0.224	0.091	0.834
LC5	45.95	0.121	0.087	5.569	0.121	0.084	3.79	38.688	49.936	0.345	0.185	0.206	0.868
LC6	41.93	0.180	0.027	4.978	0.104	0.057	3.797	41.43	47.762	0.515	0.144	0.182	0.824
LC7	45.13	0.133	0.027	6.947	0.185	0.078	5.671	39.624	45.702	0.439	0.073	0.056	1.065
LC8	48.05	0.158	0.103	6.226	0.194	0.045	4.245	46.63	39.73	0.739	0.167	0.275	1.488
LC9	44.05	0.161	0.021	6.978	0.114	0.107	5.465	43.159	42.000	0.698	0.042	0.072	1.183
LC10	45.21	0.141	0.076	6.647	0.232	0.078	2.598	35.42	53.200	0.524	0.132	0.079	0.873
H1	47.75	0.138	0.065	7.381	0.079	0.035	3.661	28.966	58.337	0.444	0.072	0.093	0.729
H2	49.12	0.113	0.05	7.375	0.195	0.064	4.754	25.024	60.788	0.568	0.042	0.150	0.877
H3	47.13	0.206	0.061	7.569	0.123	0.127	5.014	27.037	58.107	0.503	0.155	0.170	0.928
H4	48.95	0.196	0.007	7.215	0.195	0.103	5.235	25.65	60.112	0.408	0.145	0.165	0.569

*Percentage by weight of total fatty acids identified by GC as FAMEs

Based on our study, the sunflower seeds of all 14 genotyeps so far had similar, fatty acid compositions and low amount of saturated fatty acids. Intervarietal differences in fatty acids composition were found and they can be used to establish chemotaxonomic differences, which have also been shown in some other species. A large variability of saturated fatty

acids content was detected between sunflower inbred lines and hybrids (from 10.007% to 14.060%). The unsaturated fatty acids variability is between 85.94% - 89.99%. Sunflower genotypes seed can be classified taking into account linoleic acid/oleic acid ratio (from 0.77% inbred line LC2 to 2.43% hybrid H2).

Table 3

Acids profile in 14 sunflower genotypes and ratio between saturated and unsaturated acid

Geno-types	Total % Saturated fatty acids	Total % Mono saturated fatty acids	Total % Poly saturated fatty acids	Total % Unsaturated fatty acids	Saturated/ unsaturated acid ratio	Linoleic acid/oleic acid ratio
LC1	11.441	31.719	56.840	88.559	0.129	1.787
LC2	13.291	48.724	37.985	86.709	0.153	0.772
LC3	10.652	42.144	47.204	89.348	0.119	1.116
LC4	12.765	40.528	46.707	87.235	0.146	1.149
LC5	10.704	39.015	50.281	89.296	0.120	1.291
LC6	10.007	41.716	48.277	89.993	0.111	1.153
LC7	13.994	39.865	46.141	86.006	0.163	1.153
LC8	12.432	47.099	40.469	87.568	0.142	0.852
LC9	13.957	43.345	42.698	86.043	0.162	0.973
LC10	10.545	35.731	53.724	89.455	0.118	1.502
H1	12.081	29.138	58.781	87.919	0.137	2.014
H2	13.275	25.369	61.356	86.725	0.153	2.429
H3	14.060	27.330	58.610	85.940	0.164	2.149
H4	13.470	26.010	60.520	86.530	0.156	2.344

4. CONCLUSIONS

Acid profile obtained after GC analysis is helpful to choose the possible utilization of the oil: food industry or carrier oil. These cultivars might contain useful genetic resource for the development of novel varieties. The four Romania hybrids (H1, H2, H3, H4) used in this study contain highly unsaturated fatty acids, having good nutritional quality.

ACKNOWLEDGEMENTS

The authors would like to acknowledged the support for providing the sunflower seeds genotypes at Agricultural Research and Development Institute Fundulea, Romania

REFERENCES

1. Amy E. Bionkoski and the group "*Balance of unsaturated fatty acids .Is important to a cholesterol –Lowering Diet"* Journal of the American Dietetic Association. **2005**

2. AOAC, "*Official Method of Analysis*". Association of Official Analytical Cereal Chemists, Washington, DC, USA. **1999**.

3. D. Brătfălean, F.D. Irimie, S.P. Agachi, D. Stanciu, I. Sorega, "*Variability study of fats acids on 13 Romanian genotype of sunflower oil by Gas Chromatography*", Cercetari de genetica vegetala si animala, Bucuresti **2006,** pp33-38

4. P. Melgarejo and F. Artes, "*Total lipids and fatty acid composition of oil seed from lesser known sweet pomegranate clones*", Journal of the Science of Food and Agriculture 80(**2000**), pp1452-1454

5. R. Shostek, "Flowers and Plants. An International Lexicon with Biographical Notes". Quadrangle /The New York Times Book Co. **1974**, pp 329

STUDIA UNIVERSITATIS BABEŞ-BOLYAI, CHEMIA, LII, 2, 2007

CATALYTIC SYNTHESIS OF HYDROGEN IODIDE FROM IODINE AND WATER IN THE PRESENCE OF CARBON MONOXIDE AS REDUCING AGENT

JENŐ BÓDIS*

ABSTRACT. A catalytic synthesis for hydrogen iodide (a co-catalyst source for Reppe reactions) from iodine, water and carbon monoxide is reported. Beside the well known noble metal catalyst (e.g., rhodium, iridium), iron (powder) and iron compounds (e.g., $Fe(CO)_5$, FeI_2) were found to have high and constant activities in the HI formation during reactions performed on recycled catalysts. The induction period observed with iron and iron compounds as catalyst precursor in the first catalytic reaction is completely missing in the advanced ones.

Keywords: Hydrogen iodide, Catalytic synthesis, Co-catalysts, Carbonylations

INTRODUCTION

Hydrogen iodide and alkyl iodides are effective co-catalysts for the carbonylation reactions of alcohols and the hydrocarboxylation reactions of alkenes or alkynes, known under the common name of Reppe reactions [1-10]. As the hydrogen iodide is very corrosive, it is recommended that its use in industrial reactors should be avoided. Fortunately, this is possible, since under the conditions of the Reppe reactions the hydrogen iodide changes into alkyl iodides and these latter ones intervene effectually in the catalytic cycle. In view of avoiding the advanced corrosion processes of the bulky carbonylation reactors, the alkyl iodides (methyl iodide and ethyl iodide) used in the industrial processes must be synthesized separately in low volume reaction vessels. Methyl iodide, the co-catalyst of the carbonylation reaction of methanol to acetic acid can be obtained according to the following chemical reaction [1,7]:

* "Babes-Bolyai" University, Department of Organic Chemistry, 11 Arany Janos str., 400028 Cluj-Napoca, Romania.
E-mail: jbodis@chem.ubbcluj.ro, Fax: 40-264-590818

$$CH_3OH + HI \rightarrow CH_3I + H_2O$$

whereas ethyl iodide, the co-catalyst for the carbonylation reaction of ethanol as well as for the hydrocarboxylation reaction of ethylene to propionic acid can be won according to the reaction [1,7]:

$$CH_3CH_2OH + HI \rightarrow CH_3CH_2I + H_2O$$

The synthesis of hydrogen iodide from elemental iodine and water under the reducing action of carbon monoxide requires the presence of noble metal catalysts, for example salts or complexes of rhodium or iridium [7,11,12] and takes place in accordance with the chemical equation:

$$I_2 + CO + H_2O \rightarrow 2\,HI + CO_2$$

Owing to the fact that the reaction takes place in the liquid phase and that the recovery of rhodium and iridium, very expensive noble metals, raises serious technical difficulties, cheaper transition metals have been tested as catalysts in the synthesis of hydrogen iodide.

EXPERIMENTAL

Elemental iodine (p.a.) and hydrogen iodide (57%) of FLUKA origin have been used. The distilled water and carbon monoxide (99.5%) have been prepared in the "Babes-Bolyai" University (BBU) laboratory. CO has been prepared by means of the catalytic dehydration of the technical formic acid with concentrated sulphuric acid. The gas thus formed has been neutralized by bubbling through a solution of sodium hydroxide and is collected in a gas reservoir, from whence it is compressed in gas cylinders. The absolute methanol (p.a., 99,5%) has been provided by the "Chimopar" Bucharest. The transition metal salts (p.a.) used as catalyst precursors are of Merck and FLUKA origin. $[Rh(CO)_2Cl]_2$ and $Fe(CO)_5$ have been prepared in the BBU laboratory. The basic diagram of the batch-type hydrogen iodide production equipment is represented in Figure 1.

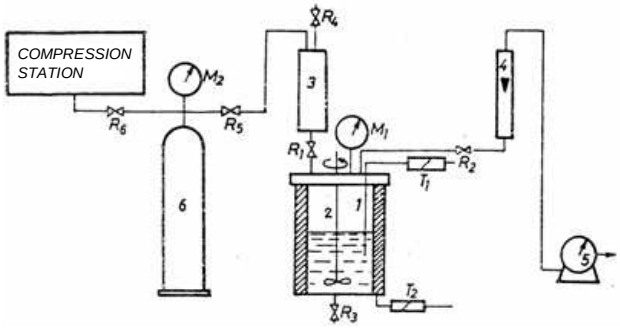

Figure 1. Diagram of the hydrogen iodide preparation (Legend in the text).

The equipment consisted of an autoclave (1) of 200 cm^3 volume, manufactured from corrosion-resisting Hast-Alloy C, fitted with a magnetic stirrer (2) and a heating system steered by a heat regulator with a chromel-coppel T_2 thermocouple. The temperature of the reaction vessel was measured by an iron-constantan thermocouple T_1. The valves R_1, R_2 and R_3 were also made of Hast-Alloy C. The autoclave pressure has been measured by means of manometer M_1, equipped with a separating Teflon membrane. As carbon monoxide source a gas cylinder (6) of 40 l has been used, equipped with the manometer M_2 containing the CO compressed at 150 bar. The pressure vessel (3) made of Hast-Alloy C, directly linked to the autoclave through valve R_1 is used for the injection of the solution composed of elemental iodine, water, hydrogen iodide (57% aqueous solution) and catalyst. After the introduction of the reaction mixture, the air was removed by means of repeated purging with CO. Then the heating was started and on reaching the running temperature, by means of the inlet valve R_1 and the evacuation valve R_2 for the CO, the pressure was adjusted to the desired value. The gas output was measured by the rotameter (4) and the wet gas meter (5). The moment of determining the operating pressure counts as the time $t_0 = 0$ at the time-dependent inspection of the reaction. The kinetic measurements have been carried out at constant temperature and pressure. The gas output flow rate has been kept between 4-6 l/h.

The reaction has been followed by monitoring the decrease of the elemental iodine concentration and the increase of the hydrogen iodide concentration against time. The variation of the composition of the solution contained in the autoclave has been determined on the basis of the samples taken through valve R_3 at definite time intervals. The volume of a sample was approximately of 0.5-1 cm^3. The concentration of the elemental iodine has been volumetrically measured by titration with a 0,1 N solution of $Na_2S_2O_3$ in the presence of starch.

The actual concentration of the hydrogen iodide has been obtained by means of titration with a 0,1 N solution of sodium hydroxide in the presence of phenolphthalein. Because the free iodine disturbs the titration of the hydrogen iodide, the iodine has been extracted in advance with carbon tetrachloride. On the basis of the instantaneous values of the concentration of the free iodine $[I_2]$ and of those of the hydrogen iodide [HI] respectively, and taking into consideration their initial concentrations $[I_2]_0$ and $[HI]_0$, their momentary conversions have been calculated (X_{iodine} and X_{HI}) according to the relations:

$$X_{iodine} = ([I_2]_0 - [I_2])/[I_2]_0; \qquad X_{HI} = ([HI] - [HI]_0)/2[I_2]_0$$

The conversion curves obtained by the graphical representation of X = f(t) served for the study on the reproducibility of the process and for the study on the influence of the reaction parameters upon the conversion. It has been furthermore inquired into the possibility of reusing the catalytically active species in more catalytic cycles.

RESULTS AND DISCUSSION

Figure 2 presents the conversion curves obtained as a result of the use of the $[Rh(CO)_2Cl]_2$ (curve 19) and the $Co(CH_3COO)_2 \cdot 4H_2O$ (curve 20) as catalyst precursors.

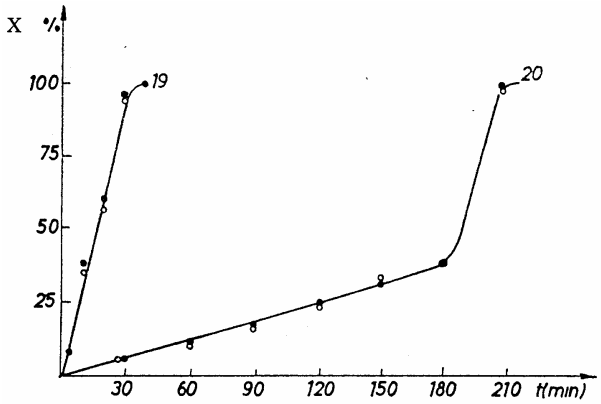

Figure 2. Conversion curves of hydrogen iodide synthesis in two significant experiments: (19)-catalyst $[Rh(CO)_2Cl]_2$, [Rh] = 3,4 10^{-3} mol/l, P = 10 bar; (20)-catalyst $Co(CH_3COO)_2 \cdot 4H_2O$, [Co] = 0,175 mol/l, P = 50 bar. Conditions: $[I_2]_0$ = 0,71 mol/l, $[H_2O]_0$ = 3,33 mol/l, $[HI]_0$ = 1,933 mol/l, T = 130 °C; (●)- calculated from the consumption of I_2, (○)-calculated from the increase of the HI concentration.

In case of these experiments the actual conversions have been calculated as well as from the elemental iodine consumption as from the increase of the hydrogen iodide concentration. It follows from these diagrams that the conversion values determined on the basis of the two variants lies on the same curve, within the limit of experimental errors. However, the values calculated from the increase of the HI concentration are systematically somewhat lower than those calculated from the decrease of the elemental iodine concentration, but the differences are insignificant. The minor systematic error is probably owing to the loss of HI occurring as a result of the extraction of iodine from the aqueous solution with carbon tetrachloride. Subsequently, the calculation of conversion in most experiments has been performed only by means of determining the iodine consumption.

In view of studying the reproducibility of the hydrogen iodide synthesis many experiments in identical conditions have been conducted. Figure 3 illustrates the conversion curves obtained for two experiments performed in the presence of $Fe(CO)_5$ under identical conditions.

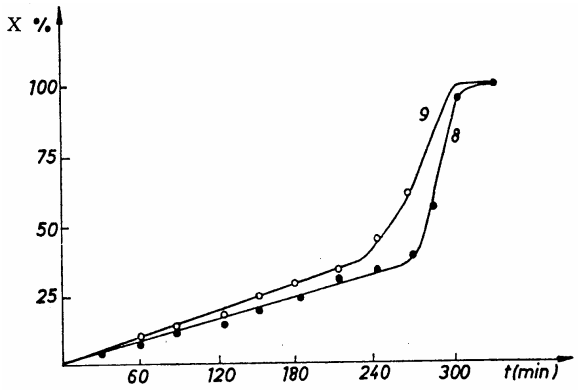

Figure 3. Conversion curves for two HI syntheses catalyzed by $Fe(CO)_5$ carried out under identical conditions P = 50 bar, T = 130 °C, [Fe] = 0,175 mol/l, $[I_2]_0$ = 0,71 mol/l, $[HI]_0$ = 1,933 mol/l, $[H_2O]_0$ = 3,33 mol/l.

The rate of the conversion curves displayed an acceptable reproducibility merely for the first phase, which being slow, was also called the induction period of the reaction. In the rapid phase, as the speed was considerably higher, the density of the experimental data was reduced and the conversion determination errors were higher. From the combinations of cheaper transition metals only those of Fe and Co have displayed catalytic activity in the reaction of hydrogen iodide formation from

elemental iodine and water in the presence of CO. Figure 4 represents the conversion curves obtained as a result of the use of different compounds of iron and cobalt as catalysts and the conversion curve obtained with the $[Rh(CO)_2Cl]_2$ catalyst (curve 19) which was considered the reference curve.

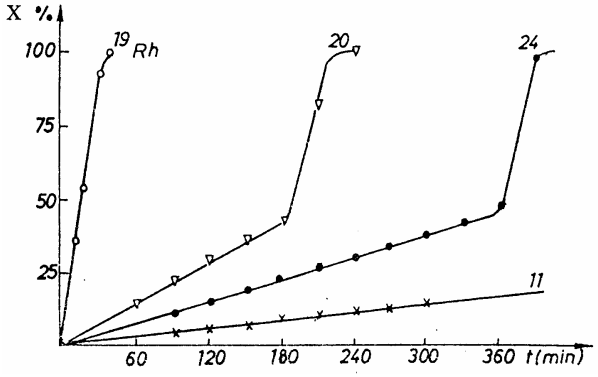

Figure 4: Diagrams X = f(t) for HI synthesis in the absence and presence of transition metal compounds. (11)-without catalyst, P = 50 bar; (19)-$[Rh(CO)_2Cl]_2$, [Rh] = $3.4 \cdot 10^{-3}$ mol/l, P = 10 bar; (20)-$Co(CH_3COO)_2 \cdot 4H_2O$, (24)-$FeSO_4 \cdot 7H_2O$, [Fe] = [Co] = 0,175 mol/l, P = 50 bar; T = 130 °C, $[I_2]_0$ = 0,71 mol/l, $[HI]_0$ = 1,933 mol/l, $[H_2O]_0$ = 3,33 mol/l.

The experiments (20) and (24) reveal that the reaction had an auto-acceleration character. Thus, the first slow stage corresponds to the phase of formation of a catalytically active species from the utilized precursor catalyst. The formation of the active catalyst is immediately followed by the rapid reduction of elemental iodine to hydrogen iodide. It follows from the analysis of the conversion curves (20) and (24) that the catalytic activity of the Fe and Co compounds is close, the incline of the two curves is in the rapid phase similar. However, the time necessary for the formation of the effective catalysts from the precursors differs. The formation of the catalytically active species from cobalt acetate occurs more rapidly than that from ferrous sulphate. Nevertheless, in both cases one can observe the auto-acceleration which is owing to the formation of the catalytically active species from the precursor initially employed.

The temporal sequence of the reaction in the presence of the iron catalyst is dependent on the nature of the compound utilized as a precursor. Figure 5 illustrates the conversion curves obtained with different iron compounds used as catalyst precursors.

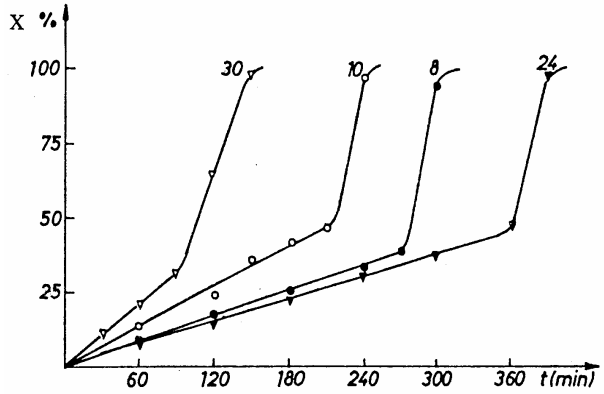

Figure 5. Representations X = f(t) obtained for the HI synthesis as a result of the use of iron compounds as catalyst precursors. (8)-$Fe(CO)_5$, (10)- Fe powder, (24)-$FeSO_4 \cdot 7H_2O$, (30)-FeI_2; P= 50 bar, T = 130 °C, $[I_2]_0$ = 0,71 mol/l, $[HI]_0$ = 1,933 mol/l, $[H_2O]_0$ = 3,33 mol/l.

It follows from the diagram that from the different tested iron compounds, the catalytically active species were formed the most rapidly from iron iodide and iron powder. The presence of SO_4^{2-} anion seems to be disturbing the catalytic process (curve 24).

Furthermore, it has been suggested that one should temporally examine the HI syntheses in the presence of catalysts preformed from FeI_2 or iron powder in a previous experiment. Due to the injection of the stoichiometric quantity of methanol at the boiling temperature of iodomethane (43 °C), the hydrogen iodide previously formed was transformed in methyl iodide, which gets distilled from the system. Once again the I_2 solution and the stoichiometric quantity of water were injected in the autoclave. After several purging with CO, the reaction mixture was warmed up at 130 °C and the working pressure was set with CO at 10 bar. Figure 6 comparatively presents the conversion curves obtained under identical conditions for the $[Rh(CO)_2Cl]_2$ catalyst (curve 19) and an iron catalyst preformed in a former experiment (curve 32). In this case representations X = f(t) no longer have an inflexion point. As anticipated, the slow phase, the stage of formation of the active species from the precursor, is missing. Accordingly, the active species once formed from the iron precursor maintains its catalytic activity. Furthermore, it does not get deactivated even during the synthesis of the methyl iodide which takes place at atmospheric pressure and in the absence of the CO atmosphere.

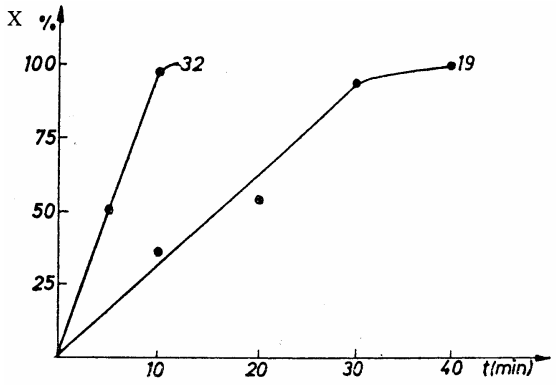

Figure 6. Comparison of the activity of the recycled iron catalyst to that of the rhodium under the following concentration ratios: [Fe]:[Rh] = 50, (19)- $[Rh(CO)_2Cl]_2$, (32)- catalyst preformed from FeI_2, P= 10 bar, T = 130 °C, $[I_2]_0$ = 0,71 mol/l, $[HI]_0$ = 1,933 mol/l, $[H_2O]_0$ = 3,33 mol/l.

Figure 6 shows, that under a concentration ratio of [Fe]/[Rh] = 50, the preformed iron catalyst is more effective than that of rhodium. On calculating the reaction speeds from the slope of the two curves, it is found that the rate of reaction is 3 times higher in the case of the preformed iron catalyst. Accordingly, at an iron concentration of 16,5 ·[Rh] it is possible to effect a performance similar to that of the rhodium catalyst.

CONCLUSIONS

Hydrogen iodide can be prepared under favorable conditions from elemental iodine, water and carbon monoxide in the presence of adequate catalysts. Thus, rhodium and iron salts or other type of compounds of these metals can thereby function as catalysts. During the catalytic synthesis of HI on recycled iron catalysts, the catalytically active species formed from iron powder or iron iodide (FeI_2) becomes more effective due to the absence of the induction period initially observed and maintains an increased activity throughout more catalytic cycles.

REFERENCES

1. A. Mullen, "Carbonylations catalyzed by metal carbonyls-Reppe reactions", in New Syntheses with Carbon Monoxide, J. Falbe, ed., Springer-Verlag, Berlin/Heidelberg/New York, 1980, pp. 243-308.
2. B. P. Curtis Jr., L. W. Fannin, F. E. Paulik and J. L. Price, US Pat., 3, 761, 579 (1973).
3. E. Campean, J. Bódis, C. Virágh, F. Kacsó, L. Zador and N. Almási: RO Pat., 102686 (1993).
4. J. Bódis and J. Mink, Polymer Preprints, 42 (2001) 624; b) J. Bódis and J. Mink: Abstracts of papers of the American Chemical Society, 221: 178-POLY Part 2 Apr. 1, 2001, Publisher: American Chemical Society, ISSN: 0065-7727.
5. J. Bódis, "Carbonylation of methanol over supported rhodium catalysts: Kinetic and FT-IR spectroscopic investigations", in In-situ Monitoring of Monomer and Polymer Synthesis, J. E. Puskas, T. E. Long and R. F. Storey, eds., Kluwer Academic/ Plenum Publishers, New York /Boston/ Dordrecht/ London/ Moscow, 2003, pp. 187-205.
6. J. Bódis, J. Zsakó, Cs. Németh and J. Mink, Vibrational Spectroscopy, 9 (1995) 197.
7. J. Bódis, PhD Thesis, Babeş-Bolyai University of Cluj, (1995).
8. J. Bódis, Rev. Chim., 56 (10) (2005) 1062.
9. J. Zsakó J. Bódis, E. Campean, Á. Imre and N. Palibroda, Progress in Catalysis, 4 (1995) 1.
10. K. K. Robinson, A. Hershman, J. H. Craddock and J. F. Roth, J. Catal., 27 (1972) 389.
11. M. J. Howard, M. D. Jones, M. S. Roberts and S. A. Taylor, Catalysis Today, 18 (1993) 325.
12. N. Almási, E. Campean, F. Kacsó, C. Virágh, J. Bódis, V. Coşoveanu, RO Pat., 102505 (1992).

STUDIA UNIVERSITATIS BABEŞ-BOLYAI, CHEMIA, LII, 2, 2007

ELECTROCHEMICAL INVESTIGATION OF THE INFLUENCE OF TWO THIADIAZOLE DERIVATIVES ON THE PATINA OF AN ARCHAEOLOGICAL BRONZE ARTEFACT USING A CARBON PASTE ELECTRODE

ADRIANA VLASA*, SIMONA VARVARA, LIANA M. MUREŞAN***

ABSTRACT. The efficiency of two non-toxic thiadiazole derivatives (2-mercapto-5-R-acetylamino-1,3,4-thiadiazole and 2-mercapto-5-R-amino-1,3,4–thiadiazole) as corrosion inhibitors for bronze patina in aqueous electrolytes containing sodium sulphate and sodium hydrogen carbonate (pH 3) was studied by using a carbon paste electrode. The obtained results show the influence of the tested inhibitors on the electrochemical behaviour of patina, the strongest effect being noticed in the case of 2-amino-5-mercapto-1,3,4-thiadiazole.

Keywords: patina, bronze corrosion; corrosion inhibitor; thiadiazole derivatives, carbon paste electrode

1. INTRODUCTION

During interaction between archaeological bronze artefacts and the surrounding environment, these ancient objects became covered with a layer of corrosion products, called *patina*, whose composition strongly depends on the corrosive medium [1, 2]. Depending on the environmental conditions, the patina layer has a bluish, a green or even a brown colour, conferring to the artefacts an attractive aspect. Moreover, once formed, the patina is relative stable and acts as a protective barrier of the bronze artefact under many exposure conditions [3]. Due to these reasons and to the fact that the patina hides important archaeological information, this layer is carefully preserved on the surface of bronze artefacts. However, its stability can change under the influence of the environment and the corrosion starts

* "Babes-Bolyai" University, Department of Physical Chemistry, 11 Arany Janos St., 400028 Cluj-Napoca, ROMANIA.*E-mail: limur@chem.ubbcluj.ro

**"1 Decembrie 1918" University, Dept. of Topography, 11-13 Nicolae Iorga St., 510009 Alba Iulia, ROMANIA.

again [4]. Even archaeological bronze artefacts exposed in museum or stored in conservation room are submitted to degradation process. Therefore, in order to avoid this inconvenient, suitable treatment with coating substances are often required.

To this regard, a range of corrosion inhibitors, mainly nitrogen and sulphur-containing organic heterocyclic compounds developed for industry were tested in the conservation-restoration laboratories aiming to find a suitable corrosion inhibitor for the ancient artefacts. Among them, benzotriazole (BTA) has been widely accepted in the stabilization of copper and bronze artefacts being considered as the most efficient corrosion inhibitor over a wide temperature and pH range. However, BTA is highly toxic and its use is nowadays quite limited also because the conservation practice has proved that the stabilization of bronze artefacts with BTA is not always successful; the treatment may result in a darkening of the patina and, in some cases, in the development of a slight gloss [5].

Recently, in an attempt to characterize the effect of inhibitors on the electrochemical behaviour of patina isolated from the bronze substrate, the use of a cavity microelectrode was reported [6]. Inspired by this idea and by the possibility to avoid the influence of bronze substrate on the electrochemical response of the patina, the present work proposes the using of a carbon paste electrode for its electrochemical investigation. The influence of two non-toxic thiadiazole derivatives: 2-mercapto-5-R-acetylamino-1,3,4-thiadiazole (MAcT) and (2-mercapto-5-R-amino-1,3,4-thiadiazole (MAT) on the electrochemical behaviour of the patina scratched from the surface of an archaeological bronze artefact and incorporated in carbon paste was investigated in an electrolyte containing Na_2SO_4 and $NaHCO_3$ (pH 3) by cyclic voltammetry and polarization measurements.

The composition of patina was determined by SEM-EDS analysis.

2. EXPERIMENTAL

Materials

Experiments were carried out in an aerated solution of 0.2g/l Na_2SO_4 + 0.2g/l $NaHCO_3$, acidified to pH=3 by addition of dilute H_2SO_4.

2 mercapto-5-R-acetylamino-1,3,4-thiadiazole **(MAcT**) and 2 mercapto-5-R-amino-1,3,4 -thiadiazole (**MAT**) were synthesized in the laboratories of the Faculty of Pharmacy from Cluj-Napoca, Romania and their molecular structures are presented in figure 1.

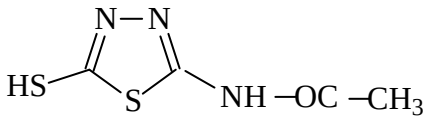

MAcT

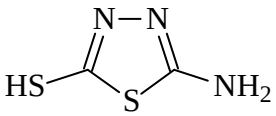

MAT

Figure 1. Molecular structure of the inhibitors

Graphite powder and paraffin oil were purchased from Fluka (Buchs, Switzerland).

All other chemicals were of analytical grade and used as received.

The investigated Transylvanian archaeological bronze artefact covered with patina layer was a pin of bronze, datable back to the Eneolithic period (around 3800 B.C.) and provided by the "1 Decembrie 1918" University of Alba-Iulia.

Preparation of carbon paste electrode

25 mg of patina gently scratched from the surface of the bronze pin were mixed with 25 mg graphite powder and 10µl paraffin oil in order to obtain the modified carbon paste electrodes. This composition was put in the cavity of a Teflon bar, forming the head of a disc electrode. Prior to all measurements, the carbon paste electrode was gently polished on paper.

Methods

In-depth composition of the metallic artefact and of the patina formed on its surface was determined by SEM-EDS analysis. A very small surface from the cross-section area of the pin was gently polished with emery paper up to the grade 1200 and finished with alumina powder. After taking SEM observation of the bronze pin (Leica model Stereoscan 440 controlled by LEO software), the composition of the artefact and of the patina was determined by EDS (Princeton Gamma-Tech, model Spirit).

Cyclic voltammetry and polarisation measurements were conducted using an electrochemical analyzer (Autolab-PGSTAT 10, EcoChemie, Utrecht, Netherlands) connected to a PC for potential control and data acquisition. The electrochemical experiments were performed in a three-electrode cell with a separate compartment for the reference electrode connected with the main compartment *via* a Luggin capillary. The working electrode was a carbon paste electrode incorporating the patina, the reference electrode was a saturated calomel electrode (SCE) and the counter electrode was a platinum foil.

3. RESULTS AND DISCUSSION

3.1 SEM and EDS measurements

The results concerning the structural and morphological characterization of the Transylvanian archaeological bronze pin covered with patina layer are presented in figure 2 and Table1.

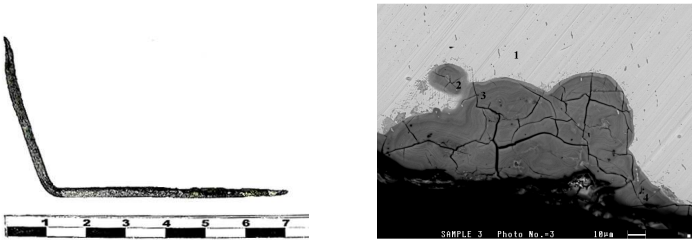

Figure 2. Bronze bended pin and SEM picture of the bronze artefact covered with a patina layer

On the points marked from 1 to 4, EDS analyses were performed, and the results are displayed in Table 1. The percents presented here were normalised with respect to the total amount of elements analysed. The carbon was not analysed quantitatively.

Table 1.

Composition of the patina layer determined by EDS in the points marked 1-4.

	Cu	Sn	Ni	Al	Fe	Cl
1	94.42	4.47	0.21	0.89	-	-
2	31.91	6.69	0.07	-	0.03	4.30
3	16.12	13.66	0.08	-	0.08	0.54
4	11.98	11.81	0.03	-	0.07	0.35

*the rest to 100% represents O

As can be observed, the investigated artefact is essentially a Cu-Sn binary alloy with a small amount of Ni as impurity. The Al detected in the EDS spectra is due to the alumina powder used for polishing a small area of the artefact.

The patina consists mainly of Cu and Sn oxides. It is interesting to note that the Sn content in patina is higher than that in bronze matrix. This phenomenon is known as "decuprification process" or a preferential dissolution of Cu [4]. The presence of Cl^- ions in the patina is due to the contact between the artefact and the soil in which it was buried during centuries.

3.2 Electrochemical measurements

The cyclic voltammograms performed with the carbon paste electrode incorporating patina in the absence and in the presence of **MAT** are presented in figure 3.

As can be observed, in the absence of additive, one anodic and one cathodic peak appear, corresponding to the oxidation/reduction of Cu/Cu^{2+} redox couple. In the presence of **MAT**, two anodic peaks were put on evidence: the peak at less positive potentials decreases with the increase of additive concentration, and the other one increases with the concentration of **MAT**. The two peaks were attributed to the dissolution of the copper deposited during the cathodic scan and to the oxidation of a complex formed between Cu(I) ions and the thiadiazole derivative, in which the thiadiazole derivatives act as bidentate ligands through the aminic nitrogen atom and the closed ring nitrogen in the complex [7]. An increase of inhibitor concentration leads to an increase of complex concentration and thus, of the second peak height and to a decrease of the first peak, due to the inhibition of copper dissolution.

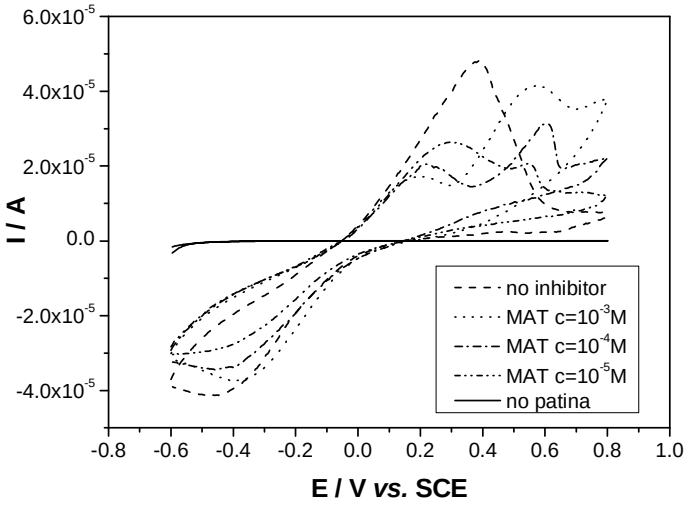

Figure 3. Cyclic voltammograms recorded in 0.2g/l Na_2SO_4 + 0.2g/l $NaHCO_3$ (pH=3) using a carbon paste electrode incorporating patina, in the absence and in the presence of **MAT**. Scan rate 0.02 V/s.

When **MAcT** is used (figure 4), two anodic peaks are observed on the voltammograms as well, their height being correlated with the concentration of the organic compound: the larger the inhibitor amount, the higher the two peak currents. However, the currents are lower than in the case of **MAT** (Table 2).

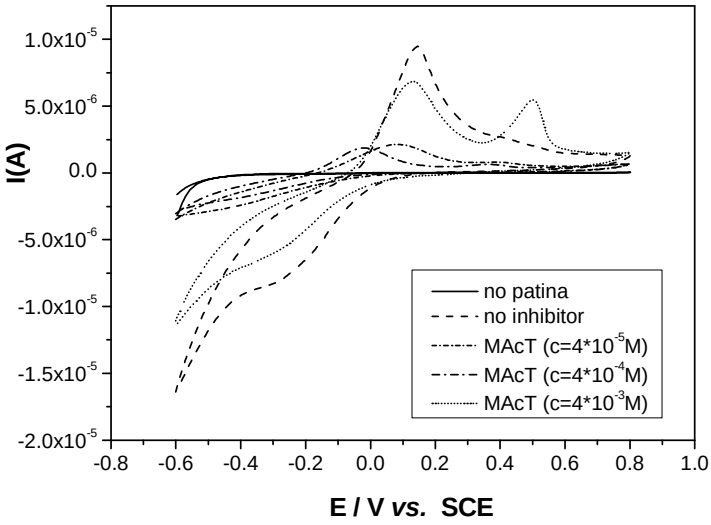

Figure 4. Cyclic voltammograms recorded in 0.2g/l Na_2SO_4 + 0.2g/l $NaHCO_3$ (pH=3) using a carbon paste electrode incorporating patina in the absence and in the presence **MAcT**. Scan rate 0.02 V/s

An explanation for this behaviour could be the depletion in electrons of the aminic nitrogen bound to the thiadiazole ring, due to the presence of the acetyl group in the molecule of **MAcT**, which leads to a poorer tendency of this compound to form a complex with Cu(I) ions. This behaviour suggests that **MAcT** has a slighter influence on the patina behaviour than **MAT**.

Table 2. Electrochemical parameters of the voltammograms recorded on the carbon paste electrode incorporating patina in the absence and in the presence of the two thiadiazole derivatives; electrolyte 0.2g/l Na_2SO_4 + 0.2g/l $NaHCO_3$ (pH=3).

Inh	Conc. (M)	$\varepsilon_{pa,1}$ (V *vs.* SCE)	$\varepsilon_{pa,2}$ (V *vs.* SCE)	ε_{pc} (V *vs.* SCE)	$I_{a,1}$ (A)	$I_{a,2}$ (A)	I_c (A)
-	0	0.385	0	0.373	$4.889 \cdot 10^{-5}$	0	$1.128 \cdot 10^{-5}$
MAT	$4 \cdot 10^{-3}$	0.146	0.554	0.324	$7.608 \cdot 10^{-6}$	$1.127 \cdot 10^{-5}$	$1.532 \cdot 10^{-5}$
MAcT	$4 \cdot 10^{-3}$	0.129	0.504	0.059	$6.148 \cdot 10^{-6}$	$3.554 \cdot 10^{-6}$	$5.202 \cdot 10^{-6}$

According to [7], the efficiency of both organic inhibitors could be associated to the extent to which they adsorb and cover the electrode surface, knowing that their adsorption depends on their structure and on the surface charge of the metal.

The polarisation curves recorded with the carbon paste electrode incorporating patina, in the absence and in the presence of the two thiadiazole derivatives in the solution are shown in figure 5.

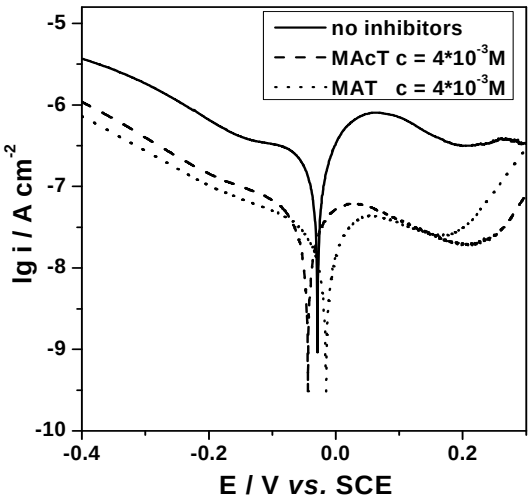

Figure 5. Influence of thiadiazole derivatives on the anodic and cathodic polarization curves of carbon paste electrode incorporating patina recorded in 0.2 g/l Na_2SO_4 + 0.2 g/l $NaHCO_3$ (pH=3). Scan rate 10 mV/min.

As can be noticed, the addition of thiadiazole derivatives gives rise to decreases of both cathodic and anodic current densities, as compared to the blank solution, in the whole applied potential range. This indicates that the investigated organic compounds inhibit the process by increasing the charge transfer resistance of the anodic dissolution of copper and acting as barriers to the diffusion of oxygen molecules from the solution to the electrode surface. Disregarding their molecular structure, the two thiadiazole derivative appears to have a more pronounced effect on the anodic process than on the cathodic one.

4. CONCLUSIONS

The new electrochemical method proposed for the study of patina originating from the surface of bronze objects, after its incorporation in carbon paste, seems to be an interesting alternative to cavity microelectrode method and can be used to characterize the effect of inhibitors on the electrochemical behaviour of the patina. Open circuit potential measurements and electrochemical impedance investigations, performed on the same experimental system, will be performed in order to obtain additional data on the inhibition mechanism of the two thiadiazoles.

The results of preliminary electrochemical investigations show that 2 mercapto-5-R-acetylamino-1, 3, 4-thiadiazole seems to have a slighter effect on the electrochemical behaviour of the patina than 2 mercapto-5-R-amino-1, 3, 4-thiadiazole in the investigated electrolyte.

ACKNOWLEDGEMENTS

The authors thank Prof. Dr. Robert Sandulescu, from "Iuliu Hatieganu" University of Medicine and Pharmacy of Cluj-Napoca for supplying us the thiadiazole derivatives, and to Prof. Dr. Iuliu Paul from "1 Decembrie 1918" University of Alba Iulia for providing the ancient bronze artefact. The financial support from EGIDE, France (Project ECO-net No. 10279NA/2005, 2006) is gratefully acknowledged.

REFERENCES

1. A. Kratschmer, I. O. Wallinder, C. Leygraf, Corrosion Science 44 (2002) 425-450.

2. B. Rosales, R. Vera, G. Moriena, Corr. Sci. 41 (1999), 625.

3. K. Rahmouni, *Formation et caracterisation de la patine de bronze,* Thèse de doctorat, Université Pierre et Marie Curie, Paris, 2006, Chapitre VI.

4. K. Rahmouni, S. Joiret, L. Robbiola, A. Srhiri, H. Takenouti, V. Vivier, Proc. Internat. Workshop „Advanced Techniques for Energy Sources Investigation and Testing", 4-9 Sept. 2004, Sofia, Bulgaria, P8-1.

5. L. Robbiola, J.M. Blengino, C. Fiaud, Corr. Sci. 40 (12), (1998), 2083.

6. L. Ying, F. Haitao, Z. Yifan, W. Wuji, J. Mat. Sci., 38 (2003) 407.

7. R. Faltenmeier, SSCR Journal 9, (1998), 1.

STUDIA UNIVERSITATIS BABEŞ-BOLYAI, CHEMIA, LII, 2, 2007

SIMULATION OF THE ROTARY LIMEKILN AND LIME COOLER

ANA-MARIA CORMOS*, VASILE-MIRCEA CRISTEA*, CALIN-CRISTIAN CORMOS*, SERBAN-PAUL AGACHI*

ABSTRACT. A mathematical model of the calcium carbonate decomposition process has been developed in order to determine the time and space evolution of temperature, solid and gaseous products distribution in the rotary limekiln.

The model incorporates a detailed mathematical description for the two phases (gas and solid) present into the system, also taking into account the heat transfer through the kiln wall. The gas phase, solid phase and kiln wall have been modeled using mass and heat balance equations for counter-current flow systems. Both time and spatial distribution for gaseous and solid components are described revealing the interactions between different subsystems considered in the study.

1. INTRODUCTION

The thermal decomposition of limestone is a very important process. In 2006, 271000 thousand metric tones of lime were produced in the entire world [1]. Lime, the main product of limestone thermal decomposition process, is a basic chemical; practically the lime is used in every human activity domain. The breakdown of consumption by major end-users was as follows: 36 % for metallurgical use, 27 % for environmental use, 24 % for chemical and industrial use and 13 % for construction use.

The decrease of energy consumption and efficient use of raw materials for the decomposition process of the limestone in a limekiln leads to important economic benefits (it decreases the operational costs; it increases the gross margin of the process; it makes lime manufacture processes more sustainable etc.).

* Babes – Bolyai University, Faculty of Chemistry and Chemical Engineering, 11 Arany Janos Street, RO-400028, Cluj – Napoca, Romania, Tel: +40264593833, Fax: +40264590818, E-mail: cani@chem.ubbcluj.ro

2. MATHEMATICAL MODEL OF ROTARY LIME KILN

The rotary limekiln consists of a cylindrical shell with its long axis having a small inclination from the horizontal direction. Calcium carbonate is introduced at the highest end of the shell and moves towards the lower end due to the rotation and the inclination of the cylinder. In the lower end of the kiln, a natural gas flux is burning in order to produce the heat necessary for the endothermic reaction (calcium carbonate decomposition)

The rotary limekiln with a gas heat recovery is presented in figure 1.

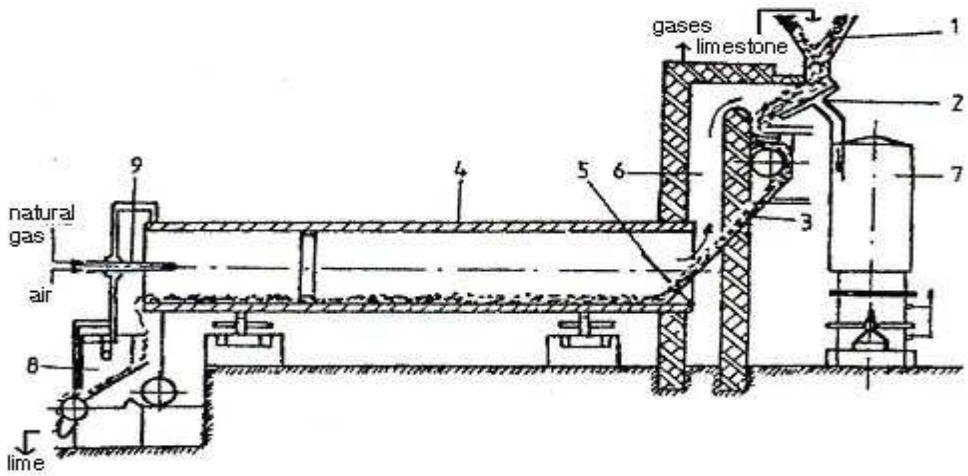

Figure 1. Rotary limekiln with a gas recovery system [2]
1 – calcium carbonate tank, 2 – grid, 3 – feed chute , 4 – rotary limekiln, 5 – cross wall , 6 – gas tower, 7 - scrubber , 8 – lime cooler, 9 – gas burner

Three zones can be distinguished along the kiln in the direction of the movement of the solid material. The first zone starts at the calcium carbonate feed and is the solid heating zone. The second zone is the reaction zone where most of the decomposition process is taking place. The last one is the combustion zone where the fuel flame is developed.

The produced lime is cooled with primary cool air in a lime cooler, figure 2.

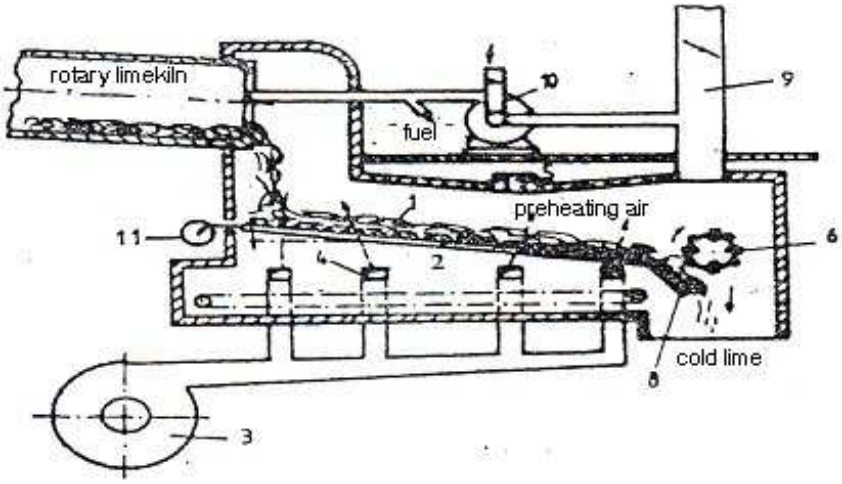

Figure 2. Lime cooler [2]
1 – grid, 2 – bars , 3 – ventilator , 4 – air distributor, 5 – connection , 6 – disintegrator with hammers, 7 – conveyer, 8 – lime outlet, 9 – secondary chimney, 10 – primary air ventilator, 11 – engine

The following assumptions have been considered for model development:

- Model parameters are constant in the radial cross section of the kiln;
- Both gas and solids velocity is considered constant.
- Limestone is uniformly distributed across the kiln section;
- Flowing regime is ideal for both phases (plug flow);
- Heat transfer by conduction and radiation are negligible in the axial direction;
- Coefficients of convection, emissivities, latent heat and heat of reaction are independent of temperature.

Heating zone:

The mass balance for solid and gas flows is described by the equations:

$$\frac{1}{V_m}\cdot\frac{\partial}{\partial t}\left(Q_m\right)=-\frac{\partial}{\partial z}\left(Q_m\right)-\frac{h_t\cdot A_T\cdot\left(T_g-T_m\right)}{L_v\cdot\left(0.1\cdot Q_m\right)}\cdot Q_h$$

$$\frac{1}{V_g}\cdot\frac{\partial}{\partial t}\left(Q_g\right)=-\frac{\partial}{\partial z}\left(Q_g\right)+\frac{h_t\cdot A_T\cdot\left(T_g-T_m\right)}{L_v\cdot\left(0.1\cdot Q_m\right)}\cdot Q_h$$

The heat balance equations for gas, solid and kiln wall are presented in the following equations:

$$\frac{Q_g \cdot C_g}{V_g} \cdot \frac{\partial}{\partial t}(T_g) = -Q_g \cdot C_g \cdot \frac{\partial}{\partial z}(T_g) - H_{gm} - H_{gp}$$

$$\frac{Q_m \cdot C_m}{V_m} \cdot \frac{\partial}{\partial t}(T_m) = -Q_m \cdot C_m \cdot \frac{\partial}{\partial z}(T_m) + H_{gm} - H_{pm}$$

$$M_p \cdot C_p \cdot \frac{\partial}{\partial t}(T_p) = H_{gp} + H_{pm} - H_{p0}$$

Reaction zone (calcium carbonate decomposition):

The mass balance equations for the gaseous and solid productions are:

$$\frac{1}{V_g} \cdot \frac{\partial Q_g}{\partial t} = -\frac{\partial Q_g}{\partial z} + \frac{Q_m}{V_m} x_{CaCO_3} k_{CaCO_3} \frac{M_{CO_2}}{M_{CaCO_3}}$$

$$\frac{1}{V_m} \cdot \frac{\partial Q_m}{\partial t} = -\frac{\partial Q_m}{\partial z} - \frac{Q_m}{V_m} x_{CaCO_3} k_{CaCO_3} \frac{M_{CO_2}}{M_{CaCO_3}}$$

The kinetics of calcium carbonate decomposition reaction is considered to follow Arrhenius' law.

The mass balance equations for calcium carbonate contained in solid is:

$$\frac{1}{V_m} \cdot \frac{\partial x_{CaCO_3}}{\partial t} = -\frac{\partial x_{CaCO_3}}{\partial z} - \frac{1}{V_m} x_{CaCO_3} k_{CaCO_3}$$

The heat balance equations for gas, solid and kiln wall are presented in the following equations:

$$\frac{Q_g c_g}{V_g} \cdot \frac{\partial T_g}{\partial t} = -Q_g c_g \frac{\partial T_g}{\partial z} - H_{gm} - H_{gp}$$

$$\frac{Q_m c_m}{V_m}\cdot\frac{\partial T_m}{\partial t}=-Q_m c_m\frac{\partial T_m}{\partial z}+\frac{Q_m}{V_m}x_{CaCO_3}k_{CaCO_3}\Delta H_{CaCO_3}+H_{gm}-H_{pm}$$

$$M_p\cdot C_p\cdot\frac{\partial T_p}{\partial t}=H_{gp}+H_{pm}-H_{p0}$$

Flame zone:

The heat balance equations for gas, solid, flame and kiln wall are:

$$\frac{Q_g\cdot C_g}{V_g}\cdot\frac{\partial}{\partial t}\left(T_g\right)=-Q_g\cdot C_g\cdot\frac{\partial}{\partial z}\left(T_g\right)+H_{fg}-H_{gm}-H_{gp}$$

$$\frac{Q_m\cdot C_m}{V_m}\cdot\frac{\partial}{\partial t}\left(T_m\right)=-Q_m\cdot C_m\cdot\frac{\partial}{\partial z}\left(T_m\right)+H_{gm}+H_{pm}+H_{fm}$$

$$\frac{Q_c\cdot C_c}{V_g}\cdot\frac{\partial}{\partial t}\left(T_f\right)=-Q_c\cdot C_c\cdot\frac{\partial}{\partial z}\left(T_f\right)-H_{fp}-H_{fm}-H_{fg}$$

$$M_p\cdot C_p\cdot\frac{\partial}{\partial t}\left(T_p\right)=H_{gp}-H_{pm}-H_{p0}$$

The heat fluxes considered in the above equations are:
- heat flux to the environmental

$$H_{p0}=h_0\cdot\pi\cdot D\cdot\left(T_p-T_0\right)+\sigma\cdot\pi\cdot D\cdot e_{p\cdot}\cdot\left({T_p}^4-{T_0}^4\right)$$

The heat fluxes H_{gm} (gas to solid), H_{gp} (gas to kiln wall), H_{pm} (kiln wall to solid) are different for each zone:

- heat zone (and lime cooler)
-

$$H_{gm}=h_g\cdot L_2\cdot\left(T_g-T_m\right)+\sigma\cdot L_2\cdot e_m\cdot e_g\cdot\left({T_g}^4-{T_m}^4\right)$$

$$H_{gp}=h_g\cdot L_3\cdot\left(T_g-T_p\right)+\sigma\cdot L_3\cdot e_p\cdot e_g\cdot\left({T_g}^4-{T_p}^4\right)$$

$$H_{pm}=h_p\cdot L_1\cdot\left(T_p-T_m\right)+\sigma\cdot L_2\cdot e_p\cdot\left(1-e_g\right)\cdot e_m\cdot\left({T_p}^4-{T_m}^4\right)$$

- reaction zone

$$H_{gm} = U \cdot A_T \cdot \left(T_g - T_m\right)$$

$$H_{gp} = h_g \cdot L_3 \cdot \left(T_g - T_p\right) + \sigma \cdot L_3 \cdot e_p \cdot e_g \cdot \left({T_g}^4 - {T_p}^4\right)$$

$$H_{pm} = h_p \cdot L_1 \cdot \left(T_p - T_m\right)$$

- flame zone

The fluxes H_{fm} (flame to solid), H_{fp} (flame to kiln wall), H_{fp} (flame to kiln wall) are:

$$H_{fm} = \sigma \cdot L_2 \cdot e_f \cdot e_m \cdot \left(1 - e_g\right) \cdot F_{fm} \cdot \left({T_f}^4 - {T_m}^4\right)$$

$$H_{fp} = \sigma \cdot L_3 \cdot e_f \cdot e_p \cdot \left(1 - e_g\right) \cdot F_{fp} \cdot \left({T_f}^4 - {T_p}^4\right)$$

$$H_{fg} = \sigma \cdot \pi \cdot D_f \cdot e_{f\cdot} \cdot e_g \cdot \left({T_f}^4 - {T_g}^4\right) + h_f \cdot \pi \cdot D_f \cdot \left(T_f - T_g\right) - \frac{\partial Q_c}{\partial l} \cdot C_c \cdot T_f$$

Lime cooler:

In the cooler, only heat phenomena (heat transfer and transport) takes place. The heat balance equations for gas, solid and kiln wall are presented in the following equations:

$$\frac{Q_g \cdot C_g}{V_g} \cdot \frac{\partial}{\partial t}\left(T_g\right) = -Q_g \cdot C_g \cdot \frac{\partial}{\partial z}\left(T_g\right) + H_{gm} - H_{gp}$$

$$\frac{Q_m \cdot C_m}{V_m} \cdot \frac{\partial}{\partial t}\left(T_m\right) = -Q_m \cdot C_m \cdot \frac{\partial}{\partial z}\left(T_m\right) - H_{gm} - H_{pm}$$

$$M_p \cdot C_p \cdot \frac{\partial}{\partial t}\left(T_p\right) = H_{gp} + H_{pm} - H_{p0}$$

The simulation of the calcium carbonate decomposition process was done using Matlab software package.

3. RESULTS AND DISCUSSIONS

The simulation based on the mathematical model of the calcium carbonate decomposition process reveals the time and space evolution of temperature, flows, solid and gaseous products in the rotary kiln.

Some of the most representative simulation results are presented in the figures below. The solid is the principal raw material of the process and consequently, in the figures below the bench mark "0" is the calcium carbonate feed end of the rotary kiln.

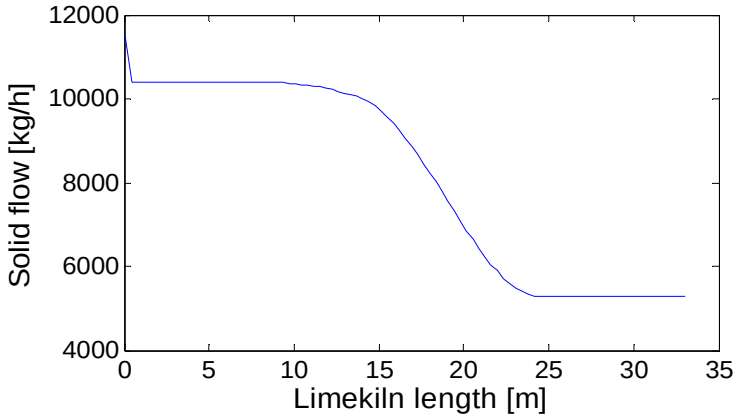

Figure 3. Solid flow profile

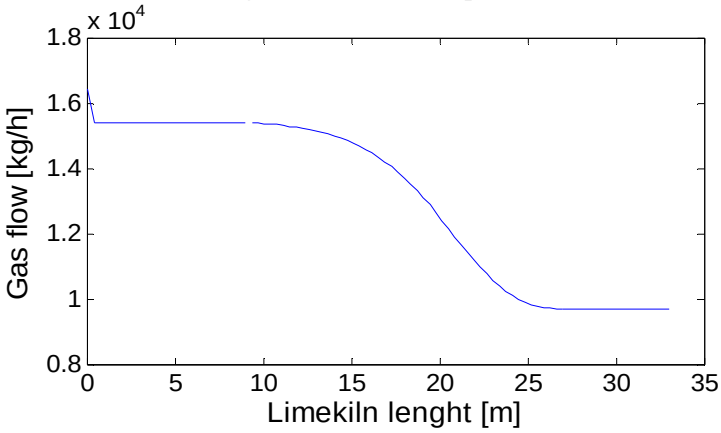

Figure 4. Gas flow profile

In the figures, 3 and 4 are presented the solid and gas flow profiles along the kiln length. The flows are almost constant in the heating zone,

because in this zone only physical processes occur (heat transfer between solid and gaseous phase and limekiln wall) without mass transfers between the phases presented in the kiln. Exception is in the first part of the heating zone, when the drying of solid takes place.

The calcium carbonate content of the solid decreases along the reaction zone, reaching a value less than 4% at the discharge end, figure 5.

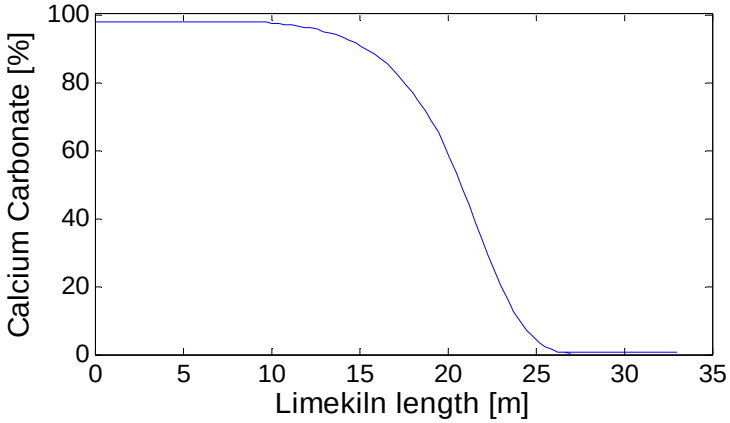

Figure 5. Calcium carbonate content profile

The lime T_m, gas T_g and inside kiln wall T_p temperatures profiles, for the lime cooler are presented in the figure 6.

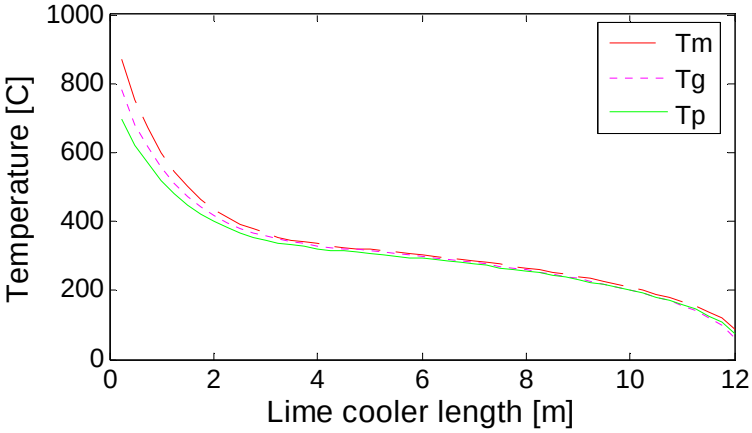

Figure 6. Lime temperature profile

The answer of the rotary kiln system was also investigated in the presence of typical disturbances. If one or more input variables are changed, the system behavior is modified to reach other stationary state (the outputs parameters of the system are changed). For example, if the solid flow rate Q_m increase with a step + 1000 Kg/h at the solid feed end, the gas flow increase with 600 kg/h at out gas kiln end. The gas flow change is presented in figure 7.

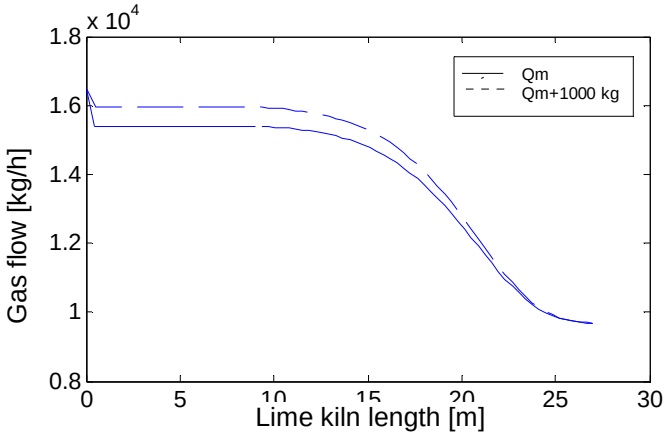

Figure 7. The gas flow change for a step increase of solid flow (Q_m + 1000 Kg/h)

The lime cooler system was also investigated. The change of the lime temperature for a step increase of the cooling air flow ΔQ_g = + 10% is presented in figure 8.

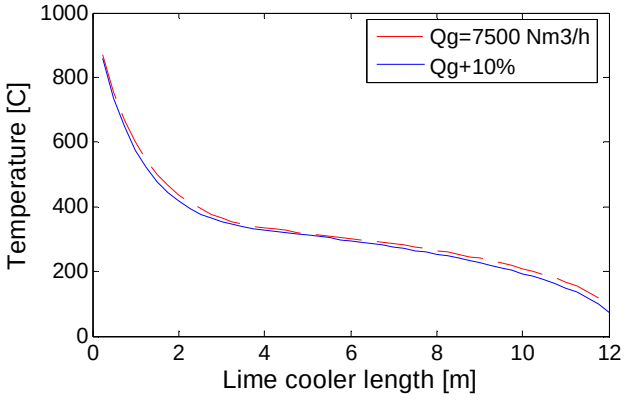

Figure 8. The lime temperature change for a step increase of natural gas flow rate of ΔQ_g =+ 10%

The simulations reveal the way that disturbances influence some important process variables and their evolution along the rotary lime kiln.

4. CONCLUSIONS

The simulation of the rotary lime kiln and lime cooler was done using MATLAB software. The time and space evolution of the main process variables (solid and gaseous flows, composition of the streams, temperature of the solid and gaseous phases) have been studied considering their complex interactions taking place during the limestone decomposition process.

The simulator based on the mathematical model and of the calcium carbonate decomposition process can be used to study the behavior of the process in changing operating conditions and the influence of different disturbances. The process simulation results can be very useful to establish the optimal operation conditions and to design the control system for the plant.

5. . NOTATION

A_T – specific area of solid exposed to gas, [m²/m]
Cc , Cg , Cm , Cv , Cp - specific heat for combustion products, gas, solid, vapors and kiln wall [kcal/(kg·K)]
D, D_f – diameter of the limekiln and the flame, [m]
E_a – Activation Energy, [kcal/kmol]
e_f, e_g, e_p, e_m – emissivities of the flame, gas, kiln wall and solid
F_{fm}, F_{fp} – form factors for radiative heat transfer
h_f, h_g, h_p, h_m, h_0 – heat transfer coefficients, [kcal/(h·m²·K)]
K_T – heat transfer coefficients from gas to solid, [kcal/(h·m²·K)]
k_{CaCO3} – velocity constant of the calcium carbonate decomposition reaction, [1/h]
ΔH_{CaCO3} – heat of reaction, [kcal/kg]
M_{CaCO3} – molecular mass of calcium carbonate, [kg/kmol]
M_p – mass per unit length of the kiln wall, [kg/m]
Q_g, Q_m , Q_h – flowrate of gas, solid, moisture [kg/h]
T_g, T_m, T_p, T_f, T_0 – temperature of the gas, solid, kiln wall, flame and enviroment, [K]
V_g, V_m - gas and solids velocity, [m/h]
R – gas constant, [kcal/(kmol·K)]
U – heat transfer coefficient for the reaction zone, [kcal/(h·m·K)]
X_{CaCO3} – calcium carbonate concentration, [mass %]
σ - Stefan-Boltzmann constant, [kcal/(h·m²·K⁴)]

REFERENCES

1. Cormos A. M. – Modelarea si simularea procesului de descompunere a calcarului intr-un cuptor vertical, cu cocs, Teză de doctorat , Cluj-Napoca, 2005

2. Cristea V. M., Agachi S. P., Control of an Industrial Rotary Calciner for Soda Ash Production, Proceeding of ESCAPE-12 Congress, Hague, The Netherlands, 463-468, 2002

3. http://minerals.usgs.gov/minerals/pubs/commodity/lime - Miller, M. Lime Information, US Geological Survey Minerals Yearbook, 2006

4. Le Blanc G. D., Seborg D. E., Holman K. L., Physically-Based, Dynamic Model of a Lime Kiln, AIChE Annual Meeting, Los Angeles, 18 November, 1997

5. Szep Al, Varul: Tehnologie şi utilizări, Ed. Cermi, Iaşi, 2005

STUDIA UNIVERSITATIS BABEŞ-BOLYAI, CHEMIA, LII, 2, 2007

MODEL PREDICTIVE CONTROL (LINEAR AND NONLINEAR) OF A COMPLEX FCCU

RALUCA ROMAN*, ZOLTAN KALMAN NAGY, VASILE MIRCEA CRISTEA*, ŞERBAN PAUL AGACHI***

ABSTRACT. Model Predictive Control (MPC) is standard multivariable control solution in the continuous process industries and it is becoming increasingly popular in the petrochemical industry due to the large economical benefits. The paper present the most important modern process control strategies using industrial relevant complex Fluid Catalytic Cracking process as the subject of control performance studies. The nonlinear and linear MPC methods have been investigated and the results demonstrate that modern MPC approached can be successfully applied for complex chemical processes.

1. INTRODUCTION

Petroleum refineries are complex plants, where the combination and sequence of processes is usually specific to the characteristics of the crude oil (raw material) and the products to be produced. A number of different catalytic cracking processes have evolved in order to increase the degree of conversion and improve product quality. The most important are hydrocracking and fluid catalytic cracking. Fluid Catalytic Cracking Unit (FCCU) is one of the most important conversion processes in a petroleum refinery; during the process, high-boiling petroleum fractions (gasoil) are converted in valuable products: gasoline and diesel and valuable gases (ethylene, propylene, isobutylene) are also produced [1].

The process is presented in Figure 1.

* Babeş-Bolyai University, Faculty of Chemistry and Chemical Engineering, 11 Arany Janos., Cluj-Napoca, 400028 Cluj-Napoca, Romania, e-mail: romanr@chem.ubbcluj.ro

** Loughborough University, Department of Chemical Engineering, Loughborough, LE11 3TU, United Kingdom

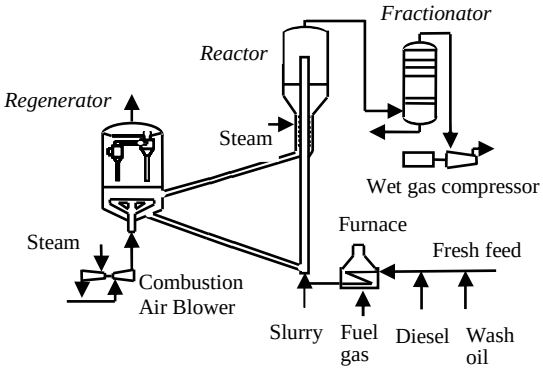

Figure 1. Fluid Catalytic Cracking Unit

The process consists in the following: pre-heated feed is mixed with the hot slurry recycle (from the bottom of the main fractionator) and injected into the reactor riser, where it mixes with hot regenerated catalyst and totally vaporizes. A carbonaceous material (coke) is deposited on the surface of the catalyst and poisons the catalyst, continuous regeneration is made in regenerator. Spent catalyst is transported from the reactor to the regenerator. Catalyst in the regenerator is fluidized, carbon and hydrogen on the catalyst react with oxygen to produce gases such as CO, CO_2, H_2O. Gas travels up in the regenerator into the cyclones where the entrained catalyst is removed and returned into the bed Reactor products (gas, gasoline, diesel, slurry) are passed to the main fractionator for separation [2].

A control system is used to maintain the stable operation of a process, to reduce variability in the product specification, to protect the physical and operational constraints or to maintain a maximum operating efficiency. The development in process control is influenced by the improvement of the performance of computers suitable for on-line control. The process computer having high speed and storage capacity can be easily needed in controlling the processes due to its low capitol costs [3]. The petroleum refining industry is one of the world leaders in application of advanced control methods and the FCCU became in the last decades the testing bench for every modern refinery control system. Researchers, but also people from industry, are interested in developing control algorithms and their efficient FCC implementation due to the large economic benefits.

2. MODEL PREDICTIVE CONTROL ALGORITHM

Model Predictive Control (MPC) algorithm has become a standard multivariable control solution in the continuous process industries, and it is becoming increasingly popular in the petrochemical industry. The main reasons for this preference include the ability to handle constraints in an optimal way and the flexible formulation in the time domain. Linear MPC schemes, (MPC schemes for which the prediction is based on a linear description of the plant) and nonlinear MPC schemes (MPC based on a nonlinear plant description) has been studied intensely in the past decade and the number of reported industrial applications is continuously growing.

Model Predictive Control (MPC) is a form of control in which the current control action is obtained by solving on-line, at each sampling instant, a finite horizon open loop optimal control problem, using the current state of the plant as the initial state; the optimization yields an optimal control sequence and the first control in this sequence is applied to the plant- this is its main difference from conventional control which uses a pre-computed control law. The optimization problem is solved on-line based on prediction obtained from a nonlinear or linear model of the plant [4].

The algorithm is presented in Figure 2.

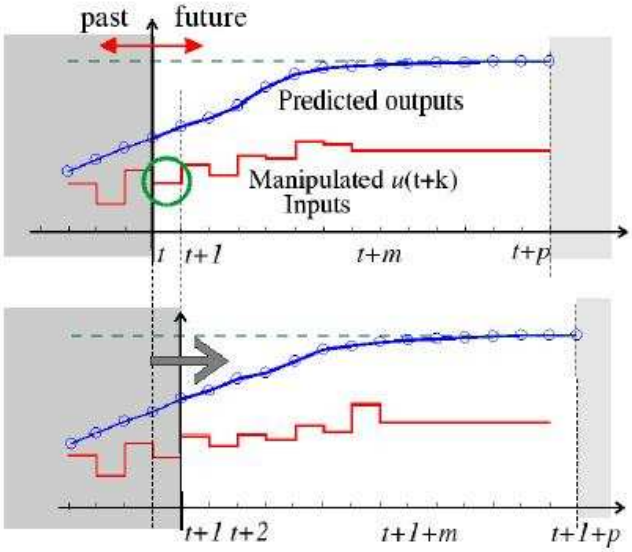

Figure 2. MPC algorithm

At the present time k the behavior of the process over a horizon p is considered. Using the model, the response of the process output to changes in the manipulated variable is predicted. Current and future moves of the manipulated variables are selected such that the predicted response has certain desirable (or optimal) characteristics. The first control action is implemented, new measurements are obtained which are used for the compensation of plant/model mismatch and the estimation of unmeasured state variables. Finally the prediction horizon is shifted by one sampling time into the future and the optimization is performed again

The mathematical formulation of the model predictive control problem is [5,6]:

- *objective function*:

$$\min_{u(.),P,M} \{J(x(t),u(.),P,M)\} \tag{1}$$

- *constraints:*

$$\frac{\partial x}{\partial t} = f(f,u,q,d) \tag{2}$$

$$x(k) = x_{est}(k) \tag{3}$$

$$0 = g_1(x) \tag{4}$$

$$y_p = g_2(x) \tag{5}$$

$$u_{\min}(k+i) \le u(k+i) \le u_{\max}(k+i) \tag{6}$$

$$u(k+i) = u(k+M-1) \tag{7}$$

$$x_{min}(k+i) \le x(k+i) \le x_{max}(k+i) \tag{8}$$

$$y_{\min}(k+i) \le y_P(k+i) \le y_{\max}(k+i) \tag{9}$$

where x are state variables, u are manipulated variables, q are parameters, d are measured and unmeasured disturbances and y are output variables.

The objective function is the sum of the squares of the differences between the predicted outputs and the setpoint values over the prediction horizon of P time steps and it has a second term, which is the square sum of manipulated variable changes over the control horizon (M)::

$$\min_{u(k)\ldots u(k+M-1)} \{\sum_{i=1}^{P} \| Q_i(r(k+i) - y_P(k+1)) \|^2 + \sum_{i=1}^{M} \| R_i \Delta u(k+i-1) \|^2 + \sum_{i=1}^{M} \| R_{uss} \Delta u(k+i-1) - u^{ref}(k+i-1)) \|^2 \} \tag{10}$$

3. FCCU control results

Traditional control theory is no longer suitable for the FCCU increasingly sophisticated operating conditions and product specifications. There is now a strong demand for advanced control strategies with higher control quality to meet the challenges imposed by the growing technological and market competition.

The FCCU dynamic model for which MPC studies has been done was developed on the basis of reference construction and operation data from an industrial unit (ROMPETROL Company) and consists of detailed models of the feed and preheat system, reactor stripper, riser, regenerator, air blower, wet gas compressor, catalyst circulation lines and main fractionator. The model captures the major dynamic effects that can occur in an actual FCCU system. It is multivariable, strongly interacting and highly nonlinear (it consist of 933 differential algebraic equatios (ODEs) and more than 100 algebraic equations).

Linear Model Predictive Control (LMPC) and Nonlinear Model Predictive Control (NMPC) algorithms based on the global reactor-regenerator-main fractionator FCCU are presented in a complex 5x7 structure control; it was investigated the most important process variables: reactor temperature (T_r), fractionator pressure (P_5), reactor catalyst inventory (W_r) and gasoline and diesel composition in the top and bottom of the main fractionator. The control of those variables is important in the efficient and safe operation of the unit and also influences the products quality and plant productivity. As manipulated variables where chose form a practical point of view: the spent and regenerated catalyst circulation lines valve positions (*svsc* and *svrgc*), stack valve position (V_{14}), condenser's liquid flow *(LT)* and reboiler's liquid flow *(VB)*.

Comparisons of the MPC based nonlinear model (NMPC) with the MPC based linear FCCU model (LMPC) in the presence of coking rate disturbance (1% increase at t=8 min) are presented in the Figure 3 and Figure 4. This disturbance shows the effect of changes in raw material properties on the process variables.

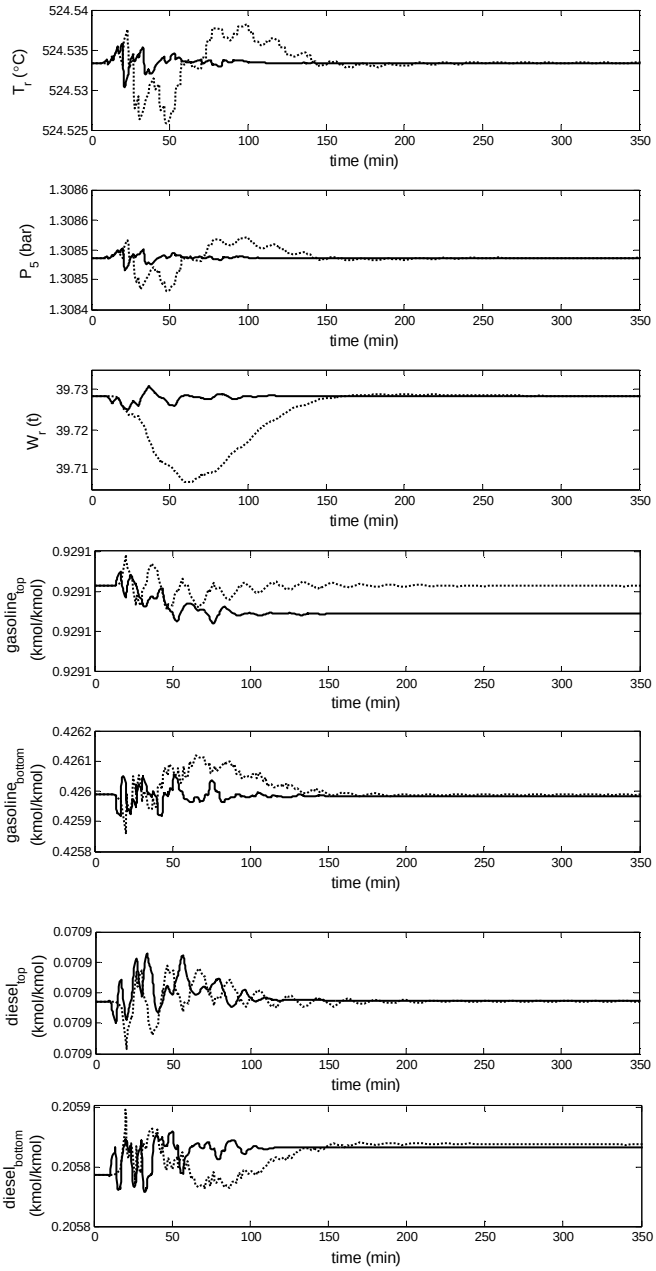

Figure 3. Simulation of FCCU dynamic behavior-controlled variables (LMPC - dotted line; NMPC - solid line)

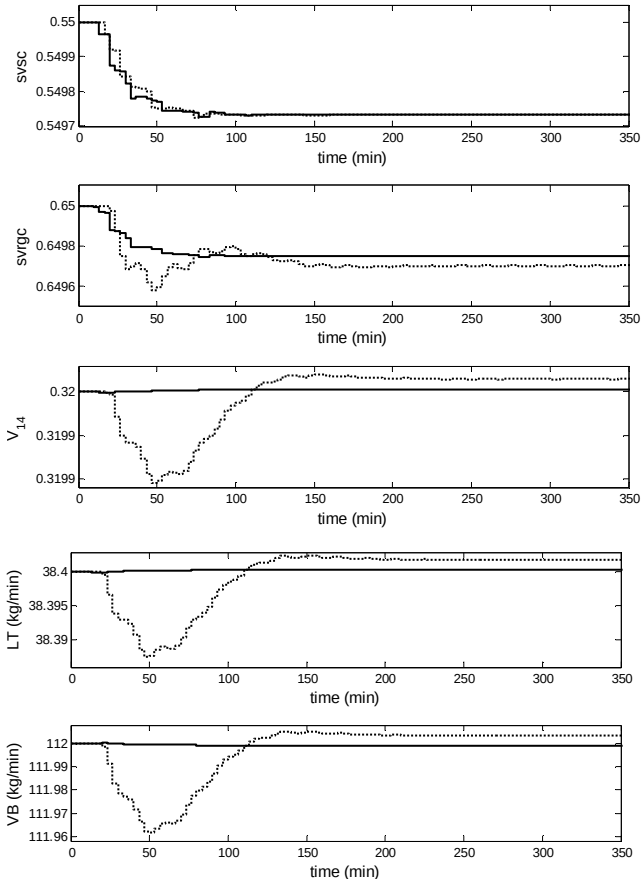

Figure 4. Simulation of FCCU dynamic behavior-manipulated variables (LMPC - dotted line; NMPC - solid line)

4. CONCLUSIONS

Modern control studies have been done for a complex petrochemical process: Fluid Catalytic Cracking Unit. It is shown that complex MPC structures based linear and nonlinear model can successfully be applied for a very height dimensional FCC system. MPC it was successfully applied and present good control performance for complex FCCU based on its multivariable feature, inherent prediction ability and capacity to direct handle the constraints and this fact has made it an important tool for the control engineer. NMPC algorithms performs better than LMPC algorithm

in tracking the setpoints and rejecting disturbances The results of the proposed complex control structures encourage the application of the advanced control algorithms to the industrial FCCU.

ACKNOWLEDGEMENTS

The authors are also gratefully to the ROMPETROL Company for their support. This work was supported by the Marie Curie fellowship HPMT-CT-2001-00278.

REFERENCES

1. F. Allgoewer, T. A. Badgwell, J. S. Quin, J. B. Rawlings, S. J. Wright, *Advances in Control*, **1999**, 391-400.
2. R. Findeisen, L. Imsland, F. Allgoewer, B. A. Foss, *European Journal of Control*, **2003**, *9*, 179-195.
3. R. Sadeghbeigi, "Fluid Catalytic Cracking Handbook", Buterworth-Heinemann, New York, **2000**.
4. R. C. McFarlane, R. C. Rieneman, J. F. Bartee, C. Georgakis, *Computers Chemical Engineering*, **1993**, *17*, 275-300.
5. S. P. Agachi, Z. K. Nagy, M. V. Cristea, A. Imre-Lucaci,, Wiley-VCH Verlag GmbH and Co. KGaA, **2006**.
6. S.J Qin, T. Badgewell, *Control Engineering Practice*, **2003**, *11*, 733-764.

STUDIA UNIVERSITATIS BABEŞ-BOLYAI, CHEMIA, LII, 2, 2007

DETERMINATION OF CADMIUM IN ENVIRONMENTAL SAMPLES USING THE METHANE - AIR FLAME ATOMIC ABSORPTION SPECTROMETRY

LADISLAU KÉKEDY-NAGY*, JÓZSEF SZŰCS-BALÁZS*

ABSTRACT. The cadmium content of some soil, tree leave, grape and lichens samples has been determined directly by flame atomic absorption spectrometry using the methane-air flame. The flame and instrumental parameters were optimized; the best results were obtained with the lamp current of 5 mA, at the observation height of 11 mm, with the stoichiometric flame. The detection limit of 0.05 ± 0.02 $mg.L^{-1}$ was obtained at a significance level of 0.05. The cadmium content of environmental samples has been determined with the external calibration curve and the standard addition method. In all cases, the results of two methods agree within the quantification error.

INTRODUCTION

Cadmium is relatively rare element; its abundance in the lithosphere is estimated at about 0.5 $mg.kg^{-1}$ in the earth's crust. Due its several attractive physical and chemical properties cadmium is largely used in the industry. The major use of cadmium is for plating, mainly iron and steel articles, to form a protective coating. Cadmium is used in many alloys too, such as bearing metals, solders, electrical conductor, fusible metals and jewelry. The main sources of cadmium pollution are the ferrous metal and steel production, industrial Cd applications and nonferrous metals mining and production. Cadmium lands on environment via air deposition, sludge application and, in unusual conditions, via liquid effluents and solid wastes from Cd-processing plants. It can enter the human body mainly via drinking water, plants and animal food products, respectively. The quantity of cadmium in these products is proportional to the cadmium loading of the environment (natural water and soil especially) [1-3]. Cadmium has no physiological importance but it is considered as one of the most poisonous heavy metal for all living

* Universitatea "Babeş-Bolyai" Facultatea de Chimie şi Inginerie Chimică, 3400 Cluj-Napoca, Arany J. 11, România

organisms. In the plants, among other effects, inhibits the photosynthesis, the activity of some enzyme activity, as H+-ATPase etc.[4-7]. Entering the animal or human organism by ingestion cadmium causes immediate poisoning and irreversible damage to the liver and the kidneys [8,9]. As calcium, magnesium and zinc antagonist chronic cadmium poisoning can leads to osteomalacia and osteoporosis in humans, called the Itai-Itai disease (occurred first in Japan in 1912, latest in '70-es) [10]. Cadmium can produce sterility, exhibits carcinogenic and teratogenic effects too. Therefore, accurate and reliable control of the whole cadmium content in different samples is required.

Flame atomic absorption spectrometry (FAAS) is probably the most widespread analytical method for the determination of cadmium in low concentrations. Usually the high temperature C_2H_2-air, C_2H_2–N_2O flames are used as atomization source, the detection limit of the cadmium by direct aspiration being of order of 10^{-3} -10^{-4} mg.L^{-1} [11, 12]. Cadmium is present usually in trace levels in the environment, in some cases the analyte had to be concentrated prior the quantification, as by: on-line sorption [13]; solid phase extraction on different adsorbents such as: Amberlite XAD-2010 resin [14]; Amberlite XAD-2 resin loaded with TAM reagent [15]; cellulose nitrate membrane filter [16]; bonded silica gel [17-20].

The low temperature (~ 2000 K) propane-butane-air (PB-A) flame was used in few cases for the determination of cadmium, mostly in early stage of the flame atomic absorption spectrometry development. The methane-air (M-A) flame has similar properties (temperature, burning velocity etc) with the PB-A flame [21]. To our best knowledge the behaviour of cadmium in the M-A flame was not studied, and the detection limits are not known.

The aim of the present work is to optimize the flame and the instrumental parameters for the AAS determination of Cd in the M-A flame, to apply the results for quantification of Cd in different environmental samples by direct aspiration without sample concentration prior analysis.

EXPERIMENTAL

INSTRUMENTATION

The measurements were carried out at 228.1 nm with a single beam HEATH-701 (Heath Co., Benton Harbor, MI, USA) spectrometer. A cadmium hollow-cathode lamp was used (NARVA, Germany), in connection with a HEATH EU-700 scanning monochromator, a HEATH EU-700-30 type photomultiplier module and a 1P28A (RCA, USA) photomultiplier (-360 V). The photomultiplier signal was introduced via a home made I/U and A/D

converter (National Instruments) into a Pentium 2 PC and processed using in Quick Basic language written software. The data acquisition speed was of 100 ms, one recorded data represents the mean value of 50 measuring points, each point being the average of 300 individual measurements. The pneumatic nebulizer-spray chamber-burner system was used from an AAS-1 (Carl Zeiss Jena) atomic absorption spectrometer. The original slot type burner-head (for C_2H_2-air flame) was replaced with a similar, Mecker type, developed by us for atomic absorption measurements in the M-A flame [22]. The air flow-rate was kept constant, 500 L/h, the flow rate of the methane being varied as a function of the gas mixture wanted. As CH_4 source the city gas of 99 % purity was used, from the pipe.

CHEMICALS

The cadmium stock standard solution (1000 $mg.L^{-1}$) was prepared by dissolving in HCl (analytical grade, Merck, Darmstadt, Germany) of 1 g of metal (Specpure, Johson Matthey Chemicals Limited, England). The diluted standards were prepared by dilution with double distilled water.

SAMPLING AND HANDLING

The top soils were collected in 5-10 cm depth, the vegetal organic matter was removed (roots, leaves, boughs etc.), dried in oven at 105 °C, grinded and sieved. 2 grams of samples were taken for analyses. The samples were treated with 10 mL of concentrated HCl and heated carefully on hot plate for 30 minutes. Then 1 mL of concentrated HNO_3 was added and heated for further 5 minutes, and filtered. The clear filtrate was completed to a volume of 50 mL. The tree leaves (*Juglans regia, Prunus domestica, Vitis vinifera)* were collected in July after two weeks of dry season. The leaves were dried first at room temperature than in the drying oven at 90 °C. Lichen samples (*Xantoria parietina*) were collected from the cortex of trees by cutting with a sharp knife. After removal the rest of cortex, the lichens were dried in oven at 90 °C. The dry samples were finely grinded, about 2 g were taken for analysis. The samples were digested by treating with 10 mL of concentrated HNO_3, allowed to stand overnight, and heated carefully on hot plate until the production of red NO_2 fumes ceased. After cooling 2 mL of 70% $HClO_4$ were added and heated again to allow evaporating to a small volume. Finally, the clear digests were diluted to a volume of 50-mL with distilled water. The grapes sap was collected in springtime during the pruning. The clear liquid drops were collected directly into the 5 mL vials and were kept in the refrigerator at 4 °C until analysis. The saps samples were used directly, without any treatment.

PROCEDURE

The behaviour of cadmium in the M-A flame was observed in the flame up to h = 16 mm over the burner head (in 1mm steps). Three different flame compositions were used: 0.88; 1.00 and 1.12, expressed in relative stoichiometric units (RSU). Four replicate measurements were made in each case. The mean, the standard deviation, the S/N was calculated for each h and flame composition investigated. The homogeneity of the means was tested by the F test at a significance level of 0.05. The spectral bandpass of the monochromator was of 0.1 nm (width of the slit of 0.050 mm).

RESULTS AND DISCUSSION

OPTIMIZATION OF THE FLAME AND INSTRUMENTAL PARAMETERS

First, the hollow-cathode lamp current was optimized, by measuring the absorption (A) of the calibration solution of 1 mg.L^{-1} Cd at different lamp current intensities (i), between 2 – 10 mA, in 1 mA steps. The composition of the flame was constant, of 1.12 RSU, the observation height over the burner (h) was of 9 mm. The results are summarized in the Table I.

Table I.

The i - A relationship for 1 mg.L^{-1} of Cd in the M-A flame

i (mA)	A	S/N ratio	RSD (%)
2	0.063	2.24	11.1
3	0.058	6.80	6.9
4	0.056	7.22	7.1
5	0.058	12.60	5.2
6	0.055	10.17	3.6
7	0.048	7.86	4.2
8	0.044	12.00	4.5
9	0.043	5.78	4.7
10	0.044	8.33	4.5

The absorption of cadmium is maximal at i = 2 mA and decreases non-uniformly with the increase of the lamp current. The A – i relationship could

be described best with a sixth order polynomial function. The curve presents a slow increase in the i = 4 – 6 mA range with the local maximum at the i = 5 mA. At this lamp current value the S/N ratio of the determinations is also maximal, of 12.6 (RSD = 3.44%). We can consider that the optimal value of the lamp current for the determination of cadmium is of 5 mA.

Further, the influence of the flame composition and that of the observation height on the absorption of cadmium was investigated. Three flame compositions (0.88, 1.00, 1.12 RSU) were used, the concentration of the analyte was 1 mg.L^{-1}. The lamp current was the optimal one. The absorption data versus observation height and flame composition are presented in the Fig. 2.

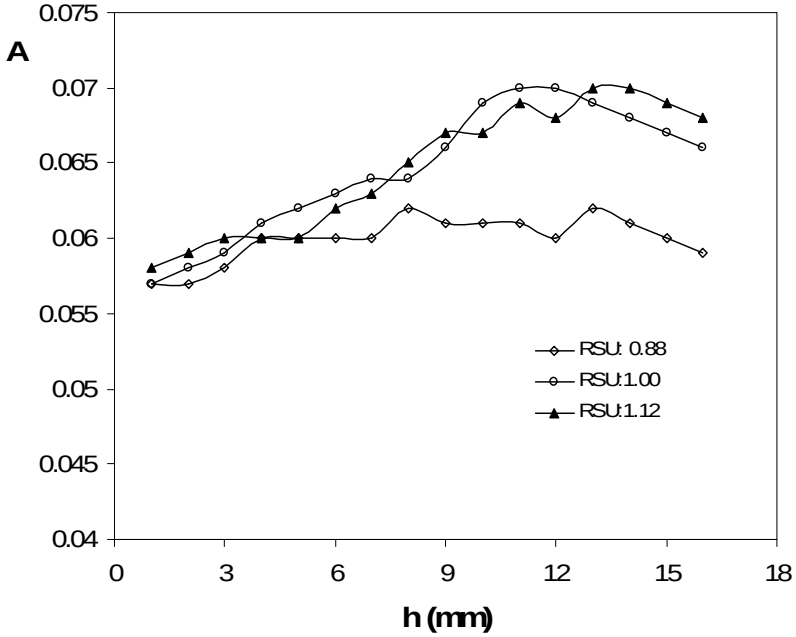

Figure 2. The variation of the absorption of the 1 mg.L^{-1} cadmium vs. observation height and flame composition.

The analytical signal depends both on observation height and flame composition. The absorption increases slowly with the increase of the methane content of the flame, being the highest in stoichiometric gas mixture (1.00 RSU). The highest absorption was observed at the same height of 11 mm over the burner, regardless of flame composition. The standard deviation of all

means was homogeneous, the magnitude of the S/N ratio being decided by the magnitude of the mean. In conclusion, the optimal conditions for the quantitative determination of cadmium in the M-A flame are h = 11 mm and flame composition of 1.00 RSU.

CALIBRATION, DETERMINATION OF THE DETECTION LIMIT

For the determination of the detection limit the variation of the analytical signal versus concentration was studied in the 0.01 – 50 $mg.L^{-1}$ cadmium concentration range. Three calibration curves were plotted. Each calibration curve was established by using six standard solutions. Six replicate measurements were made at each concentration level. The homogeneity of the means and the linearity of the calibration curve were tested. The equation of the regression line, the confidence limits and the coefficient of correlation (R) were calculated with the least squares method. The detection limit was calculated for the fixed values of (P10)0 = 0.025 and (P11)d = 0.975. The results are summarized in Table II.

Table II

Calibration data of cadmium determination in the M-A flame

No. Eq.	Concentration range ($mg.L^{-1}$)	Equation of the calibration curve	Detection limit ($mg.L^{-1}$)
1.	0.1 – 2	A = 0.064 *C – 0.0035 R = 0.9998	0.05 ± 0.02
2.	2 – 10	A = 0.0417*C + 0.0669 R = 0.9934	0.77 ± 0.36
3.	0.1 – 50	$A = 0.00001*C^3 – 0.0015*C^2 + 0.0627*C +$ + 0.0012 R = 0.9997	not calculated

The A – C relationship is not linear in the whole concentration range. The best fitted linear relationship was found in the 0.1 – 2 $mg.L^{-1}$ domain, the detection limit was of 0.05 ± 0.02 $mg.L^{-1}$. This value is low, but about two orders of magnitude higher than those obtained in the acetylene flames. In the 2 – 10 $mg.L^{-1}$ domain the A – C relationship is still linear, the detection limit being of same order of magnitude with that obtained earlier. Beyond 10 $mg.L^{-1}$ the calibration curve bents progressively toward the abscissa, exhibiting the well known saturation phenomenon. The A-C relationship for the entire 0.1 – 50 $mg.L^{-1}$ concentration range can be approximated best with a third order polynomial curve.

DETERMINATION OF CADMIUM IN THE ENVIRONMENTAL SAMPLES

The cadmium content of the samples was determined both by the calibration and by the standard addition method. The later method was used in order to study the presence of possible interference and/or as reference method due to the absence of certified reference material. The determinations were carried out with optimized flame and instrumental parameters. Four parallel measurements were made in each case. The measuring sample solutions were prepared in 25 ml volumetric flasks. In the case of standard addition method 50 µl of concentrated cadmium standard of 100 $mg.L^{-1}$ was added to the 1 mL of diluted sample. Three additions of standard were made, in 0.5 $mg.L^{-1}$ concentration steps. It was calculated the regression line, the cadmium content was determined from the intercept with the abscissa of the line. The results of the determination of cadmium content of the environmental samples are summarized in the Table III.

Table III

Results of analysis of the environmental samples (n = 4)

Sample		Concentration ($mg.kg^{-1}$, by standard calibration)	Concentration ($mg.kg^{-1}$, by standard addition)
Soil	Nr. 1	4.9 ± 0.3	5.4 ± 0.2
	Nr. 2	4.6 ± 0.3	5.1 ± 0.3
	Nr. 3	7.4 ± 0.3	8.3 ± 0.3
	Nr. 4	4.0 ± 0.3	4.3 ± 0.2
	Nr. 5	3.0 ± 0.3	3.1 ± 0.2
	Nr. 6	2.9 ± 0.3	3.1 ± 0.2
Lichen	Nr. 1	n.d.	0.5 ± 0.3
	Nr. 2	1.3 ± 0.3	1.5 ± 0.3
	Nr. 3	n.d.	2.0 ± 0.3
	Nr. 4	n.d.	0.3 ± 0.3
	Nr. 5	1.6 ± 0.3	1.8 ± 0.3
	Nr. 6	n.d.	1.3 ± 0.3

Grape sap	Nr. 1	n.d.	0.5 ± 0.3
	Nr. 2	1.4 ± 0.3	1.3 ± 0.3
	Nr. 3	n.d.	1.8 ± 0.3
	Nr. 4	1.3 ± 0.3	1.5 ± 0.3
	Nr. 5	n.d.	1.5 ± 0.3
	Nr. 6	2.4 ± 0.3	2.0 ± 0.3
Tree leaves	Nr. 1	n.d.	0.8 ± 0.3
	Nr. 2	n.d.	1.0 ± 0.3
	Nr. 3	2.8 ± 0.3	3.3 ± 0.3
	Nr. 4	n.d.	1.3 ± 0.3
	Nr. 5	n.d.	2.0 ± 0.3
	Nr. 6	2.0 ± 0.3	2.5 ± 0.3

The results of the two methods are very close, they usually agree within the errors of the determinations. In some cases it was impossible to separate unambiguously the analytical signal from the background (noted n.d.). In all these cases the quantification of the cadmium was possible only by the standard addition method.

In conclusion the methane-air flame allows the direct determination of cadmium in low concentrations without prior concentration of the analyte. The close results show the lack of interferences in the M-A flame, as observed in the acetylene flames. We consider, that for higher cadmium concentrations the standard calibration method is recommended, for concentrations close to the detection limits the standard addition method offer better results, closer to the real cadmium content of the samples. As final conclusion cadmium can be quantified precisely in soil and vegetal samples by direct aspiration using the M-A flame, without prior concentration of the analyte.

CONCLUSIONS

In the M-A flame cadmium exhibits a strong absorption of the resonance line, at the 228.8 nm. The absorption varies with the hollow-cathode lamp current, with the composition of the flame and observation height. The optimal lamp current is of 5 mA, the of observation height over

the burner head is 11 mm, in stoichiometric flame (RSU = 1.00). The absorption-concentration relationship is linear in the 0.1-10 mg.L^{-1} range, the detection limit is of 0.05 ± 0.02 mg.L^{-1} of cadmium. The cadmium content of soil, lichen, tree leave and grape sap samples can be determined accurately using the external calibration or the standard addition method. In conclusion, M-A flame is a suitable for precise atomic absorption determination of cadmium in different environmental samples.

REFERENCES

1. A. G. Gaydon, H. G. Wolfhardt, "Flames, their Structure, Radiation and Temperature", Chapman and Hill, New York, 1970
2. B. S. Ismail, K. Farihah, J. Khairiah, *B.Environ.Contam.Tox.*, **2005**,*74*, 320-327
3. C. Duran, A. Gundogdu, V. N. Bulut, M. Soylak, L. Elci, H. B. Sentürk, M. Tüfekci, *J.Hazard.Mater.*, **2007**, *146*, 347-355
4. C. Winkler, W. A. Rambeck, W. E. Kollmer, H. Zucker, Z. Tierphysiol.,Tieren Futtermk., **1984**, *51*, 250-256
5. E. Cordoş, L. N. Kékedy, R. Hui, *Patent RSR*, nr. 67867 / 1977
6. E. Fodor, A. Szabo-Nagy, *J.Plant Physiol.*, **1995**, *147*, 87-92
7. E. Meers, R. Samson, F. M. G. Tack, A. Ruttens, M. Vandegehuchte, J. Vangronsveld, M. G. Verloo, *Environ.Exp.Bot.*, **2007**, *60*, 385-396
8. G. G. Bortoleto, G.T. Macarovscha, S. Cadore, *J.Braz.Chem.Soc.*, **2004**, *15*, 313-317
9. I. Narin, M. Soylak, *Anal.Chim.Acta*, **2003**, *493*, 205-212
10. J. C. Amiard, C. Amiard-Triquet, B. Berthet, C. Metayer, *J.Exp.Mar.Biol.Ecol.*, **1987**, *106*, 73-89
11. J. L. Moya, R. Ros, I. Picazo, *Photosynth. Res.*, **1993**, *36*, 75-80
12. K. Pyrzynska, K. Kilian, *Water Res.*, **2007**, *41*, 2839-2851
13. K. Toshiaki, Y. Toshiki, S. Hiroaki, T. Hideki, S. Kazuo T., *Toxicology*, **1994**, *92*, 115-125
14. L. Ebdon, E. H. Evans, A. S. Fisher, S. J. Hill, "An Introduction to Analytical Atomic Spectrometry", John Wiley & Sons Ltd, Baffins Lane, Chichester, New York, Weinheim, Brisbane, 1998, p 43
15. M. G. Vijver, J. P. M. Vink, T. Jager, N. M.van Straalen, H.Th. Wolterbeek, C. A. M. van Gestel, *Soil.Biol.Biochem.*, **2006**, *38*, 1554-1563
16. M. H. A. Melo, S. L. C. Ferreira, R. E. Santelli , *Microchem.J.*, **2000**, *65*, 59-65
17. M. Miró, J. M. Estela, V. Cerdà, *Talanta*, **2004**, *63*, 201- 223
18. M. Shamsipur, F. Raoufi, H. Sharghi, *Talanta*, **2000**, *52*, 637-643
19. Q. H. Bin, D. Garfinkel, *Med.Hypoth.*, **1994**, *42*, 380-384
20. R. Ma, W. Van Mol, F. Adams, *Anal.Chim.Acta*, **1994**, *285*, 33-43
21. T. Crommentuijn, A. Doornekamp, C. A. M. Van Gestel, *Appl.Soil.Ecol.*, **1997**, *5*, 261-271
22. Y. S. Kim, K. Ch. Kim, Ch. W. Lee, *Bull.Korean Chem.Soc.*, **1999**, *20*, 431-435

STUDIA UNIVERSITATIS BABEŞ-BOLYAI, CHEMIA, LII, 2, 2007

DIOXYGEN ACTIVATION BY RIESKE DIOXYGENASES – COMPUTATIONAL STUDIES. 1. POSSIBLE CATALYTIC INTERMEDIATES

RADU SILAGHI-DUMITRESCU*

ABSTRACT. Density functional and semiempirical calculations were performed on the non-heme mononuclear iron active site of Rieske dioxygenases (RDO), and on complexes of this site with oxygen and activated oxygen species that have been implicated in the RDO catalytic cycle. Dioxygen binding to the high-spin ferrous center in RDOs is predicted to result in an S=2 side-on ferric-superoxo moiety, with a long O-O bond (1.36 Å). One-electron reduction of this species is predicted to result in an S=5/2 or S=3/2 side-on ferric-peroxo species. Protonation of this peroxo intermediate is predicted to result in an S=5/2 ferric-hydroperoxo species, which is predicted to readily isomerize to a perferryl-oxo-hydroxo. These results are consistent with model compound studies as well as with the recent crystal structures of dioxygen- and substrate-bound naphthalene dioxygenase.

INTRODUCTION

Rieske dioxygenases (RDO) are non-heme iron enzymes catalyzing the *cis*-1,2 di-hydroxylation of aromatic substrates by molecular oxygen and a reductant (typically one of the reduced pyridine nucleotides (NAD(P)H), inserting the equivalent of hydrogen peroxide and resulting in a non-aromatic dihydrodiol. (see Scheme 1).

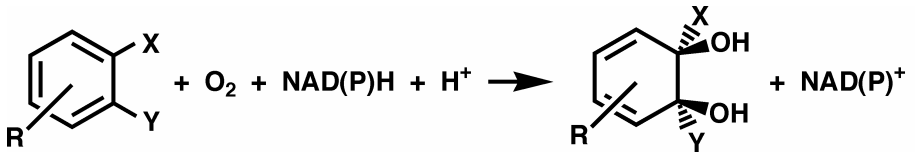

Scheme 1

* Department of Chemistry, "Babeş-Bolyai" University, Cluj-Napoca RO-400028, Romania

Mechanisms based on biochemical and model compound evidence proposed for the RDO-catalyzed reaction are shown in Figure 1.[1] In model compounds, ferric-hydroperoxo (Fe(III)-OOH) adducts are often found to undergo O-O bond cleavage forming higher-valent iron complexes (Fe(IV)=O, ferryl or Fe(V)=O, perferryl) with increased oxidative properties compared to the parent Fe(III)-OOH adducts.[1] While such chemistry is well-documented in heme enzymes, only one such high-valent intermediate has been identified in a non-heme iron oxygenase.[1] Of the ferrous-dioxygen, ferric-peroxo, ferric hydroperoxo and perferryl reaction intermediates proposed for RDOs, only the putative ferrous-dioxygen state of naphthalene dioxygenase (NDO) has been observed.[2]

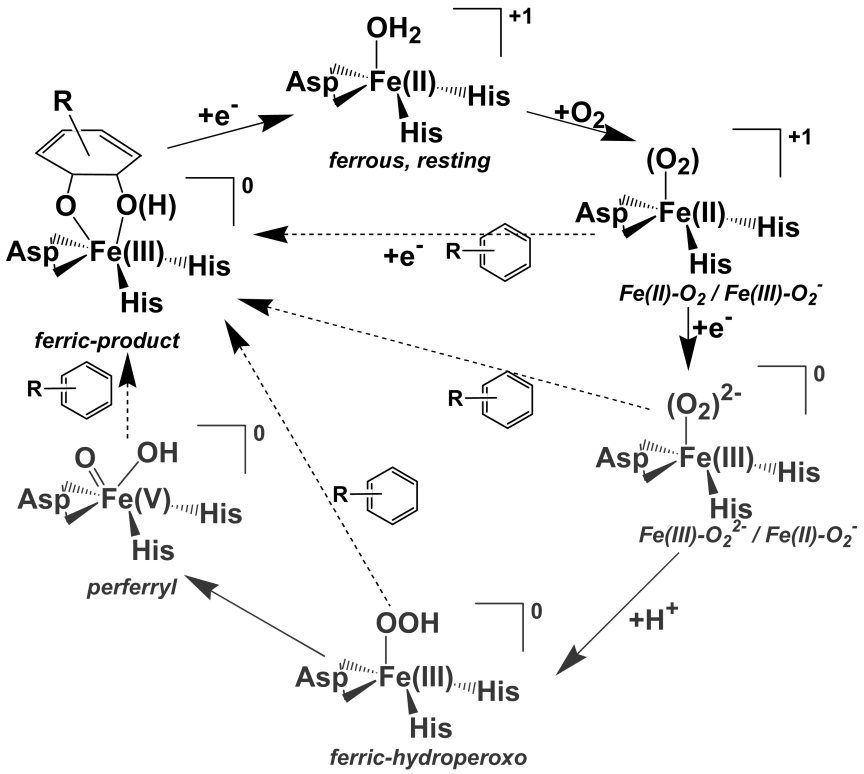

Figure 1. Proposed RDO catalytic mechanisms. Species shown in grey have never been observed in RDO. The identities of the protein-derived iron ligands are indicated. The aromatic substrate may be benzene (R = hydrogen), substituted benzenes, or other aromatics (including heterocyclic compounds).

In the present study DFT geometry optimizations were performed for models of RDO active site, as well as for various putative complexes of this active site with dioxygen and with activated dioxygen species, with the aim of predicting the most stable states – and thus the most important players in the still-elusive RDO catalytic cycle.

RESULTS AND DISCUSSION

The orientation of the protein-derived ligands changed dramatically upon unconstrained geometry optimization. These changes included reorientation of the carboxylate from semi-bidentate to clearly (symmetrically) bidentate, and rotations of the imidazole rings. Such changes are unlikely to be allowed at the active site, and attempts were made to avoid them. One option was to constrain Fe-ligand bond distances. However, this study attempts to examine and compare energies for various spin/oxidation states of putative reaction intermediates. Constraining Fe-ligand bond distances to the values seen in the crystal structure would artificially favor certain iron oxidation and/or spin states. Therefore, all protein-derived heavy atoms were kept frozen upon geometry optimization, in all models. The iron and the exogenous ligand (water, oxygen, peroxide, etc.), as well as all hydrogen atoms, were not frozen upon geometry optimization. This approach allowed the Fe-ligand distances to adjust in each model to a satisfactory degree, accommodating well any changes in spin/oxidation state (see Tables in main text). We note the non-octahedral environment around the iron (i.e., ligands are not directly *trans* to each other, so that movement of the iron away or towards any one particular ligand does not necessarily affect other Fe-ligand distances).

When discussing geometry optimization data of dioxygen / superoxo/ peroxo / hydroperoxo / oxo-hydroxo complexes, the following conventions will be used throughout. In end-on (monodentate) $O_2(H)$ ligands, the Fe-ligated oxygen atom will be labeled O1, with the other oxygen atom labeled O2. In side-on models, where the two Fe-O bond lengths are almost equal, the oxygen atom closer to the nitrogen atom labeled N1 in Figure 3 will be labeled O1, while the oxygen closer to N2 will be labeled O2. In oxo-hydroxo models, the oxo atom will be labeled O1, while the hydroxo oxygen will be labeled O2. Also, in Tables reporting partial atomic charges and excess spin densities, contributions from all of the protein-derived atoms are summed and listed under the notation "L3".

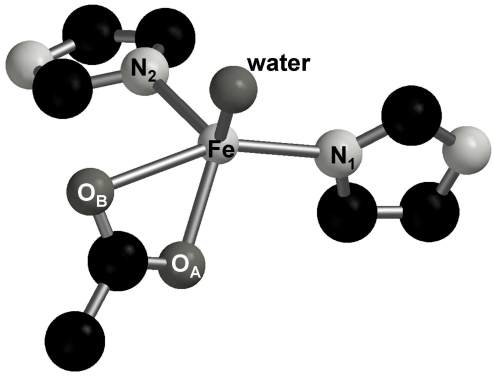

Figure 3. Geometry-optimized model **2** (S = 2, water bound), showing numbering of the protein-derived iron ligands.

Calculated energies and bond lengths for models **1** and **2** (ferrous and ferric "resting" states respectively of the NDO active site) are shown in Table 1. Table 2 lists partial atomic charges and spin densities (we note that a significant amount of spin density from the S=5/2 ferric iron appears to delocalize onto the protein derived ligands; also, the extra charge added upon reduction of **2** to **1** seems to have been delocalized to a great extent onto the protein-derived ligands). The iron site in the NDO crystal structure, 1EG9, is most likely ferrous, which is the stable oxidation state for the as-isolated enzyme in air. The crystals are also thought to have undergone reduction in the X-ray beam.[2]

Table 1.

Energies and bond distances for the ferrous and ferric "resting" states.

	Model	Energy [kcal/mol]	Fe-OH_2	O-H	Fe-N_1	Fe-N_2	Fe-O_A	Fe-O_B
1	Fe(II)-H_2O	1268564.3	2.15	0.99	2.09	2.04	1.98	2.54
2	Fe(III)-H_2O	1268327.7	2.05	0.99	2.10	2.09	2.02	2.52
1EG9	Fe-H_2O[a]	-	1.96	-	2.17	2.11	2.03	2.47

[a] Experimental geometry, from pdb entry 1EG9. The calculated Fe-O1 bond lengths suggest a ferric state in 1EG9.

Table 2.

Partial charges and spin densities (in parentheses), "resting" states.

	Model	Fe	O1	H_2O	L3[a]
1	S=2 Fe(II)-H_2O	0.76 *[3.66]*	-0.52 *[0.04]*	0.17 *[0.04]*	0.07 *[0.30]*
2	S=5/2 Fe(III)-H_2O	0.92 *[4.01]*	-0.50 *[0.08]*	0.24 *[0.09]*	0.87 *[0.90]*

[a]Sum over the protein-derived iron ligands.

"Ferrous-dioxygen" models

Calculated energies for formally ferrous-dioxygen models **3-8** are shown in Table 3. Of these models, the most stable is the side-on high-spin **8**. The recent crystal structure of dioxygen-bound naphthalene dioxygenase (with or without substrate bound)[2] suggest that the water ligand of the resting ferrous state (model **1**) is completely removed from the iron upon dioxygen binding and/or reduction to peroxide. We have nevertheless optimized geometries for models **9-17**, which are equivalents of models **3-8** but with a water ligand added. For end-on models, two coordination isomers are possible depending on whether the water ligand is placed ~trans to the N_1 nitrogen (atom numbering illustrated in Figure 3), or ~trans to N_2 (the latter models are named "exo" hereafter). Of these water models, the most stable was still the side-on high-spin (**17**). Notably, end-on models **9** and **11** converted upon geometry optimization to side-on geometries, further pointing to side-on binding of dioxygen at the NDO site as strongly favored over end-on binding. Optimized geometries for all ferrous-dioxygen models are shown in Figure S1.

A "gating" phenomenon is observed with RDOs, where dioxygen binding to the ferrous mononuclear site does not occur under physiologically-relevant conditions (but does occur under high oxygen pressure[2]) unless substrate is present *and* the nearby electron-donating Rieske site is reduced. With support from MCD and ENDOR studies, it has been argued that the gating phenomenon has a purely *structural* explanation. That is, substrate binding and reduction of the Rieske site would induce structural changes at the mononuclear site, removing one or two solvent molecules from the iron coordination sphere, thus providing open coordination positions for dioxygen. Comparison of the energies listed in Tables 1 and 2, between models **1** (ferrous-water) and **8** (ferrous-dioxygen), shows that these two states of the NDO active site have nearly equal energies (if one accounts for

the energies of free O_2 and free H_2O; zero-point vibrational energy corrections[3] and solvation would be needed for an exact comparison here). We can only hypothesize, based on these partial results, that dioxygen binding to ferrous NDO may not provide a driving force for the NDO catalytic cycle. Then, considering the high[4] $[H_2O]/[O_2]$ ratio under typical experimental and physiological conditions encountered by Rieske dioxygenases, the equilibrium between **1** and **8** would always be displaced entirely towards **1** unless external factors (such as substrate binding and reduction of the Rieske site, or increased dioxygen concentration[2]) displace it towards **8**. Then, the $[H_2O]/[O_2]$ ratio would be at least as important as previously proposed factors in "gating" O_2 access to the iron.

Table 3.

Calculated energies, "ferrous-dioxygen".

Nr.	Model	Energy [kcal/mol][a]
3	S=0 $[Fe\text{-}O_2]^{2+}$ end-on	19.8
4	S=1 $[Fe\text{-}O_2]^{2+}$ end-on	8.7
5	S=2 $[Fe\text{-}O_2]^{2+}$ end-on	9.4
6	S=0 $[Fe\text{-}O_2]^{2+}$ side-on	22.0
7	S=1 $[Fe\text{-}O_2]^{2+}$ side-on	9.9
8	S=2 $[Fe\text{-}O_2]^{2+}$ side-on	0.0
9	S=0 $[Fe\text{-}O_2]^{2+}$ end-on, + H_2O	*Side-on* (**12**)
10	S=1 $[Fe\text{-}O_2]^{2+}$ end-on, + H_2O	-47986.1
11	S=2 $[Fe\text{-}O_2]^{2+}$ end-on, + H_2O	*Side-on* (**14**)
12	S=0 $[Fe\text{-}O_2]^{2+}$ end-on, + H_2O, exo	-47980.6
13	S=1 $[Fe\text{-}O_2]^{2+}$ end-on, + H_2O, exo	-47981.3
14	S=2 $[Fe\text{-}O_2]^{2+}$ end-on, + H_2O, exo	-47981.0
15	S=0 $[Fe\text{-}O_2]^{2+}$ side-on, + H_2O	-47976.0
16	S=1 $[Fe\text{-}O_2]^{2+}$ side-on, + H_2O	-47985.6
17	S=2 $[Fe\text{-}O_2]^{2+}$ side-on, + H_2O	-47992.3

[a] Energy of model **8** (-1314962.8 kcal/mol) taken as arbitrary reference.

As shown in Table 4, in model **17**, as well as in two other less stable "extra water" models, the Fe-water distance is in fact very long, suggesting that the extra water ligand is in fact completely removed from the iron upon dioxygen binding.[3] These results not only agree with the absence of

a water ligand in the NDO "dioxygen-bound" crystal structures,[2] but also indicate these crystal structures to be placed on the most favored potential energy surface at the NDO active site (i.e., likely to be involved in the NDO catalytic cycle). Based on the above considerations, water can be excluded as a ligand to the (formally) ferrous-dioxygen form of the NDO active site.

Complexes of ferrous iron with dioxygen are often interpreted as containing a paramagnetic ferric center (S=1/2 in heme complexes) antiferromagnetically coupled to superoxide. The extremely long (1.36 Å) O-O bond of model **8** is at the upper limit of typical metal-superoxo complexes,[5] and may in fact be taken as proof of a peroxo ligand.[6] The Lowdin bond order of 1.45 is clearly indicative of a superoxo moiety, and partial atomic charges and spin densities listed in Table 5 are consistent with this interpretation. Such a long O-O bond in a ferric-superoxo system is, to our knowledge, theoretically and experimentally unprecedented. The crystal structure of ferrous NDO reacted with dioxygen[2] showed a 1.40-Å O-O bond, which, despite a relatively low resolution, the authors proposed to be indicative of a ferric-peroxo state. Our calculated 1.36-Å O-O bond now indicates the crystal structure data to also be consistent with a ferric-superoxo formulation. The Fe-O bonds of model **8** (1.83, 1.90 Å) are shorter than those observed in the substrate-free NDO-dioxygen crystal structure (2.2 and 2.3 Å), but are consistent with those observed in the crystal structure of the substrate-bound, dioxygen-bound NDO crystal structure (1.8, 2.0 Å).[2]

Table 4.

Bond distances, "ferrous-dioxygen". Lowdin bond orders are shown in parentheses, for selected models.

	Model	Fe-O1	Fe-$O2^b$	O1-O2	Fe-OH_2	Fe-N_1	Fe-N_2	Fe-O_A	Fe-O_B
3	S=0 $[Fe\text{-}O_2]^{2+}$ end-on	1.72	2.66	1.27	-	2.30	2.02	1.95	2.36
4	S=1 $[Fe\text{-}O_2]^{2+}$ end-on	1.78	2.75	1.26	-	2.14	2.09	2.00	2.48
5	S=2 $[Fe\text{-}O_2]^{2+}$ end-on	1.87	2.90	1.28	-	2.09	2.19	2.02	2.46
6	S=0 $[Fe\text{-}O_2]^{2+}$ side-on	1.76	1.96	1.33	-	2.14	2.14	2.04	2.49

Table 4. - continued

7	S=1 $[Fe\text{-}O_2]^{2+}$ side-on	1.88	1.85	1.34	-	2.19	2.12	2.00	2.44
8	S=2 $[Fe\text{-}O_2]^{2+}$ side-on[a]	1.83 (0.99)	1.90 (0.92)	1.36 (1.45)	-	2.23	2.10	2.05	2.42
9	S=0 $[Fe\text{-}O_2]^{2+}$ end-on + H_2O	-	-	-	-	-	-	-	-
10	S=1 $[Fe\text{-}O_2]^{2+}$ end-on + H_2O	1.84	2.82	1.28	2.15	2.24	2.15	2.15	2.46
11	S=2 $[Fe\text{-}O_2]^{2+}$ end-on + H_2O	-	-	-	-	-	-	-	-
12	S=0 $[Fe\text{-}O_2]^{2+}$ end-on + H_2O, exo	1.74	2.65	1.29	2.06	2.12	2.24	2.05	2.51
13	S=1 $[Fe\text{-}O_2]^{2+}$ end-on + H_2O, exo	1.87	2.85	1.25	2.58	2.12	2.14	2.06	2.52
14	S=2 $[Fe\text{-}O_2]^{2+}$ end-on + H_2O, exo	1.85	2.96	1.27	2.66	2.12	2.12	2.04	2.51
15	S=0 $[Fe\text{-}O_2]^{2+}$ end-on + H_2O	1.82	1.89	1.34	2.06	2.19	2.11	2.23	2.54
16	S=1 $[Fe\text{-}O_2]^{2+}$ side-on + H_2O	1.85	1.89	1.34	2.03	2.17	2.09	2.29	2.59
17	S=2 $[Fe\text{-}O_2]^{2+}$ end-on + H_2O	1.85	1.93	1.35	2.41	2.17	2.19	2.15	2.51

[a] Calculated Lowdin bond orders in parentheses. [b]Range of Fe-O-O angles in end-on models: 121-143.

Table 5.

"Ferrous-dioxygen": partial charges and spin densities (the latter shown in brackets).

	Model	Fe	O1	O2	OO(H)	H_2O	L3[a]
3	S=0 $[Fe\text{-}O_2]^{2+}$ end-on	0.61	-0.01	-0.12	-0.13	-	0.52
4	S=1 $[Fe\text{-}O_2]^{2+}$ end-on	0.72 *[2.67]*	-0.02 *[-0.37]*	-0.07 *[-0.61]*	-0.09 *[-0.98]*	-	0.37 *[0.35]*
5	S=2 $[Fe\text{-}O_2]^{2+}$ end-on	0.82 *[3.72]*	-0.09 *[0.03]*	-0.08 *[-0.23]*	-0.17 *[-0.20]*	-	0.23 *[0.48]*
6	S=0 $[Fe\text{-}O_2]^{2+}$ side-on	0.66	-0.06	-0.14	-0.20	-	0.54
7	S=1 $[Fe\text{-}O_2]^{2+}$ side-on	0.66 *[1.45]*	-0.10 *[0.28]*	-0.11 *[0.30]*	-0.21 *[0.58]*	-	0.55 *[-0.03]*
8	S=2 $[Fe\text{-}O_2]^{2+}$ side-on	0.78 [3.22]	-0.09 [0.24]	-0.12 [0.15]	-0.21 [0.39]	-	0.43 [0.39]
9	S=0 $[Fe\text{-}O_2]^{2+}$ end-on + H_2O	-	-	-	-	-	-
10	S=1 $[Fe\text{-}O_2]^{2+}$ end-on + H_2O	0.75 [2.88]	-0.08 [-0.42]	-0.04 [-0.71]	-0.12 [-1.13]	0.12 [0.02]	0.25 [0.25]
11	S=2 $[Fe\text{-}O_2]^{2+}$ end-on + H_2O	-	-	-	-	-	-
12	S=0 $[Fe\text{-}O_2]^{2+}$ end-on + H_2O exo	0.60	-0.02	-0.20	-0.22	0.33	0.29
13	S=1 $[Fe\text{-}O_2]^{2+}$ end-on + H_2O exo	0.74 [2.95]	-0.03 [-0.51]	-0.05 [-0.74]	-0.08 [-1.25]	0.10 [0.01]	0.24 [0.26]
14	S=2 $[Fe\text{-}O_2]^{2+}$ end-on + H_2O exo	0.79 [3.52]	-0.09 [-0.03]	-0.09 [0.11]	-0.18 [0.08]	0.09 [0.01]	0.30 [0.39]
15	S=0 $[Fe\text{-}O_2]^{2+}$ end-on + H_2O	0.59	-0.13	-0.12	-0.25	0.28	0.38
16	S=1 $[Fe\text{-}O_2]^{2+}$ side-on + H_2O	0.59 [1.34]	-0.12 [0.24]	-0.11 [0.28]	-0.23 [0.52]	0.29 [-0.01]	0.45 [0.15]
17	S=2 $[Fe\text{-}O_2]^{2+}$ end-on + H_2O	0.77 [3.23]	-0.13 [0.12]	-0.14 [0.22]	-0.27 [0.34]	0.15 [0.04]	0.35 [0.39]

[a]sum over the protein-derived iron ligands.

Finally, we note that while nitric oxide (NO) is widely used as a probe for ferrous sites of heme non-heme iron oxygen-reacting proteins (including RDOs), O_2 and NO seem to bind in completely different manners to the Rieske dioxygenase active sites: side-on vs. end-on, and with different effects on the X-O bond (X=N,O) upon binding of the diatomic XO to the iron.

"Ferric-peroxo"

Of the formally ferric-peroxo models **18-23** (Table 6), side-on S=3/2 (**22**) and S=5/2 (**23**) models are the most stable. All experimentally-characterized non-heme ferric-peroxo complexes are in fact known to be S=5/2 side-on bound (see, however[6]).

Table 6.

Calculated energies, "ferric-peroxo".

Nr.	Model	Energy [kcal/mol]
18	S=1/2 $[Fe\text{-}O_2]^+$ end-on	17.9
19	S=3/2 $[Fe\text{-}O_2]^+$ end-on	13.6
20	S=5/2 $[Fe\text{-}O_2]^+$ end-on	*side-on*[b]
21	S=1/2 $[Fe\text{-}O_2]^+$ side-on	13.6
22	S=3/2 $[Fe\text{-}O_2]^+$ side-on	0.0
23	S=5/2 $[Fe\text{-}O_2]^+$ side-on	0.6
24	S=1/2 $[Fe\text{-}O_2]^+$ side-on, + H_2O	-47970.3
25	S=3/2 $[Fe\text{-}O_2]^+$ side-on, + H_2O	-47981.5
26	S=5/2 $[Fe\text{-}O_2]^+$ side-on, + H_2O	-47990.6

[a] Energy of model **22** (-1315099.7kcal/mol) taken as arbitrary reference. [b]geometry optimization resulted in a side-on geometry.

In agreement with recent crystal structures of dioxygen-reacted ferrous NDO,[2] data in Tables 3 and 4 suggests that, upon binding to the ferrous NDO mononuclear site, dioxygen would completely displace the water ligand. Immediately after, or concerted with, its formation, the ferrous-dioxygen complex at the mononuclear site is expected to be reduced by an electron received from the nearby (~12 Å) Rieske site. Resulted from this reduction would be a formally ferric-peroxo species. To test whether this electron transfer could conceivably be coupled to re-

binding of a water ligand to iron, we have optimized geometries for models **24-26**. These models were constructed from models **21-23** by forcing a water ligand onto the peroxo-ligated iron (Fe-OH_2 starting distance as low as 1.6 Å). Of these "extra water" models, side-on S=5/2 model **26** was the most stable. However, as shown in Table 7, the Fe-water distance in **26** was very long, indicating that water is not a viable ligand to a putative ferric-peroxo complex at the NDO mononuclear site.

Energetically-favored models **23** and **26** feature O-O bond lengths and bond orders consistent with a ferric-peroxo formulation (cf. Table 7). Inclusion of an extra water molecule (models **24-26**) results in hydrogen bonding of this water molecule to the peroxo ligand, and in some degree of lengthening of the Fe-O bonds. The Fe-O and O-O bonds in model **23** are in fact a very good match for those found in the crystal structure of the dioxygen-bound, substrate-bound NDO,[2] supporting the previous assignment of this crystal structure as a ferric-peroxo species (nevertheless, as shown above, a ferric-superoxo description cannot be completely ruled out). Some predictions on the electronic absorption spectrum of a putative ferric-peroxo complex at the NDO active site are made in a separate section below.

A comparison of partial atomic charges in Tables 5 and 8 shows the added electron (upon going from formally ferric-superoxo **8** to formally ferric-peroxo **23**) to reside mainly on the dioxygen ligand and on the protein-derived ligands ("L3" in Tables).

Table 7.

Bond distances, "ferric-peroxo". Lowdin bond orders are shown in parentheses for selected models.

	Model	Fe-O1	Fe-O2	O1-O2	Fe-OH_2	O-H^a	Fe-N_1	Fe-N_2	Fe-O_A	Fe-O_B
18	S=1/2 $[Fe\text{-}O_2]^+$ end-on	1.73	2.80	1.32	-	-	2.08	2.17	2.08	2.55
19	S=3/2 $[Fe\text{-}O_2]^+$ end-on	1.79	2.77	1.34	-	-	2.08	2.15	2.08	2.55
20	S=5/2 $[Fe\text{-}O_2]^+$ end-on	-	-	-	-	-	-	-	-	-

Table 7 - continued										
21	S=1/2 $[Fe\text{-}O_2]^+$ side-on	1.81	1.91	1.39	-	-	2.10	2.22	2.10	2.54
22	S=3/2 $[Fe\text{-}O_2]^+$ side-on	1.85	1.85	1.41	-	-	2.23	2.22	2.14	2.45
23	S=5/2 $[Fe\text{-}O_2]^+$ side-on[b]	1.92 (0.77)	1.95 (0.74)	1.43 (1.28)	-	-	2.23	2.30	2.11	2.45
24	S=1/2 $[Fe\text{-}O_2]^+$ side-on, + H_2O	1.90	1.88	1.42	2.05	1.80	2.20	2.08	2.39	2.62
25	S=3/2 $[Fe\text{-}O_2]^+$ side-on, + H_2O	1.95	1.85	1.40	2.53	1.89	2.15	2.27	2.24	2.57
26	S=5/2 $[Fe\text{-}O_2]^+$ side-on, + H_2O	2.02	1.94	1.42	2.45	2.06	2.26	2.24	2.19	2.45

[a]Distance from peroxo oxygen to water proton. [b]calculated Lowdin bond orders, in parentheses.

A

Table 8.

Partial charges and spin densities, "ferric-peroxo".

	Model	Fe	O1	O2	O_2	H_2O	L3
18	S=1/2 $[Fe\text{-}O_2]^+$ end-on	0.59 [1.41]	-0.14 [-0.18]	-0.29 [-0.29]	-0.41 [-0.47]	-	-0.17 [0.06]
19	S=3/2 $[Fe\text{-}O_2]^+$ end-on	0.68 [2.78]	-0.18 [0.08]	-0.33 [-0.05]	-0.51 [0.03]	-	-0.17 [0.19]
20	S=5/2 $[Fe\text{-}O_2]^+$ end-on	-	-	-	-	-	-
21	S=1/2 $[Fe\text{-}O_2]^+$ side-on	0.62 *[0.85]*	-0.23 *[0.09]*	-0.30 *[0.06]*	-0.53 *[0.15]*	-	-0.09 *[0.00]*
22	S=3/2 $[Fe\text{-}O_2]^+$ side-on	0.73 *[2.64]*	-0.26 *[0.12]*	-0.29 *[0.13]*	-0.55 *[0.25]*	-	-0.18 *[0.11]*

Table 8. - continued							
23	S=5/2 $[Fe\text{-}O_2]^+$ side-on	0.81 *[3.80]*	-0.30 *[0.51]*	-0.34 *[0.47]*	-0.61 *[0.98]*	-	-0.20 *[0.22]*
24	S=1/2 $[Fe\text{-}O_2]^+$ sideon, + H_2O	0.56 *[0.90]*	-0.35 *[-0.01]*	-0.27 *[0.08]*	-0.62 *[0.07]*	0.18 *[-0.01]*	-0.12 *[0.02]*
25	S=3/2 $[Fe\text{-}O_2]^+$ side-on, + H_2O	0.44 *[2.65]*	-0.28 *[0.10]*	-0.10 *[0.03]*	-0.38 *[0.13]*	0.08 *[0.04]*	-0.14 *[0.18]*
26	S=5/2 $[Fe\text{-}O_2]^+$ side-on, + H_2O	0.78 [3.79]	-0.39 [0.44]	-0.30 [0.50]	-0.69 [0.94]	0.11 [0.03]	-0.38 [0.24]

Ferric-hydroperoxo

Of the ferric-hydroperoxo models **27-29** (cf. Table 9), the most stable was found to be S=5/2 end-on **29**. Attempts to geometry-optimize side-on versions of models **27-29** invariantly resulted in end-on geometries. The possibility of water re-ligation to the active site was also considered (models **30-35**). As with the ferric-superoxo models discussed above, two geometries of coordination with the extra water exist. Of these "extra water" models, the most stable was end-on S=5/2 model **35**. Almost all non-heme ferric-hydroperoxo complexes characterized to date are low-spin.[3,7,8] However, none of these low-spin hydroperoxo complexes are able to perform dioxygenations that would mimic RDO activity (i.e., incorporation of *both* atoms of the dioxygen molecule into product). Rather, these low-spin ferric-hydroperoxo complexes undergo solvent-assisted O-O bond heterolysis and only incorporate one of the dioxygen atoms into the product of the reaction (whether it be dioxygenation or monooxygenation). The idea, that a high-spin ferric-hydroperoxo complex may be an (at least indirect) signature of an iron complex that *can* perform "true" RDO-type reactions, may deserve further investigation.

Table 9.

Energies, ferric-hydroperoxo.

Nr.	Model	Energy [kcal/mol][a]
27	S=1/2 $[Fe\text{-}O_2H]^{2+}$ end-on	19.4
28	S=3/2 $[Fe\text{-}O_2H]^{2+}$ end-on	9.4
29	S=5/2 $[Fe\text{-}O_2H]^{2+}$ end-on	0.0
30	S=1/2 $[Fe\text{-}O_2H]^{2+}$ end-on, + H_2O	-47981.8
31	S=3/2 $[Fe\text{-}O_2H]^{2+}$ end-on, + H_2O	-47980.8
32	S=5/2 $[Fe\text{-}O_2H]^{2+}$ end-on, + H_2O	-47990.3
33	S=1/2 $[Fe\text{-}O_2H]^{2+}$ end-on, + H_2O, exo	-47983.1
34	S=3/2 $[Fe\text{-}O_2H]^{2+}$ end-on, + H_2O, exo	-47980.3
35	S=5/2 $[Fe\text{-}O_2H]^{2+}$ end-on, + H_2O, exo	-47991.9

[a] Energy of model **29** (-1315353.9 kcal/mol) taken as arbitrary reference.

The calculated bond lengths (cf. Table 10) in the NDO ferric-hydroperoxo models are consistent with previous experimental and theoretical data on ferric-hydroperoxo complexes. The Fe-O and O-O bonds in model **29** are clearly shorter than those previously predicted for a S=5/2 ferric-hydroperoxo complex at the active site of superoxide reductase (SOR). The short O-O bond is instead reminiscent of the S=5/2 Fe-O-OH moiety in hemerythrin.

Table 10.

Bond distances, ferric-hydroperoxo.

	Model	Fe-O1	Fe-O2	O1-O2	Fe-OH_2	Fe-N_1	Fe-N_2	Fe-O_A	Fe-O_B
27	S=1/2 [Fe-O_2H]$^{2+}$ end-on	1.70	2.88	1.50	-	2.21	2.10	2.02	2.43
28	S=3/2 [Fe-O_2H]$^{2+}$ end-on	1.76	2.79	1.47	-	2.15	2.13	2.01	2.48
29	S=5/2 [Fe-O_2H]$^{2+}$ end-on	1.88	2.82	1.43	-	2.15	2.14	2.02	2.47
30	S=1/2 [Fe-O_2H]$^{2+}$ end-on, + H_2O	1.78	2.77	1.47	2.07	2.17	2.13	2.12	2.50
31	S=3/2 [Fe-O_2H]$^{2+}$ end-on, + H_2O	1.81	2.92	1.44	2.04	2.43	2.11	2.26	2.36
32	S=5/2 [Fe-O_2H]$^{2+}$ end-on, + H_2O	1.95	2.75	1.45	2.26	2.28	2.16	2.10	2.40
33	S=1/2 [Fe-O_2H]$^{2+}$ end-on, + H_2O, exo	1.75	2.75	1.55	2.04	2.13	2.24	2.07	2.51
34	S=3/2 [Fe-O_2H]$^{2+}$ end-on, + H_2O, exo	1.78	2.80	1.45	2.41	2.19	2.16	2.14	2.49
35	S=5/2 [Fe-O_2H]$^{2+}$ end-on, + H_2O, exo	1.91	2.80	1.44	2.84	2.19	2.15	2.10	2.47

A comparison of data in Tables 2,5,8 and 11 reveals a role for "L3" (the protein-derived ligands) as a charge buffer. Namely, changes in overall oxidation states of the models are clearly reflected in changes in the partial atomic charges of L3. Thus, starting with the ferric resting state (**2**), reduction to the ferrous form (**1**) results in a significant increase of electron

density on L3. Dioxygen binding (**8**) again draws electrons out of L3, as dioxygen needs extra electron density to achieve a superoxo state (much more electron density is withdrawn from L3 than from iron). Reduction of this formally ferric-superoxo complex to the ferric-peroxo **23** leads to an increase of charge density on L3. Finally, the added proton upon formation of the ferric-hydroperoxo induces better localization of the charge density on the peroxo atoms, resulting in a decrease of charge density on L3. Such an analysis of the role of the supposedly "innocent" iron ligands in a ferric → ferrous → ferrous-dioxygen → ferric-peroxo → ferric-hydroperoxo chain of reactions is to our knowledge unprecedented for non-heme iron complexes, and it draws an unforeseen parallel to similar heme complexes, where the porphyrin is thought to hold the key to dioxygen activation, due to its ability to store oxidizing equivalents (ability thought to be unique to highly delocalized macrocycles).[9]

Table 11.

Partial charges and spin densities, ferric-hydroperoxo.

	Model	Fe	O1	O2	OOH	H_2O	L3
27	S=1/2 $[Fe\text{-}O_2H]^{2+}$ end-on	0.70 [1.04]	-0.23 [-0.02]	-0.27 [-0.05]	-0.17 [-0.07]	-	0.47 [0.03]
28	S=3/2 $[Fe\text{-}O_2H]^{2+}$ end-on	0.79 [2.62]	-0.24 [0.17]	-0.28 [0.05]	-0.18 [0.22]	-	0.39 [0.16]
29	S=5/2 $[Fe\text{-}O_2H]^{2+}$ end-on	0.90 [3.95]	-0.29 [0.44]	-0.25 [0.11]	-0.20 [0.55]	-	0.30 [0.50]
30	S=1/2 $[Fe\text{-}O_2H]^{2+}$ end-on, + H_2O	0.64 [0.72]	-0.30 [0.25]	-0.23 [0.09]	-0.20 [0.34]	0.26 [-0.01]	0.30 [-0.05]
31	S=3/2 $[Fe\text{-}O_2H]^{2+}$ end-on, + H_2O	0.78 [2.72]	-0.32 [0.09]	-0.21 [-0.02]	-0.20 [0.07]	0.26 [0.02]	0.16 [0.19]
32	S=5/2 $[Fe\text{-}O_2H]^{2+}$ end-on, + H_2O	0.88 [3.96]	-0.34 [0.40]	-0.26 [0.10]	-0.26 [0.50]	0.16 [0.05]	0.22 [0.49]
33	S=1/2 $[Fe\text{-}O_2H]^{2+}$ end-on, + H_2O, exo	0.65 [0.85]	0.23 [0.22]	0.35 [0.02]	-0.23 [0.24]	0.23 [0.00]	0.35 [-0.09]
34	S=3/2 $[Fe\text{-}O_2H]^{2+}$ end-on, + H_2O, exo	0.78 [2.65]	-0.23 [0.14]	-0.25 [0.02]	-0.11 [0.16]	0.11 [0.01]	0.22 [0.18]
35	S=5/2 $[Fe\text{-}O_2H]^{2+}$ end-on, + H_2O, exo	0.92 [3.95]	-0.35 [0.42]	-0.22 [0.12]	-0.25 [0.54]	0.09 [0.02]	0.22 [0.49]

High-valent (oxo) intermediates

End-on hydroperoxo complexes of non-heme iron model compounds have been shown to undergo O-O bond cleavage and generate catalytically competent ferryl-oxo or perferryl-oxo complexes.[10] In these model compound hydroperoxides, O-O bond cleavage is facilitated by an iron-bound (activated) water molecule, which donates a proton to the non-iron bound oxygen atom of the hydroperoxo ligand, generating water and a (per)ferryl-oxo-hydroxo compound (oxo atom derived from hydroperoxide, hydroxo atom derived from solvent), which further performs dioxygenation of various organic substrates. The dioxygenated product in these model compounds contains one peroxide-derived oxygen atom and one solvent-derived oxygen atom. We have examined the feasibility of related perferryl-oxo-hydroxo complexes at the NDO active site by optimizing the geometries of "side-on hydroperoxo" models whose starting geometries featured O-O "bond" lengths of 2.6 Å and Fe-O bond lengths of 1.80 Å. Two isomers can exist for these oxo-hydroxo complexes: one with the oxo ligand closer to the N2 iron ligand (and closer to the substrate binding site), and one with the hydroxo ligand closer to the N2 iron ligand (the latter isomer will be referred to as "exo").

Table 12.

Energies, "perferryl-oxo-hydroxo".

Nr.	Model	Energy [kcal/mol][a]
36	S=1/2 $[Fe(O)(OH)]^{2+}$	-25.2
37	S=3/2 $[Fe(O)(OH)]^{2+}$	-1.4
38	S=5/2 $[Fe(O)(OH)]^{2+}$	9.8
39	S=1/2 $[Fe(O)(OH)]^{2+}$ exo	9.9
40	S=3/2 $[Fe(O)(OH)]^{2+}$ exo	-1.2
41	S=5/2 $[Fe(O)(OH)]^{2+}$ exo	5.7

[a] Energy of *ferric-hydroperoxo* model **29** (-1315353.9 kcal/mol) taken as arbitrary reference.

Tables 12 and 13 reveal that "perferryl-oxo-hydroxo" complexes (of which low-spin model **36** is the most stable) at the NDO active site are indeed feasible. The energies of such complexes are comparable to (and, for model **36**, even lower than) those of their isomers, the ferric-hydroperoxo complexes. Calculated geometric and electronic parameters are given in Tables 13 and 14, and they are consistent with other examples of high-vaent iron complexes.[11-14]

Table 13.

Bond distances, "perferryl-oxo-hydroxo".

	Model	Fe-O1	Fe-O2	O1-O2	O-H	Fe-N_1	Fe-N_2	Fe-O_A	Fe-O_B
36	S=1/2 $[Fe(O)(OH)]^{2+}$	1.58	1.82	2.54	0.96	2.02	2.26	2.27	2.69
37	S=3/2 $[Fe(O)(OH)]^{2+}$	1.65	1.81	2.52	0.99	2.11	2.30	2.14	2.55
38	S=5/2 $[Fe(O)(OH)]^{2+}$	1.66	1.88	2.53	0.99	2.12	2.08	2.42	2.71
39	S=1/2 $[Fe(O)(OH)]^{2+}$ exo	1.58	1.81	2.71	0.99	1.96	2.13	2.45	2.84
40	S=3/2 $[Fe(O)(OH)]^{2+}$ exo	1.65	1.81	2.50	0.99	2.12	2.30	2.13	2.54
41	S=5/2 $[Fe(O)(OH)]^{2+}$ exo	1.67	1.83	2.52	0.98	2.15	2.18	2.43	2.68

Table 14.

Partial charges and spin densities, "ferryl-oxo-hydroxo".

	Model	Fe	O1	O2	OH	L3
36	S=1/2 $[Fe(O)(OH)]^{2+}$	0.71 [0.88]	-0.27 [-0.16]	-0.38 [0.28]	-0.04 [0.27]	0.60 [0.03]
37	S=3/2 $[Fe(O)(OH)]^{2+}$	0.73 [2.22]	-0.30 [0.79]	-0.37 [0.25]	-0.04 [0.25]	0.61 [-0.26]
38	S=5/2 $[Fe(O)(OH)]^{2+}$	0.78 [2.94]	-0.34 [0.76]	-0.42 [0.44]	-0.09 [0.44]	0.66 [0.86]
39	S=1/2 $[Fe(O)(OH)]^{2+}$ exo	0.70 [0.67]	-0.21 [0.24]	-0.46 [-0.04]	-0.12 [-0.04]	0.63 [0.13]
40	S=3/2 $[Fe(O)(OH)]^{2+}$ exo	0.73 [2.19]	-0.27 [0.80]	-0.39 [0.25]	-0.06 [0.25]	0.60 [-0.24]
41	S=5/2 $[Fe(O)(OH)]^{2+}$ exo	1.08 [3.12]	-0.64 [0.60]	-0.58 [0.21]	-0.26 [0.21]	0.82 [1.07]

Electronic absorption spectra of reactive intermediates

In order to provide further support for on-going efforts of experimentally characterizing the reactive intermediates that we have described at the DFT level, we have attempted to predict electronic spectra of reactive intermediates at the NDO active site, using ZINDO/S-CI on DFT-optimized geometries.[15]

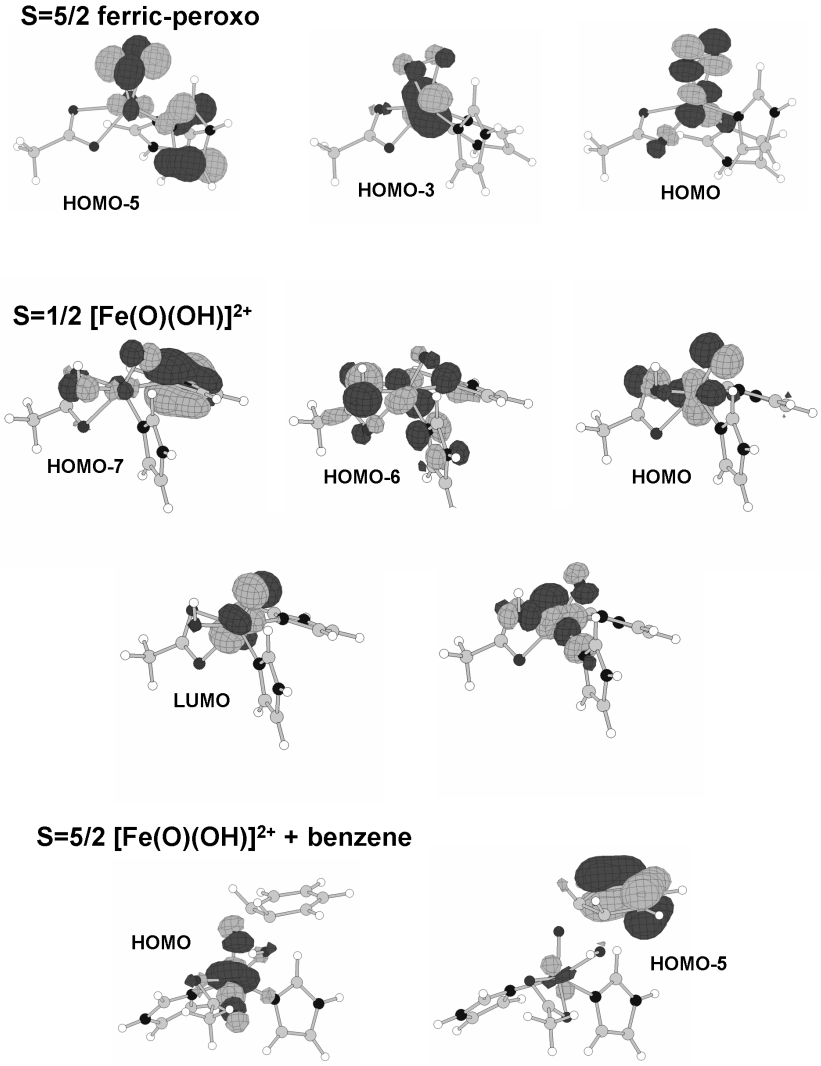

Figure 4. Main orbitals predicted to be involved in the electronic transitions in the visible region of the UV-VIS spectra for selected reactive intermediates at the NDO active site.

Ferric-peroxo complexes generally exhibit peroxo→Fe(III) charge transfer (CT) bands in the electronic absorption spectrum, at ~500-600 nm (ε~2000 $M^{-1}cm^{-1}$).[7,8] Histidine→Fe(III) CT bands are expected around 300 nm. Exceptions do exist, where relatively intense peroxo→Fe(III) CT are no longer observable at ~500-600 nm.[6] Model **23** (S=5/2 side-on ferric peroxo)

appears to be one such exception, due to the good overlap between the peroxo and histidine $\pi^{(*)}$ orbitals. As shown in Figure 4, the O-O bond in **23** is roughly perpendicular to one of the imidazole planes, and parallel to the other imidazole plane. The calculated electronic absorption spectrum featured stronger bands between 300 and 350 nm (oscillator strengths ~ 0.01 and 0.005), with histidine→Fe(III) and peroxo→Fe(III) CT character, and a weaker band at ~450 nm (oscillator strength ~0.001), with the same LMCT features (HOMO-5→HOMO-3, HOMO-5→HOMO). The main orbitals involved in these electronic transitions are shown in Figure 4. To test our hypothesis, that symmetry-based mixing or peroxo and imidazole orbitals leads to weakening of the peroxo→Fe(III) absorption in the visible region of the UV-VIS spectrum, we have also calculated the optical spectrum of a "manually" modified version of model **23**, where the peroxo moiety was reoriented to form angles of ~45° with both imidazole planes. Indeed, the oscillator strength of the band at 450 nm increased by an order of magnitude compared to the "true" (geometry optimized) model **23**.

The end-on ferric-hydroperoxo model does not show hydroperoxo→ ferric charge transfer absorption bands in the visible region. These transitions are mixed with carboxylate→ferric and imidazole→ferric absorptions at 260-300 nm. The absence of intense electronic absorptions in the visible region for ferric-hydroxperoxo complexes is not without precedent, and has been explained as due to dominance by other pi-bonding ligands.[6]

For the S=1/2 ferryl-oxo-hydroxo model **36**, a 10x5 excitation window in the configuration interaction leads to prediction of two absorption bands, one at ~390 nm (oscillator strength ~ 0.026) featuring histidine- and carboxylate-to-iron CT, and a group of bands centered between 560 and 700 nm (oscillator strengths at 0.0015-0.0053), featuring oxo-to-iron character, mixed with histidine- and carboxylate-to-iron CT (HOMO-6→LUMO, HOMO-7→LUMO, HOMO-6→HOMO, HOMO→LUMO+1). The corresponding orbitals are illustrated in Figure 4. When higher excitation windows were considered, the intensities of all the above bands decreased by at least a factor of 2.

For the S=5/2 "product-bound" model **45** (obtained from "reacting" the perferryl-oxo-hydroxo isomer with benzene) a strong band (oscillator strength ~0.463) is predicted at ~350 nm, featuring catechol-to-iron CT character, as shown in Figure 4 (HOMO-5→HOMO).

Considerations on the mechanism

Three different types of species have been proposed to be responsible for the highly selective dioxygenation accomplished at the Rieske dioxygenase active sites. A perferryl-oxo-hydroxo species has been proposed based on model compound studies. Alternatively, a side-on peroxo complex could transfer the two oxygen atoms onto an aromatic ring in a concerted fashion, as supported by recent crystal structures of the dioxygen and product-bound naphthalene dioxygenase.[2] A third mechanism, based on earlier crystal structure results and on molecular orbital symmetry considerations, involves an end-on Fe-O-O-R (R=substrate) complex, which would rearrange via a dioxetane structure, to yield the expected diol.[16]

A previous DFT study of the oxygenase reaction performed by a model compound has already shown that oxygenation of an organic substrate by a ferryl (but not perferryl) oxo-hydroxo complex (where the oxo atom originates from cleavage of a ferric-peroxo intermediate, and the hydroxo oxygen originates from solvent) has a relatively low energy barrier and is entirely feasible. Generation of the ferryl-oxo-hydroxo via protonation of the hydroperoxo by an iron-ligated water molecule was also found to have a low energy barrier. Substrate dihydroxylation by a number of model compounds has been shown to involve significant incorporation of water-derived oxygen atoms; this has been taken as proof of a ferryl-oxo-hydroxo mechanism. The same mechanism must not be valid with Rieske dioxygenases, where solvent-derived atoms are not incorporated into product to any detectable extent.

While the ferryl-oxo-hydroxo chemistry of the model compounds cannot be applied *ad literam* to Rieske dioxygenases, the possibility remains that a perferryl-oxo-hydroxo complex forms at the enzyme active site without solvent assistance.

It may be tempting to assume, based on inspection of the NDO crystal structures, that the NDO active site restricts the aromatic substrate from approaching the iron-bound activated oxygen atoms. These steric requirements would not affect in any way the peroxo-based mechanism, but would be incompatible with the ferryl-based mechanism for NDO. However, as already pointed out, spectroscopic evidence already exists for structural changes at the NDO active site upon substrate binding and upon changes in redox state at the nearby electron-transfer Rieske site. Such structural changes may conceivably involve removal of steric constraints for the perferryl-oxo mechanism.

Based on some partial electron density seen in an earlier crystal structure of indole-bound NDO, a non-concerted mechanism was proposed for indole dioxygenation, where an indole-peroxide would be formed at the NDO active site. This organic peroxide would then rearrange to an indole diol. We have attempted to model this non-concerted mechanism (using benzene as a substrate mimic, and S=5/2 peroxo as the oxygenating species), and found an activation barrier of 28 kcal/mol for formation of the "end-on" organic peroxide, and then an activation barrier of 36 kcal/mol for this peroxide isomerizing to an iron-bound benzene diol. These barriers are significantly higher than those calculated for the perferryl-oxo-hydroxo mechanism, and constitute further proof for a perferryl intermediate as *the* catalytically competent intermediate in RDOs. The lower barrier for organoperoxide formation than for subsequent diol formation suggests that, in the absence of protons, an organic peroxide may be trapped as an unproductive intermediate in the NDO active site, as seen in one of the NDO crystal structures.

Subsequent to completion of this work, Siegbahn and co-workers[17] reported a computational study on the mechanism of substrate oxidation by RDO, employing density functional theory (DFT). Dioxygen binding to the ferrous RDO site was found to yield a septet ground state. This spin multiplicity does not allow for combination of the S = 2 iron and S = 1 dioxygen frontier orbitals, consistent with an Fe-O bond longer than 2.50 Å, which is 0.8 Å longer than seen experimentally and computationally in better-characterized heme ferrous-dioxygen adducts.[18-20] This computed structure was decidedly in disagreement with the crystal structure of the NDO ferrous-dioxygen adduct, which featured a side-on dioxygen coordination geometry.[2] The lowest-energy side-on ferrous-dioxygen RDO isomers were calculated to be 5 and 10 kcal/mol higher in energy (S = 3 and S = 2, respectively). For the computed ferric-peroxo RDO models, the S = 5/2 and S = 3/2 states were close in energy, and featured side-on geometries. For the computed ferric-hydroperoxo RDO model, the S = 5/2 state was favored over S = 3/2 by 6-7 kcal/mol. DFT calculations indicated that this S = 5/2 ferric-hydroperoxo state was calculated to be capable of hydroxylating naphthalene in a multi-step mechanism where the highest activation barrier was 17-19 kcal/mol. O-O bond cleavage within S = 5/2 ferric-hydroperoxo [Fe(III)-OOH]$^{2+}$ was found to be prohibitively high, ~27 kcal/mol, suggesting that a perferryl-(oxo),hydroxo ([Fe(V)(O),OH]$^{2+}$) species would never form during the RDO catalytic cycle. O-O bond cleavage was calculated to be even more facile (activation barrier, 16

kcal/mol) in a ferrous-hydroperoxo model that would formally result upon one-electron reduction of ferric-hydroperoxo. The ferrous-hydroperoxo model was calculated to hydroxylate naphthalene in a stepwise mechanism where the highest activation barrier (involving initial attack on a carbon atom by the non-protonated oxygen atom of the Fe(III)-O-OH moiety) was 19 kcal/mol. A ferrous-hydroperoxo mechanism would be unprecedented in non-heme iron oxygenases; such chemistry is better known in heme enzymes and in non-heme model compounds.[21] Our results are mostly, but not completely consistent with those of Siegbahn and co-workers.[17].

CONCLUSIONS

Density functional calculations were reported here on the non-heme mononuclear iron active site of Rieske dioxygenases (RDO), and on complexes of this site with oxygen and activated oxygen species. Dioxygen binding to the high-spin ferrous center in RDOs is predicted to result in a S=2 side-on ferric-superoxo moiety, with a highly stranded O-O bond (1.36 Å). We propose a novel interpretation of the "gating" phenomenon in RDOs, suggesting that dioxygen binding to the ferrous site in the absence of substrate and of a reduced Rieske site may be primarily prevented by the high ($>2x10^{-6}$) $[H_2O]/[O_2]$ ratio, rather than by any specific steric/structural factors. One-electron reduction of the ferric-superoxo species is predicted to result in an S=5/2 or S=3/2 side-on ferric-peroxo species. Protonation of this peroxo is predicted to result in an S=5/2 ferric-hydroperoxo species, which is predicted to readily isomerize to a ferryl-oxo-hydroxo. These results are consistent with model compound studies, previous DFT calculations as well as with the recent crystal structures of dioxygen- and substrate-bound naphthalene dioxygenase. Electronic absorption spectra of the putative ferric-(hydro)peroxo, ferryl-oxo, and product-bound intermediates were predicted using ZINDO/S-CI calculations. Activation energies computed for substrate dihydroxylation by the species described in the present work; these results will be reported separately; they will indicate, contrary to the work from Siegbahn and co-workers, that formally Fe(V) species are the most likely active dihydroxylating agent in RDO's.

MATERIALS/METHODS

Geometries were optimized at the DFT level in the *Spartan 5.0* package at the University of Georgia Scientific Visualization and Molecular Graphics facility. The BP86 functional, which uses the gradient corrected exchange

functional proposed by Becke (1988)[22] and the correlation functional by Perdew (1986),[23] and the DN** numerical basis set (comparable in size to 6-31G**) were used as implemented in *Spartan*. For the SCF calculations, a fine grid was used and the convergence criteria were set to 10^{-6} (for the root-mean square of electron density) and 10^{-8} (energy), respectively. For geometry optimization, convergence criteria were set to 0.001 au (maximum gradient criterion) and 0.0003 (maximum displacement criterion). Charges and spin densities were derived from Mulliken population analyses after DFT geometry optimization. Lowdin bond orders were calculated at the BP/DN** geometries in the Spartan 02 for Windows package, at the BP/6-31G** level. ZINDO/S-CI calculations were performed on the DFT-optimized structures in the *Hyperchem 4.5* package.[2]

Active site models were built using heavy-atom coordinates from pdb entry 1EG9 (NDO + indole crystal structure, 1.60 Å resolution). All models were constructed within the Builder module of the *Spartan* package. All models contained Fe ligated by three protein-derived ligands: a carboxylate (modeled as CH_3COO^-) and two protonated (neutral) imidazoles (cf. Figure 3). The "fourth" (or fifth, if one counts the carboxylate as bidentate) ligand was water, peroxo, hydroperoxo, etc. (cf. Figures 2 and 3, and as listed in Tables, below). For selected models, an extra water ligand was introduced in addition to the dioxygen/superoxo/peroxo ligand.

ACKNOWLEDGEMENTS

Drs. I. Silaghi-Dumitrescu (UBB), Zanna Beharry, Eric Coulter and Donald M. Kurtz, Jr. (University of Georgia) are thanked for helpful discussions. This paper is dedicated to the memory of Dr. Eric D.Coulter.

REFERENCES

1. M. Costas, M.P. Mehn, M.P. Jensen, L.J. Que, Chem. Rev., 2004, 2, 939-86.
2. A. Karlsson, J. Parales, R. Parales, D. Gibson, H. Eklund, Science, 2003, 299, 1039-1042.
3. A. Wada, S. Ogo, S. Nagatomo, T. Kitagawa, Y. Watanabe, K. Jitsukawa, H. Masuda, Inorg. Chem., 2002, 41, 616-618.

4. A total of two water molecules are seen within ~3.5 Å from the iron in the NDO active site, in the crystal structure (1EG9); this is equivalent to an *effective concentration of water of >10 M* at the mononuclear site, even though this site is generally described as hydrophobic, .
5. D.M. Kurtz, Jr., Essays in Biochemistry, 1999, 55-80.
6. R. Silaghi-Dumitrescu, I. Silaghi-Dumitrescu, E.D. Coulter, D.M. Kurtz, Jr., Inorg. Chem., 2003, 42, 446-456.
7. J. Girerd, F. Banse, A. Simaan, Structure and Bonding, 2000, 97, 145-176.
8. E.I. Solomon, T.C. Brunold, M.I. Davis, J.N. Kemsley, S.K. Lee, N. Lehnert, N. Neese, A.J. Skulan, Y.S. Yang, Z. Zhou, Chem. Rev., 2000, 100, 235-350.
9. M. Sono, M.P. Roach, E.D. Coulter, J.H. Dawson, Chem. Rev., 1996, 96, 2841-2888.
10. A. Bassan, M. Blomberg, P. Siegbahn, L.J. Que, J. Am. Chem. Soc., 2002, 124, 11056-11063.
11. R. Silaghi-Dumitrescu, Proc. Rom. Acad. Series B, 2006, 2-3, 95-101.
12. R. Silaghi-Dumitrescu, Studia Univ. Babes-Bolyai, Chemia, 2005, 50, 17-21.
13. R. Silaghi-Dumitrescu, C.E. Cooper, Dalton Trans., 2005, 3477-3482.
14. R. Silaghi-Dumitrescu, J. Biol. Inorg. Chem., 2004, 9, 471-476.
15. HyperChem(TM) Molecular Modelling System, Release 4.5 SGI, Hypercube; Hyperchem(TM) Molecular Modelling System, Release 5.01 for Windows, Hypercube, Inc., .
16. V. Bui, M. Nguyen, J. Hansen, J. Baker, T. Hudlicky, Can. J. Chem., 2002, 80, 708-713.
17. A. Bassan, M.R. Blomberg, P.E. Siegbahn, J Biol Inorg Chem, 2004, 9, 439-52.
18. P. Rydberg, E. Sigfridsson, U. Ryde, J. Biol. Inorg. Chem., 2004, 9, 203-223.
19. R. Silaghi-Dumitrescu, I. Silaghi-Dumitrescu, Rev. Roum. Chim., 2004, 3-4, 257-268.
20. T.G. Spiro, M.K. Zgierski, P.M. Kozlowski, Coord. Chem. Rev., 2001, 219-221, 923-936.
21. R. Silaghi-Dumitrescu, Arch. Biochem. Biophys., 2004, 424, 137-140.
22. A.D. Becke, Phys. Rev., 1988, 3098-3100.
23. J.P. Perdew, Phys. Rev., 1986, B33, 8822-8824.

STUDIA UNIVERSITATIS BABEŞ-BOLYAI, CHEMIA, LII, 2, 2007

A DENSITY FUNCTIONAL STUDY OF AROMATIC RING OXYGENATION BY RIESKE DIOXYGENASE ACTIVE SITES. 2. ENERGETICS OF THE PROPOSED REACTION MECHANISMS

RADU SILAGHI-DUMITRESCU*

ABSTRACT. Density functional (DFT) calculations were performed on the non-heme mononuclear iron active site of Rieske dioxygenases (RDOs), on complexes of this site with dioxygen and activated oxygen species that have been implicated in the RDO catalytic cycle, and with the model substrate, benzene. The results were generally consistent with previous DFT studies on model compound and RDOs and recent crystal structures of dioxygen- and substrate-bound naphthalene dioxygenase., However, we identify alternative preferred pathways for substrate di-hydroxylation at the RDO active site and show, in contrast to a previous DFT study, that a formally perferryl ($[Fe(V)(O)(OH)]^{2+}$) species is a plausible intermediate in aromatic substrate di-hydroxylation. The intriguing possibility that RDOs use "controlled Fenton chemistry" to di-hydroxylate aromatic substrates is also addressed.

INTRODUCTION

Rieske dioxygenases (RDO) are non-heme iron enzymes catalyzing the *cis*-1,2 di-hydroxylation of aromatic substrates by molecular oxygen and a reductant (typically one of the reduced pyridine nucleotides (NAD(P)H), inserting the equivalent of hydrogen peroxide and resulting in a non-aromatic dihydrodiol. (see Scheme 1).

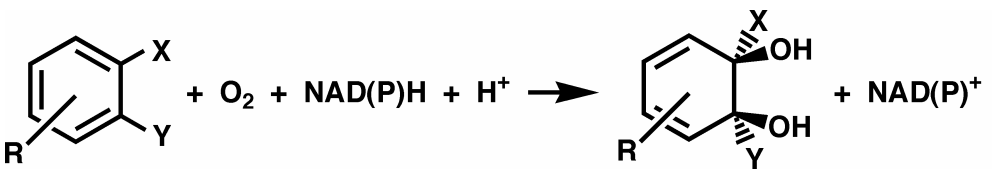

Scheme 1

* Department of Chemistry, "Babeş-Bolyai" University, Cluj-Napoca RO-400028, Romania

Mechanisms based on biochemical and model compound evidence proposed for the RDO-catalyzed reaction are shown in Figure 1.[1] In model compounds, ferric-hydroperoxo (Fe(III)-OOH) adducts are often found to undergo O-O bond cleavage forming higher-valent iron complexes (Fe(IV)=O, ferryl or Fe(V)=O, perferryl) with increased oxidative properties compared to the parent Fe(III)-OOH adducts.[1] While such chemistry is well-documented in heme enzymes, only one such high-valent intermediate has been identified in a non-heme iron oxygenase.[1] Of the ferrous-dioxygen, ferric-peroxo, ferric hydroperoxo and perferryl reaction intermediates proposed for RDOs, only the putative ferrous-dioxygen state of naphthalene dioxygenase (NDO) has been observed.[2]

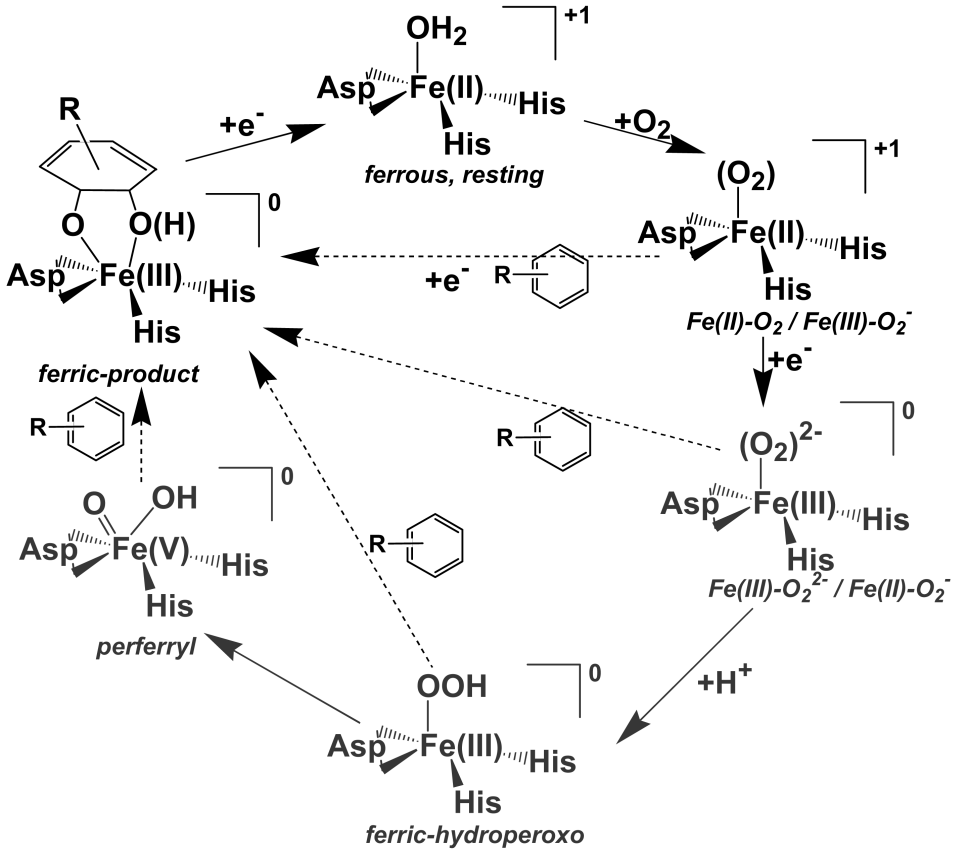

Figure 1. Proposed RDO catalytic mechanisms. Species shown in grey have never been observed in RDO. The identities of the protein-derived iron ligands are indicated. The aromatic substrate may be benzene (R = hydrogen), substituted benzenes, or other aromatics (including heterocyclic compounds).

Siegbahn and co-workers[3] recently reported a computational study on the mechanism of substrate oxidation by RDO, employing density functional theory (DFT). Their results indicated that this $S = 5/2$ ferric-hydroperoxo state would be capable of hydroxylating naphthalene in a multi-step mechanism where the highest activation barrier was 17-19 kcal/mol. O-O bond cleavage within $S = 5/2$ ferric-hydroperoxo $[Fe(III)\text{-}OOH]^{2+}$ was found to be prohibitively high, ~27 kcal/mol, suggesting that a perferryl-(oxo),hydroxo ($[Fe(V)(O),OH]^{2+}$) species would never form during the RDO catalytic cycle. O-O bond cleavage was calculated to be even more facile (activation barrier, 16 kcal/mol) in a ferrous-hydroperoxo model that would formally result upon one-electron reduction of ferric-hydroperoxo. The ferrous-hydroperoxo model was calculated to hydroxylate naphthalene in a stepwise mechanism where the highest activation barrier (involving initial attack on a carbon atom by the non-protonated oxygen atom of the Fe(III)-O-OH moiety) was 19 kcal/mol. A ferrous-hydroperoxo mechanism would be unprecedented in non-heme iron oxygenases; such chemistry is better known in heme enzymes and in non-heme model compounds.[4]

Prior to publication of Siegbahn and co-worker's DFT study,[3] we obtained an extensive set of data on the RDO catalytic cycle employing a slightly different computational strategy (BP86 functional vs. B3LYP, and a different choice of geometrical constraints on the protein-derived ligands). Our results are mostly, but not completely consistent with those of Siegbahn and co-workers.[3]. We report here the portion of our results that distinctly impacts our understanding of the RDO catalytic cycle. In particular, a substrate dihydroxylation pathway involving a perferryl-(oxo),hydroxo intermediate is shown to be feasible for RDO. A feasible mechanism for substrate hydroxylation by a Fe(II)-OOH intermediate is also identified, involving initial attack by the terminal -OH, which is distinct from that previously characterized by Siegbahn and co-workers. ZINDO/S-CI computed electronic absorption spectra are reported for proposed reaction intermediates, in an attempt to facilitate structure assignment upon UV-vis absorption spectra if/when such intermediates are characterized experimentally.

RESULTS AND DISCUSSION

Putative catalytic intermediates. The electronic structures of the putative intermediates illustrated in Figure 1, i.e. ferrous-dioxygen, ferric-peroxo, ferric-hydroperoxo and perferryl were previously described (accompanying article in this issue, and Ref[3]) and are not discussed here in detail,. We note that for

"ferrous-dioxygen" models our approach favours side-on vs. end-on geometries and $S = 5/2$ vs. $S = 3/2$, which is consistent with the experimentally-observed side-on dioxygen coordination in the NDO crystal structure.[2] The particularly long O-O bond observed experimentally (1.4 Å) is well reproduced.[2] For the perferryl intermediate, $S = 1/2$ is calculated to be the ground state, with an Fe(V)-type electronic structure consistent with previous descriptions. It is shown elsewhere that molecular orbitals and spin densities derived from DFT may be misleading in describing "high-valent" iron in biological coordination environments, and that more mundane Fe(III) or Fe(II) descriptions (with extra oxidizing equivalents localized on the ligands) are obtained with post-HF methods.[5,6]

In addition to the models already reported upon by Siegbahn and co-workers,[3] we also examined the effect of adding a water molecule to the coordination environments of ferrous-dioxygen, ferric-peroxo and ferric-hydroperoxo. Spectroscopic evidence for two water molecules in the iron coordination sphere exists in contrast to crystal structures showing only one water molecule.[2,7,8] The added water molecule did not alter the electronic structures and in particular the general preference for high-spin states and side-on coordination of O_2 and O_2^{2-}; This lack of effect together with the long iron-water bond seen in the most stable isomers, argue against a key role of a water ligand in controlling electronic structure.

O-O bond cleavage. Siegbahn and co-workers previously calculated a 26 kcal/mole activation barrier for O-O bond cleavage in an $S = 5/2$ ferric-hydroperoxo RDO model which was deemed to be prohibitively high.[3] Figure 2 shows the calculated energy profile for O-O bond elongation and cleavage in our $S = 5/2$ Fe(III)-OOH model. Consistent with previous results, the process is endothermic. In contrast to the previous results, however, the significantly lower estimated activation barrier of 15.9 kcal/molimplies that at O-O bond cleavage from this species is feasible. The product's $S = 3/2$ and $S = 1/2$ states are 7-30 kcal/mol (depending on conformer and spin state) more stable than $S = 5/2$, implying that O-O bond cleavage would be feasible both kinetically and thermodynamically. In fact, a lowering of the right-hand side of the diagram in Figure 2 by 30 kcal/mol implies that the activation barrier may well be lower than 15 kcal/mol – and thus even more feasible.

The reaction coordinate driving process illustrated in Figure 2 is expected to be sensitive to minor changes in starting geometry, the geometrical coordinate chosen, and the method used in following that

geometry. For the results in Figure 2, the O-O bond was elongated stepwise from the equilibrium distance of 1.46 Å in *S* = 5/2 ferric-hydroperoxo, $[Fe(III)\text{-}OOH]^{2+}$, to 2.36 Å in *S* = 5/2 perferryl-(oxo)hydroxo, $[Fe(V)(O)(OH)]^{2+}$; the geometry optimized at an O-O distance of {1.46 + n} Å (n ≥ 0.10) is used as starting point for geometry optimization at {1.46 + n + 0.10} Å (with smaller steps at higher energies). An alternative to this process would be to vary the Fe---OH distance, as it changes from 2.36 Å in *S* = 5/2 $[Fe(III)\text{-}O\text{-}OH]^{2+}$ to 1.82 Å in *S* = 5/2 $[Fe(V)(O)(OH)]^{2+}$. However, this latter approach failed to identify a plausible O-O cleavage mechanism: stepwise shortening of the Fe-OH distance down to 1.82 Å was found not to bring about *any* elongation in O-O bond length, and removal of the Fe-OH constraint invariably resulted in the structure converging back to the Fe(III)-OOH starting geometry. This difference between two approaches for monitoring the same reaction caution us for further studies and is also likely to at least partially explain the difference between our results and those of Siegbahn and co-workers.[3] Further differences are expected to arise from the different treatment of the model; to mimic steric constraints imposed by the protein, Siegbahn and co-workers included in their models the □-carbon atoms of the histidine ligands and then froze the positions of these two carbon atoms as well as the position of the acetate methyl carbon.[3] However, having noted that free movement of the carboxylate in our models invariably results in a quasi-symmetrical bidentate coordination of the acetate to the iron (unlike in *any* of the RDO crystal structures), and having noted that significant rotation and reorientation of the imidazole rings occur upon unconstrained geometry optimization, we chose to freeze the positions of *all* protein-derived heavy atoms, allowing free movement of the iron, protons, and exogenous ligands.

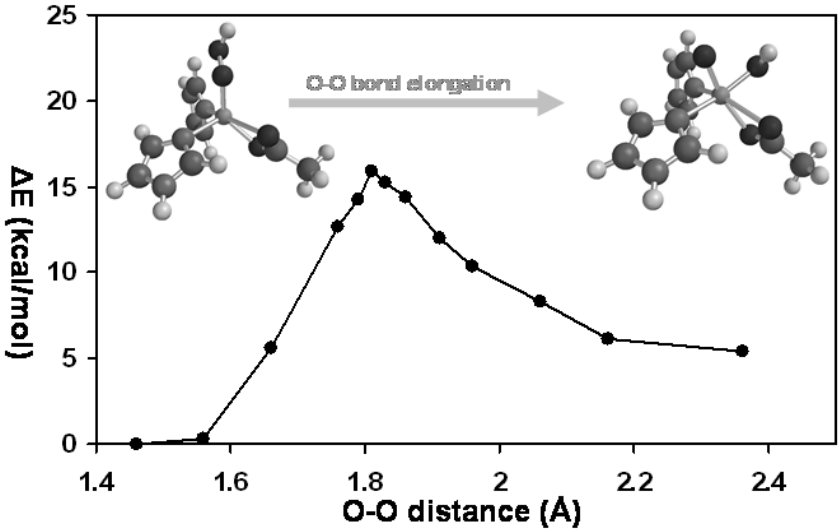

Figure 2. Variation of the potential energy as a function of the O---O distance during O-O bond cleavage within a *S* = 5/2 $[Fe(III)\text{-}OOH]^{2+}$ model (structure shown on the left), to yield *S* = 5/2 $[Fe(V)(O)(OH)]^{2+}$ (structure shown on the right).

Substrate di-hydroxylation. Figures 3 and 4 illustrate possible processes leading from an RDO reaction intermediate to di-hydroxylated product. The ferric-hydroperoxo (B) and perferryl-(oxo)hydroxo species (D and E) were the most likely candidates based on model compound studies.[3] The ferric-peroxo state (F) was also previously proposed.[2] Concerted as well as stepwise mechanisms are considered. Benzene, the simplest aromatic RDO substrate, is used in these calculations. Previous calculations by Siegbahn and co-workers employed a larger substrate, naphthalene, which is intrinsically expected to show slightly lower activation barriers than benzene.[9]

We identified one pathway (E) for benzene di-hydroxylation with a low activation barrier (11 kcal/mol) involving a perferryl, $[Fe(V)(O)OH]^{2+}$, as the di-hydroxylating agent. Although previous computational studies of synthetic complexes had suggested the feasibility of perferryl formation form ferric-hydroxperoxo,[10,11] Siegbahn and co-workers reported that di-hydroxylation of naphthalene was more likely to occur directly from a ferric-hydroperoxo with a lowest activation barrier of 17.5 kcal/mol.[3] Our results, on the other hand, indicate that the barrier for di-hydroxylation by $[Fe(III)\text{-}OOH]^{2+}$ (22 kcal/mol) is higher than the barrier for O-O bond cleavage in $[Fe(III)\text{-}OOH]^{2+}$ (16 kcal/mol).

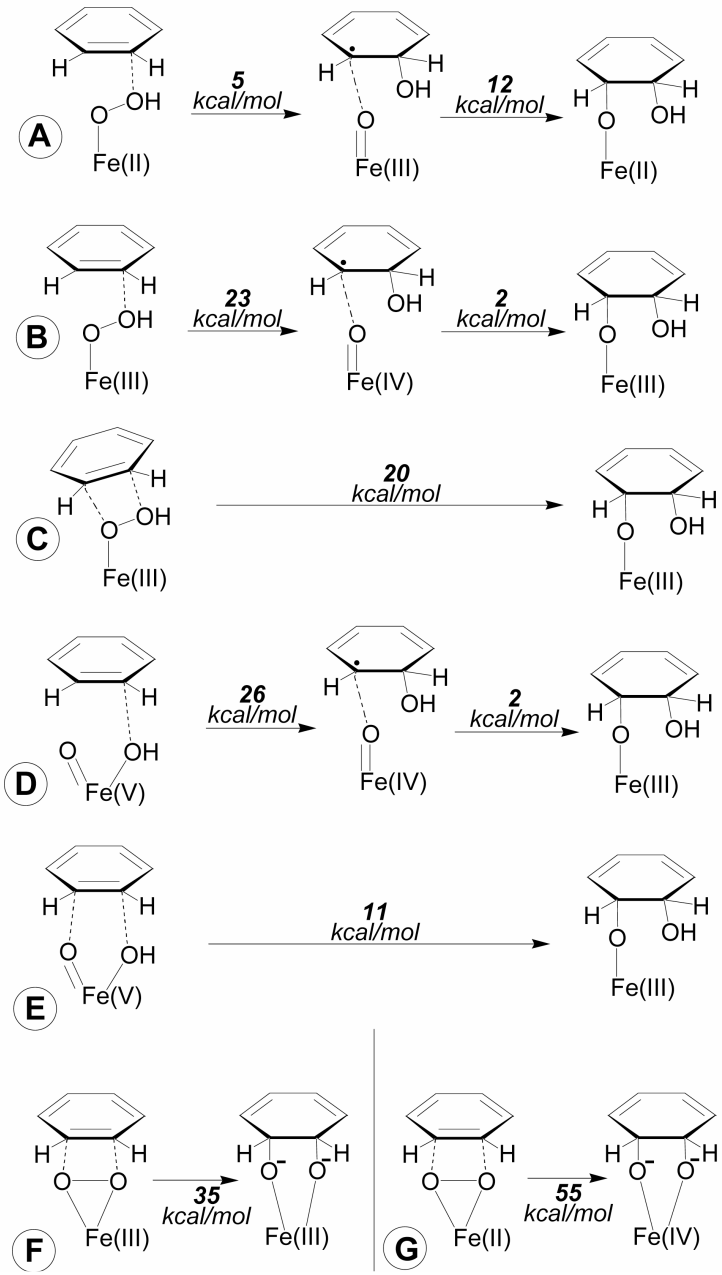

Figure 3. Possible mechanisms for substrate di-hydroxylation by RDO. Numbers indicate estimates of activation barriers based on data shown in Figure 4.

As did Siegbahn and co-workers,[3] we found a ferrous-hydroperoxo, $[Fe(II)\text{-}OOH]^+$, model to be an even lower-activation-barrier di-hydroxylating agent. We, thus, find that the pathway involving facile transfer of an OH radical-like moiety from Fe(II)-O-OH to substrate has a lower activation barrier than the pathway reported by Siegbahn and co-workers, which involved initial O-O bond cleavage of ferrous-hydroperoxo, $[Fe(II)\text{-}O\text{-}OH]^+$, to formally ferryl, $[Fe(IV)(O)(OH)]^+$, followed by substrate di-hydroxylation, with both steps relatively feasible energetically. Our lower estimated activation barrier, 12 kcal/mol, may relate to the fact that our calculated equilibrium O-O distance in $[Fe(II)\text{-}OOH]^+$ is extremely long (1.9 Å) even in the absence of the substrate, implying that substrate hydroxylation by this ferrous-hydroperoxo does not incur an additional energy penalty for breaking an O-O or Fe-O bond. Based on the computed activation barriers, Fe(III)-peroxo (reactions B and C in Figure 3) and Fe(II)-dioxygen (reaction G in Figure 3) are found significantly less likely to be involved in substrate hydroxylation.

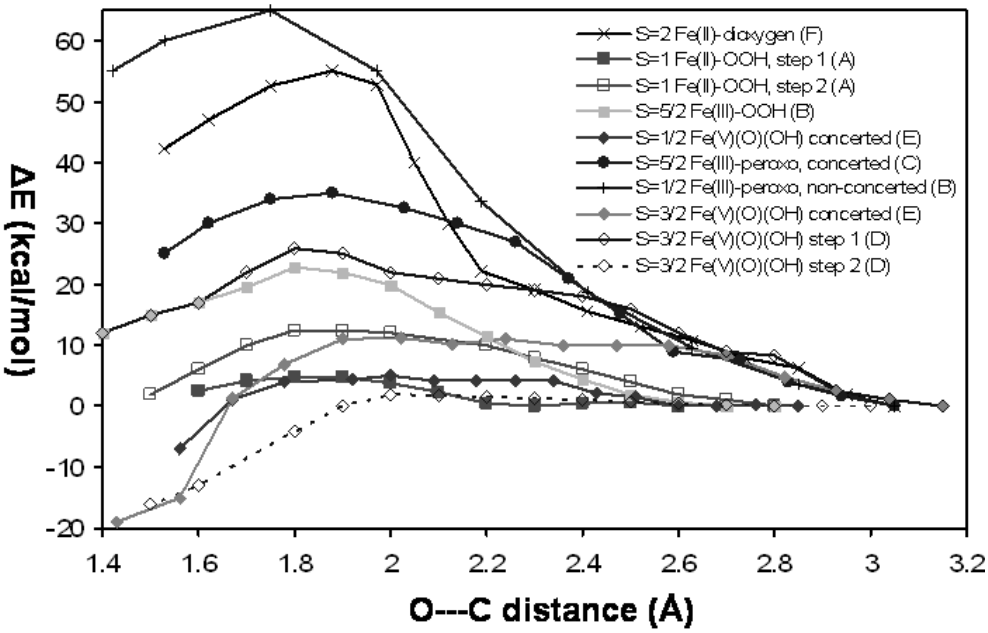

Figure 4. Variation of the potential energy as a function of the O---C distance(s) during substrate hydroxylation for the structures shown in Figure 3.

Figure 5 illustrates the overall calculated thermodynamics of dioxygen activation by the RDO model employed in the present study. The first step, reduction of the resting Fe(III) state, is extremely favorable thermodynamically. The high electron affinity calculated for the "resting" Fe(III) RDO is consistent with the fact that this state has never been observed experimentally; RDOs are typically isolated in the ferrous state even under aerobic conditions.[12,13] Similarly, the high electron affinity of the ferrous-dioxygen state (136 kcal/mol,) is suggestive of a very short lifetime. The extremely elongated O-O bond (1.36 Å) in the formally $[Fe(II)\text{-}O_2]^{2+}$ RDO, suggestive of a partial Fe(IV)-peroxo character, may contribute to the high electron affinity; the increased reactivity suggested by the strained O-O ligand in the ferrous-dioxygen adduct is however not enough by itself to support substrate hydroxylation (cf. Figures 3 and 4, the barrier would be 55 kcal/mol). The putative ferrous-dioxygen state has been observed experimentally only in a NDO crystal structure, where the exact oxidation state of the mononuclear site could not be probed; one-electron reduction to $Fe(III)\text{-}O_2^{2-}$ cannot be excluded;[2] according to our DFT results, the ferrous-dioxygen and ferric-peroxo states would be geometrically indistinguishable by protein X-ray crystallography at typical resolutions of 1.7-2.5 Å. The proton affinity of the ferric-peroxo state, ~250 kcal/mol, is somewhat lower but still in the same range as the proton 330-430 kcal/mol proton affinities of ferric-peroxo adducts of hemoproteins calculated at the same level of theory;[14] the hemoprotein ferric-peroxo adducts become protonated even at temperatures significantly below 0^{o} C, again suggesting a short lifetime for ferric-peroxo RDO. From the ferric-hydroperoxo stage, product can be formed either directly as proposed by Siegbahn and co-workers,[3] or via a perferryl intermediate; the activation barriers for these processes are in the range 11-17 kcal/mol, which is the same range seen for substrate hydroxylation by cytochrome P450 Compound I at the same level of theory.[15-18] With P450 Compound I eluding observation in the presence of substrate even at cryogenic temperatures,[19] isolation/detection of an RDO hydroxylating intermediate is expected to be similarly challenging experimentally.

The emerging picture from the present results and those of Siegbahn and co-workers[3] is that aromatic substrate di-hydroxylation at the RDO active site is feasible with ferric-hydroperoxo as well as perferryl intermediates, with our results suggesting that the latter is slightly preferred, and that a ferrous-hydroperoxo, $[Fe(II)\text{-}OOH]^{+}$, species – if ever formed - would be the lowest-activation-barrier hydroxylating agent of all

those considered here. This very reactive $[Fe(II)OOH]^+$ species with a long O-OH bond is reminiscent of the "bound hydroxyl radical" characterization of the Fenton reagent.D. T. Sawyer, A. Sobkowiak, T. Matsushita, *Acc. Chem. Res.*, 1996**, 29**, 409. While the possibility that RDOs use "controlled Fenton chemistry" to di-hydroxylate aromatic substrates is intriguing, there is currently no evidence for formation of ferrous-(hydro)peroxo species in Rieske dioxygenases. RDO active sites may actually be designed to *avoid* formation of a ferrous-hydroperoxo, since its high reactivity would make it less selective in its targets. More reliable computational results would likely emerge from QM/MM calculations directly accounting for the protein environment. However, the issue of locating a suitable pathway for the various reactions (as exemplified by the differences between our results and those of Siegbahn and co-workers) would not necessarily be alleviated by use of a larger model. These theoretical approaches can, nevertheless, complement and guide ongoing attempts to trap the actual intermediates in the RDO catalytic cycle.

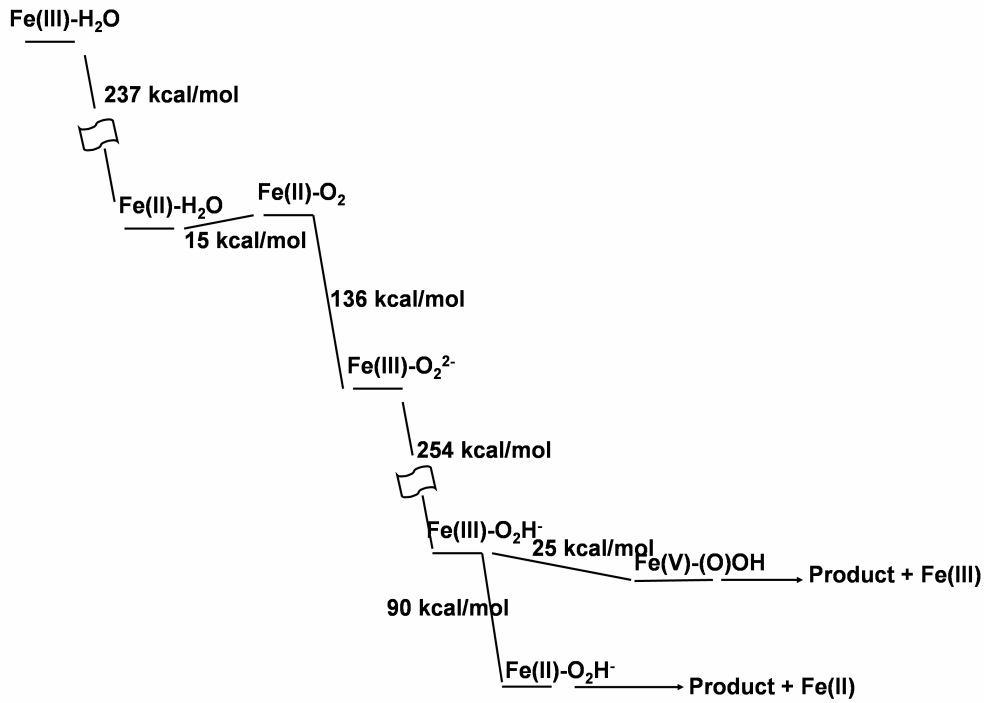

Figure 5. DFT-derived thermodynamics of dioxygen activation by RDO.

METHODS

The BP86 functional, which uses the gradient corrected exchange functional proposed by Becke (1988)[20] and the correlation functional by Perdew (1986),[21] and the DN** numerical basis set (comparable in size to 6-31G**) were used as implemented in *Spartan*.[22] For the SCF calculations, a fine grid was used and the convergence criteria were set to 10^{-6} (for the root-mean square of electron density) and 10^{-8} (energy), respectively. For geometry optimization, convergence criteria were set to 0.001 au (maximum gradient criterion) and 0.0003 (maximum displacement criterion). Charges and spin densities were derived from Mulliken population analyses after DFT geometry optimization.

Active site models were built using heavy-atom coordinates from Protein Data Bank entry 1EG9 (NDO with indole bound at the active site, 1.60 Å resolution). All models were constructed within the Builder module of the *Spartan* package. All models contained iron ligated by three protein-derived ligands: a carboxylate (modelled as CH_3COO^-) and two protonated (neutral) imidazoles (cf. Figure 2). The "fourth" (or fifth, if one counts the carboxylate as bidentate) ligand was water, peroxo, hydroperoxo, etc. For selected models, an extra water ligand was introduced in addition to the dioxygen/superoxo/peroxo ligand.

Reaction path calculations were set up starting from the separately calculated structures of ferrous-dioxygen, ferric-peroxo, ferric-hydroperoxo, ferrous-hydroperoxo and perferryl intermediates, to which a benzene moiety was added in such a way that each of the two iron-bound oxygen atoms was within 2.85 Å of a benzene carbon atom. The benzene moiety was placed above the His208 imidazole (using the residue numbering of the NDO crystal structure (the N1 imidazole in Figure S1, cf. Supporting Information), and roughly perpendicular to the Fe-O-O plane, so as to avoid placing the benzene hydrogens directly in between the oxygen and carbon atoms. To model a concerted mechanism, the two oxygen-to-carbon distances were constrained to be equal to each other and with values varying monotonically in-between 2.85 and 1.3 Å. Alternatively, to model non-concerted mechanisms, only one oxygen-carbon distance was varied at a time. For monitoring cleavage of the O-OH bond in ferric-hydroperoxo models in the absence of benzene, the O-O distance was constrained, successively, to values ranging from the equilibrium distance in Fe-O-OH to the equilibrium distance in the perferryl-oxo-hydroxo isomer.

The orientation of the protein-derived ligands changed dramatically upon unconstrained geometry optimization. These changes included reorientation of the carboxylate from semi-bidentate to clearly (symmetrically) bidentate, and rotations of the imidazole rings. Due to constraints imposed by the protein, such changes are unlikely to be allowed at the RDO active site (nor is there any experimental evidence for them), and attempts were made to avoid them. One option was to constrain iron-ligand bond distances. However, this study attempts to examine and compare energies for various spin/oxidation states of putative reaction intermediates. Constraining iron-ligand bond distances to the values seen in the crystal structure might artificially favor certain iron oxidation and/or spin states. Therefore, all protein-derived heavy atoms were kept frozen upon geometry optimization, in all models, whereas, the iron and the exogenous ligands (water, oxygen, peroxide, etc.), as well as all hydrogen atoms, were not frozen upon geometry optimization. This approach allowed the iron-ligand distances to adjust in each model to a satisfactory degree, accommodating well any changes in spin/oxidation state. We note the non-octahedral environment around the iron, i.e., the ligands are not directly *trans* to each other, so that movement of the iron away or towards any one particular ligand does not necessarily affect other iron-ligand distances.

ACKNOWLEDGEMENTS

Dr. I. Silaghi-Dumitrescu (UBB) is thanked for helpful discussions.

REFERENCES

1. M. Costas, M. P. Mehn, M. P. Jensen, L. J. Que, Chem. Rev., 2004, **2**, 939.
2. A. Karlsson, J. Parales, R. Parales, D. Gibson, H. Eklund, Science, 2003, **299**, 1039.
3. A. Bassan, M. R. Blomberg, P. E. Siegbahn, J Biol Inorg Chem, 2004, **9**, 439.
4. R. Silaghi-Dumitrescu, Arch. Biochem. Biophys., 2004, **424**, 137.
5. R. Silaghi-Dumitrescu, Studia Univ. Babes-Bolyai, Chemia, 2005, **50**, 17.
6. V. Balland, M. F. Charlot, F. Banse, J. Girerd, T. A. Mattioli, E. Bill, J. F. Bartoli, P. Battioni, D. Mansuy, Eur. J. Inorg. Chem., 2004, 301.

7. T.-C. Yang, M. Wolfe, M. B. Neibergall, Y. Mekmouche, J. D. Lipscomb, B. M. Hoffman, J. Am. Chem. Soc., 2003, **125**, 2034.

8. T. C. Yang, M. D. Wolfe, M. B. Neibergall, Y. Mekmouche, J. D. Lipscomb, B. M. Hoffman, J Am Chem Soc, 2003, **125**, 7056.

9. A. Bassan, M. Blomberg, P. Siegbahn, L. J. Que, J. Am. Chem. Soc., 2002, **124**, 11056.

10. A. Bassan, M. R. Blomberg, P. E. Siegbahn, L. Que, Jr., J Am Chem Soc, 2002, **124**, 11056.

11. A. Bassan, M. R. Blomberg, P. E. Siegbahn, L. Que, Jr., Angew Chem Int Ed Engl, 2005, **44**, 2939.

12. D. M. Eby, Z. M. Beharry, E. D. Coulter, D. M. Kurtz, Jr., E. L. Neidle, J. Bacteriol., 2001, **183**, 109.

13. Z. M. Beharry, D. M. Eby, E. D. Coulter, R. Viswanathan, E. L. Neidle, R. S. Phillips, D. M. Kurtz, Jr., Biochemistry, 2003, **42**, 13625.

14. R. Silaghi-Dumitrescu, I. Silaghi-Dumitrescu, Rev. Roum. Chim., 2004, **3-4**, 257.

15. R. Silaghi-Dumitrescu, C. E. Cooper, Dalton Trans., 2005, 3477.

16. V. Guallar, M. H. Baik, S. J. Lippard, R. A. Friesner, Proc. Natl. Acad. Sci. USA, 2003, **100**, 6998.

17. V. Guallar, R. A. Friesner, J. Am. Chem. Soc., 2004, **126**, 8501.

18. B. Meunier, S. P. de Visser, S. Shaik, Chem Rev, 2004, **104**, 3947.

19. B. M. Hoffman, Acc. Chem. Res., 2003, **36**, 522.

20. A. D. Becke, Phys. Rev., 1988, 3098.

21. J. P. Perdew, Phys. Rev., 1986, **B33**, 8822.

22. Spartan 5.0, Wavefunction, Inc., 18401 Von Karman Avenue Suite 370, Irvine, CA 92612 U.S.A.